Journal of the European Ceramic Society
Available online 3 July 2022, Version of Record 13 August 2022; DOI: 10.1016/j.jeurceramsoc.2022.06.080

TRIBOLOGICAL BEHAVIOUR OF TRANSPARENT CERAMICS: A REVIEW

Divyansh Mittal[a], Jan Hostaša[b], Laura Silvestroni[b], Laura Esposito[b], Anita Mohan[c], Rajiv Kumar[a], Sandan Kumar Sharma[a1]

[a]Department of Metallurgical and Materials Engineering, Punjab Engineering College (Deemed to be University), Chandigarh, India

[b]Institute of Science and Technology for Ceramics, National Research Council (CNR ISTEC), Via Granarolo 64, Faenza, Italy

[c]Department of Physics, Indian Institute of Technology (BHU), Varanasi, India

Abstract

Owing to superior properties, i.e. high hardness, high wear resistance, and weight reduction of transparent ceramics (TCs) over glasses, TCs have shown promising tribological potential for applications such as face shields, explosive ordnance visors, windows for aircraft, spacecraft and, re-entry vehicles, electromagnetic windows, laser igniter windows, screens for smartphones and more. Researchers globally have been attracted to explore more about TCs, considering the tremendously increasing demand over different other transparent materials. The optical quality of TCs is mostly characterized by the in-line transmittance, and the effect of various processing parameters on transmittance has already been studied by various researchers. In this review, the current research progress regarding tribological performance of TCs is compiled. TCs with potential in tribological applications include $MgAl_2O_4$, Al_2O_3, AlON, Lu_2O_3, c-BN, Y_2O_3, Si_3N_4, and SiAlON. The relevant strategies to improve the tribological properties, including microstructures and mechanical properties are comprehensively discussed. In addition, the mechanisms of material removal of different transparent ceramics are also presented. It is well observed that surface fracture comprising three stages is found as one of the dominant wear mechanisms during wear. This review aims to provide some meaningful guidelines for development of transparent ceramics with enhanced wear resistance, while identifying the wear mechanisms in particular wear conditions.

Keywords: transparent; ceramics; tribology; wear mechanism; microstructure

---

[1]Corresponding author, Tel: +91-9027186120; E-mail: sandansharma07@gmail.com

1. Introduction

Transparent ceramics (TCs) have been widely used materials in various applications during the last few decades. The first step toward the development of transparent ceramic dates back to Coble's invention of translucent alumina in 1959 [1] for the production of ceramic discharge tubes. It eventually resulted in the widespread use of high-pressure sodium vapour lamps for street lighting and a variety of other applications. Consequently, translucent and transparent ceramics became a key study area for different potential applications. In the 1970s, a viability study for transparent $MgAl_2O_4$ manufacturing was commenced [2], and in 1978 it was used for transparent armor [3]. In 1995, Ikesue et al. [4] demonstrated the first effective laser oscillation using a ceramic material (Nd: YAG), indicating that ceramics is utilized for laser applications [5] with an efficiency equivalent to single crystal lasers [6]. Between the 2000s and 2010s, interest in transparent ceramics increased steadily. As a result, transparent ceramics research is well established in fields such as armor, impact-resistant windows, and missile domes [7–14], scintillators [15], phosphors [16,17], optical lenses [9], 3D displays [18], laser gain media [19,20], and other optical applications [7–14].

To explore the universe, studying the light or electromagnetic radiations of all the wavelengths emitted by different objects in space is necessary [21]. Various observatories and re-entry vehicles are sent to the atmosphere to get valuable information about the space. These observatories use many transparent materials for different purposes. Window materials for such spacecraft must satisfy a set of strict requirements to bear the thermal shock, uphold cabin pressure, resist aerodynamic heating, and tolerate high-velocity impact by foreign particles. TCs exhibit an outstanding ballistic performance compared to glass and are therefore being investigated by NASA for such application [22].

From the theoretical point of view, Krell et al. [23] provided an in-depth discussion of transparent ceramics and the mechanisms allowing or limiting the transparency of polycrystalline ceramic materials and the relationship with the microstructure. In extension, Wang et al. [9] and Xiao et al. [24] gave comprehensive and detailed studies of various types of transparent ceramics, their manufacturing, and their use. Transparent ceramics have the potential to meet all these requirements and superior optical characteristics [25].

In 2016, the TC market was valued at USD 219.2 Million, and presently it is expected to reach USD 698.1 Million by 2022 (at a compound annual growth rate of 21.3% from 2017 to 2022) [26]. In 2017, Salem (Material Engineer at NASA, GRC) conveyed that transparent ceramics such as spinel and AlON exhibit better fracture toughness and crack growth resistance characteristics than glasses like fused silica [22]. Fused silica-based transparent materials have good optical characteristics and thermal shock resistance. Fused silica-based window materials have performed well in the space shuttle orbiter and the international space station (ISS) [22], but exhibit a catastrophic failure due to the formation of thermal gradients in the material [27]. Nevertheless, TCs provide good optical characteristics and thermal shock resistance properties in addition to slow crack growth and high hardness, which extended their use in even more severe conditions [22]. TCs additionally provide a weight reduction of the vehicle, as the total thickness of the windows is significantly reduced. These superior properties, i.e., slow crack growth, high hardness, high fracture toughness and weight reduction, of TCs over glasses provided potential in window systems and impacted the TC market [28–30]. Many tribological applications like personnel protection, face shields, riot visor, explosive ordnance visor, armor, ground vehicles, aircraft, spacecraft, re-entry vehicles, electromagnetic windows, laser igniter windows, artillery projectiles, and more can exploit the high performance of TCs due to these tunable properties [24,31].

The transparency and tribological behavior of TCs are influenced by different factors, which are collected in **Table 1.** The transparency of the TCs depends on the scattering of light, which scatter in correspondence of residual pores, secondary phases, impurity inclusions, and grain boundaries [32–34].The factors which affect the wear behavior of TC are mostly grain size, grain boundaries, crystal structure, residual pores, inclusions, and surface roughness [10,24,31,35–40]. It is also revealed that a high level of hardness and fracture toughness strongly influence the wear resistance of TC as they reduce the initial scratches as well as the subsequent fracture and propagation of cracks after initiation [41,42]. High fracture toughness and hardness value promise for the long-term protection of transparent ceramics. The presence of multiple phases leads to a decrease in transparency due to scattering.

Table 1: Effect of different factors on transparency and tribological behavior

Factor	**Sub-Factor**	**Impact**
Microstructure	Crystal Structure	• An isotropic crystal structure is mostly required for the manufacture of TC, as in an anisotropic crystals scattering occurs at grain boundaries [43] • A cubic crystal structure is ideal the highest transparency [7,43,44] • Defects in the crystal structure, like vacancies, increase the scattering thus decreasing the transparency [32–34]

	Phase	• The phase of the sintered TC must provide high density to the material with increased hardness and fracture toughness for better wear resistance [44] • A single-phase material is required for high transparency. The presence of multiple phases with different refractive index causes scattering of light [45,46]. A second phase affect both the transparency and the tribological behavior of the material [27,47]
	Grain Boundary	• A uniform refractive index is required for high transmittance of TC as the non-uniform refractive index will show more scattering of light [45,46] • second phases at the grain boundary will increase the scattering of light [48] • Toughening mechanism and strengthening mechanisms, such as grain bridging, increase the fracture toughness of the TC, which will increase the wear behavior of the material [35,49–51]
	Grain Size	• For most TCs the grain size does not affect transparency, but the full densification is often accompanied by grain growth, while fine grain size improve the tribological characteristics of TC [39,40,52,53] • Fine-grain size increase the hardness [35,54] and have an effect also on the fracture toughness [35,44,54] • Spark plasma sintering (SPS) is used to control the grain growth of TC while sintering [55,56]
	Porosity	• Inter-grain pores located at grain boundaries are easier to remove, but intra-grain pores are not always removed, which causes low transparency of TC [54] • Porosity has a direct relation with opacity and inverse relation with transparency, as pores have a strong effect on the scattering of light due to the high difference in the refractive index compared to that of ceramics [26] • Reduction in porosity and increase in density is required to increase the wear resistance of the TC [35–38]
Process	Raw material	• A fine size of the raw material will lead to low porosity and improved sintering [57] • Optimum powder size is required to manufacture TC, as a too fine raw material lead to low density and easy agglomeration [58,59] • Highly dispersed powder ensure high sintering ability required for enhanced wear resistance of TC • Impurities in the material will generate dissimilar phases and form light scattering centers, which will reduce the transparency of the material [24].
	Doping	• Doping techniques affect the mechanical and tribological behaviour of the material [60] • The addition of the correct amount of doping agent increase the wear resistance of the TC with improved mechanical properties [61,62]. On the other hand, the presence of a dopant should not

		lead to the formation of a second phase, which would compromise the transparency.
	Sintering	- Pressureless sintering in air and inert gas will lead to high porosity; therefore, vacuum sintering or hydrogen atmosphere is required [61,62] - Pressure-assisted methods (SPS and HIP) achieved exceptional mechanical properties with improved tribological properties [63–65] by limiting grain growth while providing efficient densification. Compared to pressureless sintering, the sintering temperatures are usually lower and times shorter, in particular for SPS [55,56] - The use of sintering additives facilitates the removal of pores, reduces the sintering temperature and often limits grain growth, which in turn increases the hardness of the TC [36].
	Surface finish	- The final transparency of a TC depends on the optical quality of the surface, i.e. on the surface finish of the sintered sample: the greater the roughness of sintered ceramics, the lower is its transparency [28]. The mechanical performance is also affected by the presence of scratches or defects on the surface.

The optical appearance of transparent ceramics is comparable to that of glasses [13,14,66–71]; however, TCs exhibits higher hardness, higher fracture toughness, higher resilience, and minor mass loss in scratch wear test than glasses [66,72]. The comparison of hardness and fracture toughness of TCs with glass materials is shown in **Fig. 1** [66]. Improving the material's hardness and fracture toughness enhance the TC's tribological performance [41,42,66,73], particularly a high hardness and low mass loss of TCs during the scratch wear test are beneficial to wear resistance of TCs [38,65,66]

TCs are highly transparent in the visible and mid-IR ranges (0.25–5.5 m), which suggests the utilization of TCs as windows and domes in electro-optical and infrared sensors in military systems [74]. Promising recent transparent materials used for military systems are $MgAl_2O_4$ [35], Al_2O_3 [75,76], AlON [77], Lu_2O_3[78,79], c-BN [80], Y_2O_3 [81,82], SiC [27], Si_3N_4 [65,83], and SiAlON [84–86] because of their high strength, hardness, and fracture toughness. Different mechanical, thermal, and optical properties of these transparent ceramics are listed in **Table 2**. These TCs have the potential to perform as good wear-resistant materials for different tribological applications. The study of tribological behaviour of transparent ceramics, such as $MgAl_2O_4$ [54,66], AlON [27,59,87–89], and Si_3N_4 [36,90,91] shows that these TCs exhibit significantly improved tribological performance compared to single crystals and glasses.

Table 2: Physical properties of transparent ceramics with potential in tribological applications.[27,37,59,63,65,75,83,86,92–112]

Properties of some transparent ceramic materials	**$MgAl_2O_4$**	**Al_2O_3**	**AlON**	**Lu_2O_3**	**c-BN**	**Y_2O_3**	**Si_3N_4**
Hardness [GPa]	12-18	14-27	15-20	12-15	28-46	7-10	14-34
Fracture Toughness [MPa $m^{0.5}$]	1.48-3.5	1.5-3.3	1.7-3	3.9-4.3	0.48-1.2	1.1-1.5	3.2-4.1
Transverse Rupture Strength [MPa]	80-250	450-850	330-370	-	230-370	130-170	414-682
Melting Temperature [^{o}C]	~2140	~2277	~2150	~2500	~5689	~2410	~1900
Theoretical density [g/cm^3]	3.578	3.987	3.69	9.42	3.45	5.04	3.28
Thermal Conductivity [W/mK]	10-15	12-38	9-10	10-12.5	1.2-1.4	8-12	14.5-26
Young Modulus [GPa]	250-310	390-410	320-340	52-182	560-910	165-196	260-295
Shear Modulus [GPa]	120-140	84-92	125-138	21-71	360-370	63-71	105-110
Thermal Expansion Coefficient [K^{-1}]x10^{-6}	6-8	4.5-11	5-7	7.1-8.3	4.6-4.8	3.5-5	3-4
Refractive Index	1.715	1.78	1.79	2.12	2.117	1.93	2.02
Theoretical Transmission [%] (wavelength range, µm)	49-87 (0.2-5.5)	69-84 (0.2-5)	60-81 (0.4-5.2)	63-77 (0.8-2.3)	59-69 (0.3-1.5)	70-83 (0.3-7)	38-46 (0.8-2.5)

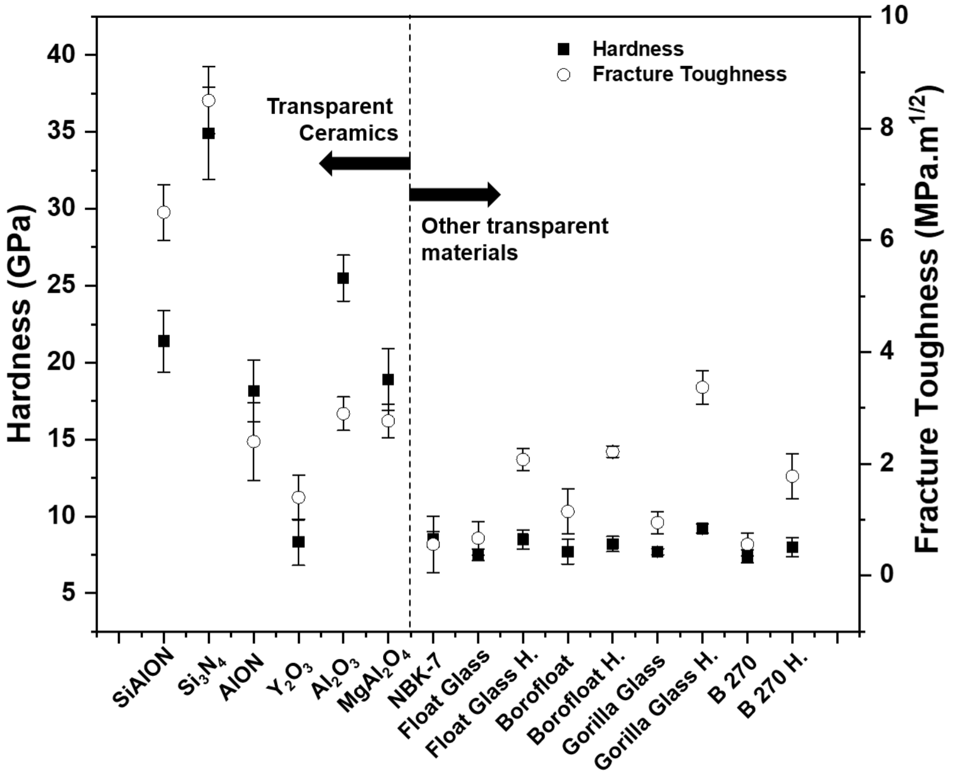

Fig. 1: Hardness and fracture toughness of different transparent ceramics such as SiAlON, Si_3N_4, AlON, Y_2O_3, Al_2O_3, $MgAl_2O_4$, NBK-7, Float glass, Float glass hardened, Borofloat, Borofloat hardened, Gorilla glass, Gorilla glass hardened, B270, B270 Hardened [37,44,63,65,75,86,92,94,96–101,111–113].

Grain size primarily determines ceramic materials' mechanical characteristics; in general, the smaller the grain size, the stronger the ceramics. TCs have shown a prominent relationship between grain size, hardness, and fracture toughness. A bimodal distribution of the grain size is required because, on one side, larger grain size promotes transparency, whereas on the other side, fine grain size improves the tribological characteristics [39,40,52,53]. Fine-grain size increases the hardness [35,54], but the effect of grain size on fracture toughness is uncertain as the fracture toughness increase [44], decrease [35], or remain the same [54] with a reduction in grain size. Borrero-Lopez et al. investigated the effect of three different grain sizes on the lubricated sliding wear of transparent $MgAl_2O_4$ ceramics [54]. Different grain sizes provide different hardness of the transparent $MgAl_2O_4$, resulting in different wear mechanisms (discussed in section 2.1). Moreover, TCs for windows and other tribological applications must have high-velocity impact strength along with high hardness and fracture toughness. For such uses, however, literature is still scanty.

The wavelength range of transparency of the material is defined by electron structure, while impurities induce absorption bands. Both factors are equally relevant in the case of single crystals. Scattering effects further limit the optical quality. The scattering depends on the difference between the refractive index of the matrix (ceramics) and the scatterer, and also on the wavelength of passing light and dimensions of the scatterers, as illustrated by Stuer et al. [45] and Pabst et al. [46]. The possible sources of light scattering are shown in **Fig. 2**. In TCs, composed of randomly oriented crystalline grains, light scatter on residual pores, secondary phases, impurity inclusions, and grain boundaries [32–34]. Therefore, the presence of these defects in TCs affects not only the tribological performance but also the transparency. To achieve the maximum theoretical transparency, TCs have to be defect-free. In general, the defect-free TCs exhibit excellent mechanical, thermal, and tribological properties as nearly-perfect materials. In the case of birefringent materials (e.g., Al_2O_3), light is further scattered at the grain boundaries of randomly oriented birefringent grains.

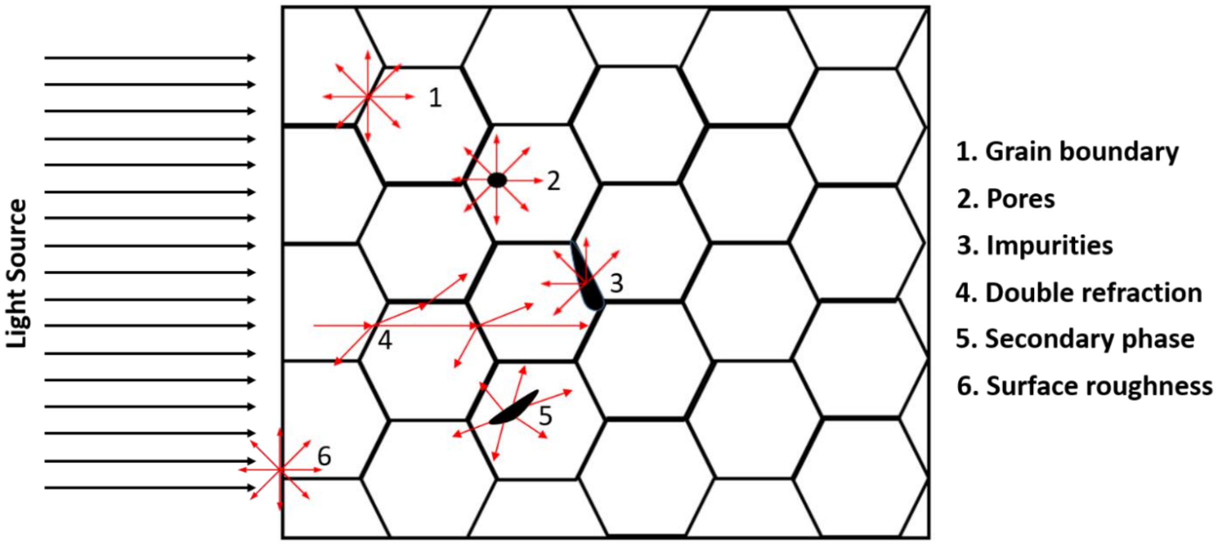

Fig. 2: Different sources for scattering the light.

Most of the TCs are single-phase materials with a cubic (optically isotropic), spinel, garnet, or bixbyite crystalline structure. However, it is also possible to achieve a significant degree of transparency in the case of non-cubic materials, either by the orientation of grains [43] or by producing ceramics with a very fine grain size that are significantly below the wavelength of the passing light [7]. The latter also applies for nanocomposites, where the presence of a second phase limit the transmittance only at shorter wavelengths (UV, visible) (e.g., MgO/Y_2O_3 nanocomposite [114] transparent above 1-2 µm or $MgAl_2O_4/Si_3N_4$ [48]).

Many TCs are refractory materials and the robust bond strength and coupled with a low diffusion coefficient, pose difficulties during densification at temperatures below 1500°C, often even below 1800°C. Therefore, sintering aids are generally required to obtain high-density TCs at lower temperatures or pressures [58,59]. Transparent ceramics is manufactured by various ceramic processing techniques, including synthesis or mixing of starting powders, eventually further powder processing (milling, granulation), shaping, heat treatments (calcination/debinding, sintering, annealing), and polishing. Compared to single crystals, TCs usually do not require secondary operations, like cutting and machining, before the final polishing step, as TCs is prepared in near-net shape. However, compared to traditional ceramic materials, the production of transparent ceramics necessitates specific equipment, particularly for the powder synthesis and sintering processes. In particular, high-purity powders with good sinterability, low level of agglomeration and regular morphology are required to avoid introducing defects and second phases. The two main approaches are the synthesis of precursor powders and the reactive sintering of a mixture of powders, and both are widely described in literature [115–119]. Shaping approaches cover many of the commonly used techniques for transparent ceramics (e.g., dry pressing [120,121], slip casting [118], gel casting [39,122], tape casting [121,123], pressure slip casting [124], and additive manufacturing [125,126]) with particular attention on limiting potential contamination and the presence of voids. While all the process parameters have to be aligned to reach a defect-free microstructure, the focus is firmly on the characteristics of the starting powders and the sintering step.

In most cases, pressureless sintering in air does not entirely remove porosity from ceramics. Therefore, pressure-assisted sintering techniques are requested, viz. hot pressing [127,128], hot isostatic pressing [129,130]), vacuum sintering [131], spark plasma sintering [95,111,132,133], microwave sintering [134,135] or a combination thereof. Moreover, sintering aids are also very often used to enhance the densification and removal of pores, limit grain growth, and lower the sintering temperature. The high pressure-temperature technique is extensively utilized to manufacture superhard and ultrahard TCs [136,137]. These TCs have excellent wear resistance. TCs, as triboelements, is widely employed in diverse fields. Different tribological applications where TCs is employed include windows in re-entry vehicles, lookdown windows in aircraft and military vehicles, armor, face shields, missile tops, infrared domes protections, window floors, and space shuttle windows. Among TC materials, the effect of various processing factors on transparency has been studied extensively [138]. However, tribological properties of TC are relatively poorly studied.

Transparent ceramics with better mechanical properties have been identified as the next-generation transparent materials for tribological applications. Salem studied the mechanical characteristics of translucent AlON and $MgAl_2O_4$ ceramics considering their utilization in spaceship windows [22]. However, the processing and characterization of TCs are difficult and costly [24,59,115,139,140]. Therefore, modelling and simulations are used to predict mechanical and tribological performance in extreme conditions [33]. Moreover, the literature on TCs reveals that the modelling of scattering by residual pores and the resulting transmittance predictions is made using the Mie theory [32,33,46,141]. Approximation techniques be used to model the effect of tiny pores and huge pores (compared to the wavelength of light) based on the Rayleigh approximation and the Fraunhofer approximation, respectively. Recent research indicates that the Rayleigh-Gans approximation provides better results than the Rayleigh approximation in small-size regions. The van de Hulst approximation (also known as the anomalous diffraction approximation) [142] is the only approximation capable of predicting the decrease in in-line transmittance as pore size increases in the small-size region and the increase in transmittance as pore size increases in the large-size region. Indeed, the Van de Hulst approximation provides transmittance predictions that are the most closely related to the exact Mie theory predictions over a wide range of pore sizes [33]. These modelling techniques are used to predict the optical, mechanical, and tribological properties of newly synthesized TCs, thereby saving money and time.

The purpose of this review is to deliver a theoretical framework for the tribological properties of transparent ceramic materials. Different types of TCs used for tribological applications have been explored. This review discusses the impact of microstructure and mechanical characteristics of TCs on tribological performances, without neglecting the importance of the optical transparency. In this view, wear testing, and scratch testing of TC materials have been reviewed to understand the mechanical and tribological properties. This approach provides insight into different TC's surface deformation characteristics and material removal mechanisms. In addition, a significant part of the study has been devoted to understand the dominant processes of material removal as a function of microstructure and mechanical properties of transparent ceramics when they are subjected to wear conditions. The following section will discuss different transparent ceramics used in different tribological conditions.

2. Different transparent ceramics for tribological applications

. Transparent ceramic material must be developed beyond the state of art with high durability, efficiency, improved performance, lightweight, and high strength, in order to fulfil the requirements of the different application fields [22].Transparent ceramics used for tribological applications require excellent hardness, fracture toughness, and elastic modulus (better contact damage resistance) [58,59]. In addition, the properties like high compressive strength (relevant for applications requiring high load at tribo-contact), low density (better specific properties than many metals), and high melting and mechanical property retention at elevated temperature (high-temperature tribological applications) are also required for the tribological applications mentioned above. Friction and wear behaviour of TCs, which are the critical components for operation in various tribological applications, have been discussed extensively [143–145]. However, there is scarcity in the research of tribological and mechanical behavior of transparent ceramics. Since the main focus is on tribological applications, TCs with low strength have been excluded in this review. The most promising transparent materials with the highest strength and potential tribological properties are $MgAl_2O_4$,Al_2O_3, AlON, Lu_2O_3, c-BN, Y_2O_3, Si_3N_4, and SiAlON, and are therefore discussed in the present review [27,59].

2.1 $MgAl_2O_4$

$MgAl_2O_4$ (spinel) has a high potential as transparent armor ceramics and protective windows and domes for sensor application. It provides a high levels of optical and mechanical performance required by these types of applications [146,147]. Earlier research has shown that such transparent windows require excellent mechanical and tribological properties, i.e., hardness, fracture toughness, wear resistance with high transmission, and a suitable refractive index [35]. $MgAl_2O_4$ is transparent from UV to mid-IR (from 0.2 to 5.5 µm) [11,146] and exhibits a density of 3.578 g/cm^3. The advancement of fabrication technology and the quality of raw powders have resulted in the production of large size $MgAl_2O_4$ ceramics with high optical quality, making them suitable for use in transparent armor, domes, and windows for applications in ultraviolet (UV), visible (VIS), and infrared (IR) [117,146].

Fabricating transparent $MgAl_2O_4$ ceramics via pressureless sintering is challenging [34,148] and therefore, advanced sintering techniques like hot pressing (HP), hot isostatic pressing (HIP), and spark plasma sintering (SPS) are required for its manufacturing [97,149–152]. Sintering aids used to produce transparent spinel ceramics are LiF [153], B_2O_3 [154], and CaO [155,156]. It is possible to prepare transparent spinel ceramics without sintering aids [157], but the use of sintering aid helps to achieve maximum transparency.

To understand the tribological behaviour of transparent $MgAl_2O_4$, a sandblasting experiment was carried out for five minutes on the surface of transparent $MgAl_2O_4$. It was observed that the mass loss from the surface was 2 mg (0.06%), which is very low compared to other glasses with a mass loss value ranging from 6.8 to 114.8 mg (0.3-4.7%). The surface roughness and maximum crater depth in the transparent $MgAl_2O_4$ spinel were found to be 0.1±0.01 µm and 3 µm, respectively. The surface roughness of the different glasses was found to be in between 1.1±0.1 µm to 3.7±0.4 µm, while the maximum crater depth was 4 µm to 229 µm [66]. It shows that transparent $MgAl_2O_4$ exhibits an excellent wear resistance, much higher compared to glasses, with low surface roughness and crater depth. **Fig. 3** represents various cracks (radial, median, and lateral cracks) formed during the scratch test of transparent material with increasing load. Three regimes were developed during scratch, i.e., micro-ductile, micro-cracking, and micro-abrasive. In the micro-ductile regime, the cracks formed are underneath. During micro-cracking, radial and lateral cracks are formed, which results in chip formation of the transparent material. However, debris formation is observed in micro-abrasive regime.

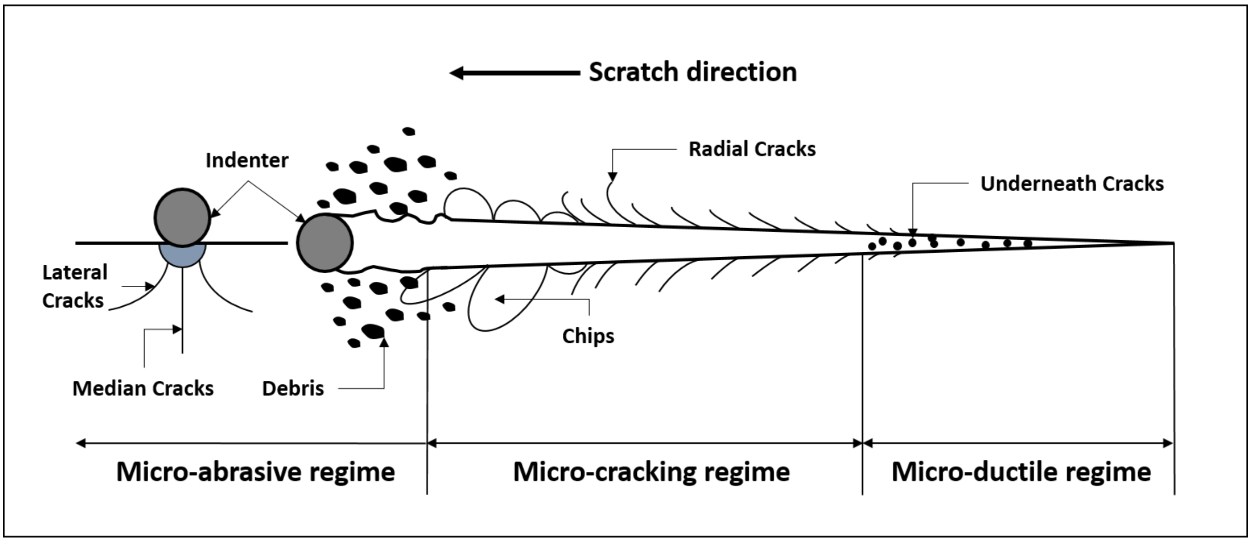

Fig. 3: Typical scratch patterns on brittle materials during a progressive scratch [66].

The optical transmittance and tribological and mechanical properties are improved with the reduction of porosity. Moreover, the wear resistance is further improved by the reduction of grain size. Benaissa et al. [35] prepared transparent $MgAl_2O_4$ without any sintering aid using SPS at different temperatures. The microstructure of transparent $MgAl_2O_4$ without any sintering additive at different sintering temperatures is shown in **Fig. 4a, Fig. 4b, and Fig. 4c**. Sintering of the powder was done at 73 MPa pressure with three different sintering temperatures, i.e., 1300 °C **(Fig. 4a)**, 1350 °C **(Fig. 4b)**, and 1400 °C **(Fig. 4c)**. The heating rate was 100 °C/min to 800 °C, 10 °C/min to 1100 °C, and 1 °C/min to final temperature. With an increase in sintering temperature, the relative density of the material dropped slightly and it was found to be 99.93%, 99.63%, and 99.58% at 1300 °C, 1350 °C, and 1400 °C, respectively. At wavelength of 550 nm, the transmittance was 70%, 45%, and 6% for 1300 °C, 1350 °C, and 1400 °C, respectively, owing to the reduced relative density and increased porosity. The use of sintering aids for the production of spinel by SPS changed the microstructure both in terms of porosity and grain size [158,159].

The tribological properties also be affected by the use of dopants or additives as the grain boundary and grain size of the TC canbe altered. This reduces the porosity and improve the tribological behaviour. Esposito et al. [60] examined the effect of LiF (0 to 1 wt %) doping in $MgAl_2O_4$ on the microstructure of the transparent ceramics sintered by hot pressing. The transparent $MgAl_2O_4$ without additive obtained by HP at 1600 °C for 60 min exhibits a bimodal microstructure as shown in **Fig. 4d**. Pore-free TC with equiaxed grains of approximately 38μm and fine grains of approximately 3μm size with intergranular pores were observed when no LiF was used (**Fig. 4d**). The addition of LiF to the $MgAl_2O_4$ provides uniformity in the microstructure of TC. LiF acts as a sintering aid as 0.5% LiF produces TCs with a grain size of 20 μm without any residual porosity (**Fig. 4e**). Adding 1% LiF to $MgAl_2O_4$ processed under the same conditions results in a more uniform microstructure with an average grain size of less than 20 μm (**Fig. 4f**). The addition of LiF promotes a fine structure and low porosity and improve the hardness and in turn the tribological characteristics.

Nassajpour et al. [48] prepared $MgAl_2O_4/Si_3N_4$ nanocomposite using $MgAl_2O_4$ and Si_3N_4 powders of average particle sizes of 250 nm and 40 nm, respectively. The TC was obtained using SPS with maximum pressure and temperature of 80 MPa and 1550°C for 20 min. The microstructures of $MgAl_2O_4$-1wt% Si_3N_4 and $MgAl_2O_4$-3wt% Si_3N_4 are shown in **Fig. 4g and Fig. 4h** respectively. The hardness obtained for pure $MgAl_2O_4$, $MgAl_2O_4$-1wt% Si_3N_4, and $MgAl_2O_4$-3wt% Si_3N_4 was 7.7, 8.1, and 10.2 GPa respectively. Increasing the Si_3N_4 concentration in the spinel-based composite increased its hardness. This is because small-scale bridging bonds developed in the spinel composite structure during sintering, which increased the strength at the surface. After heat treatment, the hardness of pure $MgAl_2O_4$, $MgAl_2O_4$-1wt% Si_3N_4, and $MgAl_2O_4$-3wt% Si_3N_4 samples increased to 8.2, 9.3, and 12.1 GPa, respectively. This rise in the hardness indicates the presence of superficial oxidation on the surface which caused compressive stress on the nanocomposite's surface. The sample $MgAl_2O_4$-1wt% Si_3N_4 exhibits the greatest shear strength. The regions under the shear stress-displacement curves for pure $MgAl_2O_4$ and $MgAl_2O_4$-1wt% Si_3N_4 are almost identical and nearly twice as large as those for sample $MgAl_2O_4$-3wt% Si_3N_4. It indicates that adding 3% Si_3N_4 significantly reduces the fracture toughness of $MgAl_2O_4$-based nanocomposites. The addition of a second phase to the ceramic matrix impact the sintered composite's reinforcing mechanism. While adding a second phase to the matrix toughen the ceramic through multiple processes ranging from crack deflection to fracture bridging, grain growth inhibition is the primary mechanism in this instance. It means that Si_3N_4 particles significantly impair grain development. The inclusion of Si_3N_4 at a concentration of up to 1% had no detrimental effect on the fracture toughness of nanocomposite samples. However, when 3% Si_3N_4 was added to the matrix, fracture toughness fell substantially, since it was also accompanied by a significant increase in the volume percentage of voids, which accounts for most of the dispersion hardening effect [48].

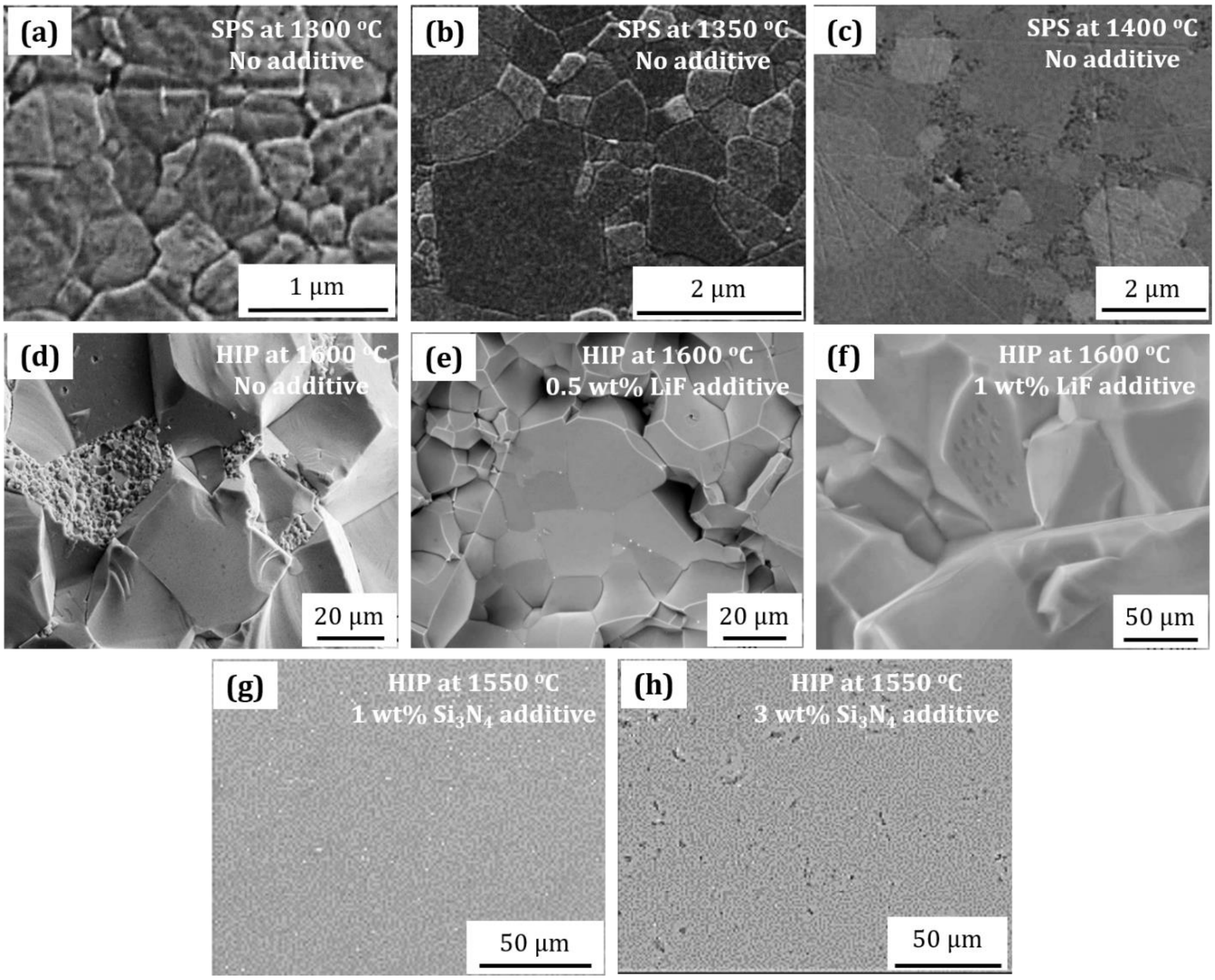

Fig. 4: Microstructure of $MgAl_2O_4$ obtained a), b), c) via SPS at different temperature without additive [35], d) via HIP without additive [60] e), f) via HIP at different temperature with 0.5 wt% LiF and 1 wt% LiF [60], g) and h) via HIP at different temperature with 1 wt% Si_3N_4 and 3 wt% Si_3N_4 [48].

Toughening and strengthening mechanisms also improve the tribological properties of the TCs [49,50]. Sheikh et al. [51] studied the effect of toughening on hardness, fracture toughness, and transparency for transparent $MgAl_2O_4/Si_3N_4$ nanocomposite sintered by SPS. The average particle size of $MgAl_2O_4$ and Si_3N_4 nanopowder was 40-50 nm and 30-40 nm, respectively. The synthesised transparent $MgAl_2O_4$-2 wt% Si_3N_4 showed spherical grains of 5 µm size and density of 3.561 g/cm^3 (99.8% of the theoretical density). The nanocomposite experiences a reduction of 60% transparency compared to pure spinel. Also, the heat treatment did not led to any variation in the optical transmittance of the nanocomposite. However, a significant improvement in the mechanical properties of the nanocomposite was observed after heat treatment 1000^{o}C such as an increase of approximately 4% increase in the elastic modulus of $MgAl_2O_4/Si_3N_4$ nanocomposite compared to pure $MgAl_2O_4$. The hardness (14.7±0.1 GPa) and fracture toughness (1.68±0.04 MPa.m$^{0.5}$) of $MgAl_2O_4/Si_3N_4$ nanocomposite was found to be in the same order as the hardness (14.1±0.1 GPa) and fracture toughness (1.67±0.05 MPa.m$^{0.5}$) of pure $MgAl_2O_4$. Heat-treated nanocomposite material improved instead the TC's hardness (16.3±0.1 GPa) and fracture toughness (2.1±0.06 MPa.m$^{0.5}$).The decrease of transparency and enhancement in mechanical properties is due to the presence of Si_3N_4 nanoparticles that scatter light but at the same time reinforce the material by toughening mechanism. As was shown in the case of pore size [45], if the size of the scatterers is sufficiently small, I deleterious effect on transparency is reduced.

In $MgAl_2O_4$ with a coarse microstructure (grain size ≈50µm), intergranular fracture was observed and a fracture toughness of 1.4-2 MPa.m$^{0.5}$ was measured [160]. The low fracture toughness of transparent $MgAl_2O_4$ has been linked with grain-boundary embrittlement induced by additive, impurities, or residual stress [146]. A tearing resistance curve, or R-curve, indicates a material's resistance to progressive crack growth (implying that the fracture toughness of the material varies with crack development). As a result, a tearing resistance curve is a function of fracture toughness and crack growth [161]. Coarse-grained microstructures of $MgAl_2O_4$ exhibit limited resistance to crack propagation due to grain bridging and wedging induced by friction and therefore low tearing resistance is provided by coarse grained transparent $MgAl_2O_4$. Porosity and second phases are not necessarily the only flaws that must be limited (0.01 % porosity) in transparent ceramics for tribological applications: coarse-grained microstructures have also been recognized as a source of weakness [162]. Microstructure refinement leads to significant increases in hardness for grain sizes as low as 1 µm as determined by Hall–Petch relationship. Even though hardness of $MgAl_2O_4$ increases significantly with microstructural refinement which increases the erosion resistance during penetration, the exact mechanism by which wear varies is unclear.

Nonetheless, one of the primary goals of transparent spinel processing is to decrease the particle size of the finished product. The cost of transparent armor, on the other hand, outweighs the minor hardness advantage associated with small particle sizes, and grain sizes in the hundreds of microns are often acceptable. It is difficult to determine the effect of grain size on ballistic performance because of the complexity of the failure mechanism, the high costs of the tests and the limited available reports on that. Even though spinel is susceptible to fracture formation, which is assisted by moisture, the effect is most apparent in coarse-grained microstructures. Although there seem to be no delayed fracture development studies for single crystals, the findings emphasize the vital role that grain boundaries play on influencing the strength of materials [31]. Other than armor application, the TCs has a potential to be used for biomedical application as wear resistant load bearing implant, which generally experience fretting wear in the joint. At present, two materials, i.e., $MgAl_2O_4$ and AlON compete with single crystals for such applications. Bodhak et al. [28] compared the tribological characteristics of these two ceramics in freshly prepared medium, i.e., stimulated body fluid at 37ºC. It was observed that the wear rate of $MgAl_2O_4$ was 62% lower than that of AlON for 1000 m test run and 47% less for 3000 m test run (**Fig. 5**).

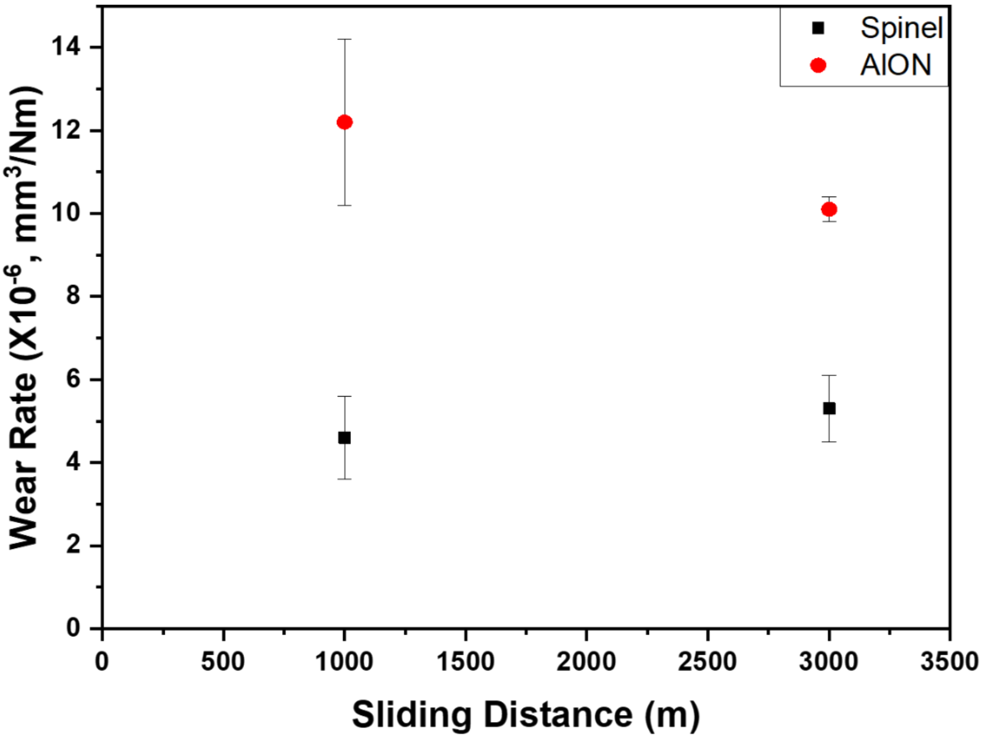

Fig. 5: Wear rate of Spinel and AlON [28].

As mentioned above, the porosity present in the TC influences the transparency, hardness, elastic modulus, and fracture toughness of the material (**Fig. 6**). The tribological characterization on the flat surface of the spinel TCs was measured using alumina balls of 6 mm as contact means for 6 min at 20 N load and 100 rpm [35]. The resulting coefficient of friction was 0.06 and 0.13 for samples fabricated at sintering temperatures of 1300°C and 1350°C, respectively. **Fig. 6** shows that the wear resistance of transparent spinel was improving with decreasing sintering temperature, which results in an increase in hardness due to smaller grain size, and decrease in fracture toughness. Also, low friction coefficient was observed with decreasing sintering temperature. The reduction in fracture toughness is due to the slight increase in porosity for the samples sintered at 1400°C compared to 1300°C. Slight porosity deflects the direction of movement and spread a high energy crack in several low energy cracks which cannot propagate too far as compared to the high energy ones. However, the presence of pores compromises the transparency of the ceramics. The sintering temperature must be kept low to fulfil the requirement of high hardness. So, it is concluded that porosity is a more prompting factor than grain size for good wear resistance. A small grain size with high density, hardness, and transmittance is observed at low sintering temperatures. In contrast, large grain size with high fracture toughness and low transmittance is observed at high sintering temperatures. Therefore, the optimum sintering temperature is required to achieve high wear resistance and transparency.

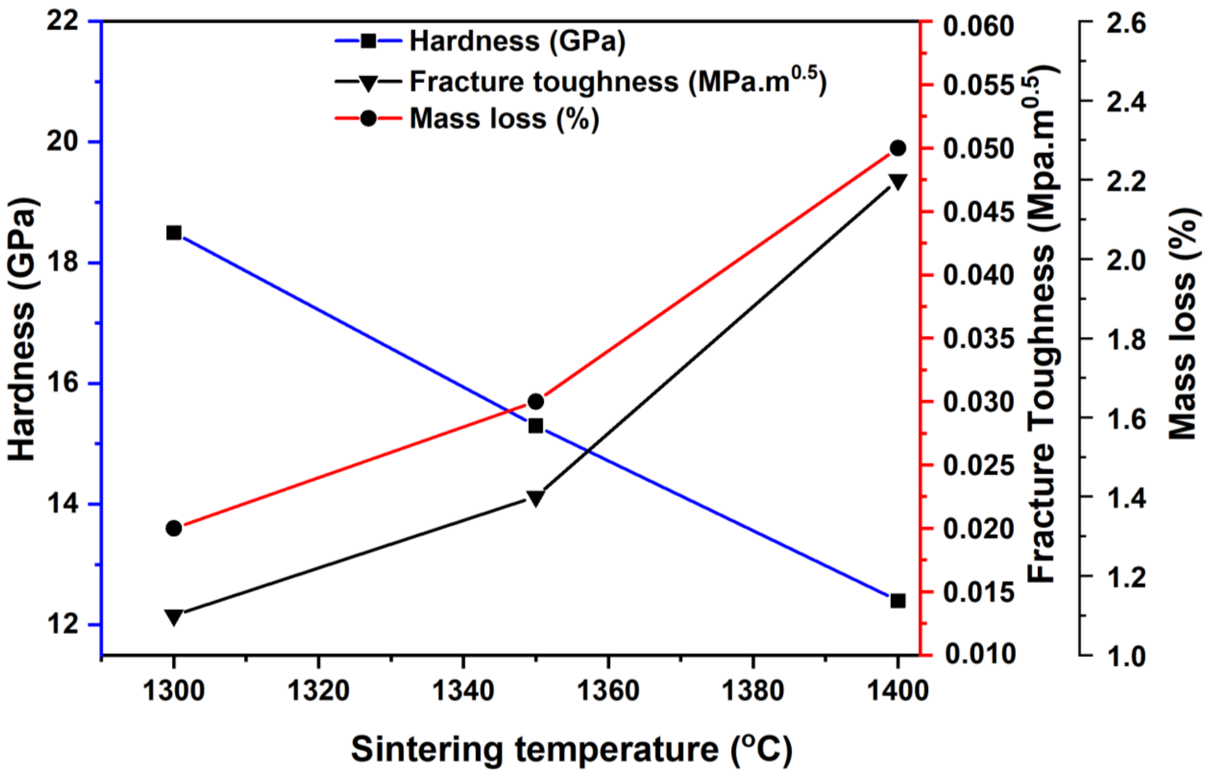

Fig. 6: Hardness, fracture toughness and mass loss upon friction vs. sintering temperature of spinel [35].

Bodhak et al. [28] fabricated a disc shaped sample of $MgAl_2O_4$ by conventional powder processing routes followed by sintering, grinding, and polishing with average surface roughness (r.m.s) ≈0.001 µm for an application like total hip arthroplasty and total knee arthroplasty. The TC formed was analyzed for tribological characteristics as these applications experienced fretting wear in the joint. A linear-reciprocating ball on a disc testing tribometer was used for all the experiments. A linear oscillatory motion of 10 mm was made with a constant load of 20 N and a constant speed of 5000 mm/min with Al_2O_3 as a counter body. Wear rate for distances 1000 m and 3000 m was measured to be $4.72 \pm 1.22 \times 10^{-6}$ mm^3 Nm^{-1} and $5.27 \pm 0.85 \times 10^{-6}$ mm^3 Nm^{-1}, respectively. Volume loss for similar distances was estimated to be 0.094±0.02 mm^3 and 0.316±0.05 mm^3, respectively. Hardness and friction coefficient value of fabricated $MgAl_2O_4$ sample was 13.09±0.71 GPa and 0.43±0.009.

The strength of the spinel is enhanced by grain refinement while preserving its transparency in infrared (IR) wavelength range, as shown recently in a nanostructured transparent spinel with an average strength of 470 MPa and Weibull modulus of 6.2 [88]. Nanostructured spinel is fragile and its strength is susceptible to deterioration through the development of defects during service. It is very important in IR windows/domes since the spinel are exposed to extreme loading conditions during high-speed missile flight. As a result, there is a need for transparent ceramics that are not only strong but also damage-tolerant and perform well under the harsh circumstances of service. In this aspect, the insertion of reinforcements, such as particles, whiskers, or fibers, into ceramic matrices, improve the damage tolerance of the toughened composites. When the size of the reinforcement is limited and no clustering occurs, transparency is maintained at longer wavelengths. For creating a well-dispersed slurry, a spinel powder was combined with 2.5 vol% Si_3N_4 (average particle size 50 nm) and 0.5 vol% Y_2O_3 (average particle size 10 nm). The slurry was spray dried and the globular powder was pressed at 50 MPa and heat-treated at 500^{o}C for 24 hours. The samples were then HP at 60 MPa pressure at 1300^{o}C for 3 hours. Some samples were again heat-treated at 1000^{o}C for 4 hours to strengthen the $MgAl_2O_4/Si_3N_4$ composite. The relative density of the fabricated composite material was found to be 99.5%. TEM microscopy revealed that $Si_3N_4$was present as a nanodispersoid with grain size of 100 nm within a polycrystalline spinel matrix of 300 nm [141]. The transmission was 70 % for IR radiations of wavelength 3-4.5 µm. The reduction in transparency was attributed to the presence of Si_3N_4grainsand the residual porosity. The results showed a 29% increase in strength and an 85% increase in fracture toughness compared to processed TCs. From the previous discussion, we conclude that the rise in fracture toughness vary the tribological characteristics of the TC by reducing the wear resistance properties [141].

It is summarized that the transparent $MgAl_2O_4$ is fabricated without an additive, but it exhibits a bimodal microstructure with low transparency. The addition of a second phase impacts on the sintered reinforcing mechanism. The addition of LiF or Si_3N_4 to $MgAl_2O_4$ results in fine structure and low porosity, improving the hardness and tribological characteristics of the TCs and their transparency. The improvement in the mechanical and tribological properties is only up to a specific percentage increase of additive, i.e. below 2-3 vol%. Therefore, an optimum quantity of additives is required to be added.

Various cracks, i.e., radial, median, and lateral, are formed during the scratch test of transparent material with increasing load. The development of small-scale bridging bonds in the spinel composite structure during sintering is required to increase the surface strength. A post sintering heat treatment improves the mechanical and tribological properties of TCs. The porosity factor sometimes overcomes the fracture toughness factor for wear performance. The porosity in the TC also increases the fracture toughness value of the material but leads to deterioration in the wear resistance. So, for good wear resistance properties, low porosity, fine grain size, high hardness, and fracture toughness must be targeted by keeping low sintering temperature, allowed in particular by the use of SPS.

2.2 Al_2O_3

Alumina (Al_2O_3), is one of the earliest transparent ceramics which has found significant commercial success [163]. Alumina is used widely due to its low cost, biocompatibility, and appropriate mechanical, chemical, electrical, and thermal properties. It has potential for tribological applications, such as transparent electromagnetic dome structures, armors, envelopes, and windows. The tribological and mechanical properties of Al_2O_3 ceramics is optimized by controlling the grain size [39,40,164]. For altering the grain size of the transparent Al_2O_3, different processing techniques and sintering aids are used. A theoretical maximum in-line transparency of polycrystalline Al_2O_3 is found in the infrared wavelength range between 2000 and 4000 nm [122,165]. The main drawback of Al_2O_3 as a TC is the birefringence [23], which limits the thickness for which the material is transparent. A reduction of grain size is an approach that allows to further improve transparency, even at lower wavelengths.

SPS is demonstrated to be a reliable process for producing transparent polycrystalline alumina with real inline transmittances greater than 50% (for 640 nm, 0.8mm thickness) [166]. Despite the short sintering cycles (usually 15 minutes) of SPS, it was shown that doping is essential to provide satisfactory optical characteristics in polycrystalline alumina [166,167]. The SPS of pure alumina cannot prevent substantial grain development, leading to the presence of pores at the grain boundary (**Fig. 7a**). Therefore, sintering of Mg-, Y-, and La-doped submicron alumina was examined using SPS [166] which successfully suppressed grain growth. The microstructures of sintered samples at 1350 °C with Mg, Y, and La as doping agents are shown in **Fig. 7b, Fig 7c, and Fig. 7d**, respectively. Compared to single doping techniques, co-doping each pairing often improves the transparency by lowering the grain size [166]. Triple doping with Mg, Y, and La in equal proportions resulted in the highest real inline transmittance of 57%. Such high transmittance coupled with very fine grain size is made possible with SPS and needs high sintering pressures and low sintering temperatures. The findings of this work should pave the way for more research and development of transparent polycrystalline alumina generated by fast sintering methods such as SPS. Polycrystalline Al_2O_3 ceramics prepared by pressureless pre-sintering followed by HIP at 198 MPa for 3 hours between temperature range from 1190 °C to 1295 °C revealed an in-line transmission of up to 70.4% at a wavelength of 632.8 nm for 0.8 mm sample thickness [165]. Al_2O_3 ceramic was doped by ZrO_2 (0.3 wt%) and $MgAl_2O_4$ (0.175 wt%) by gel-casting and then sintered. Grain size refinement in the completely dense alumina structure is observed in **Fig. 7e**. A similar method, i.e., pre-sintering followed by HIP, was also followed for Al_2O_3 with 0.03 wt% MgO and 0.2 wt% ZrO_2 which resulted in 60% in-line transparency at 650 nm wavelength for 0.8 mm sample thickness. The sintered sample had a grain size of approximately 0.5 µm (**Fig. 7f**) and 99.9% relative density with 20–21 GPa hardness. The developed TC (600–700 MPa four-point bending strength and 750–900 MPa three-point bending strength) is suitable for scratch-resistant widows and transparent Al_2O_3 armour. Therefore, it is possible to fabricate sophisticated hollow components and big flat windows with good wear resistance properties of sintered and HIPed Al_2O_3 using Al_2O_3 powder and a gel-casting method.

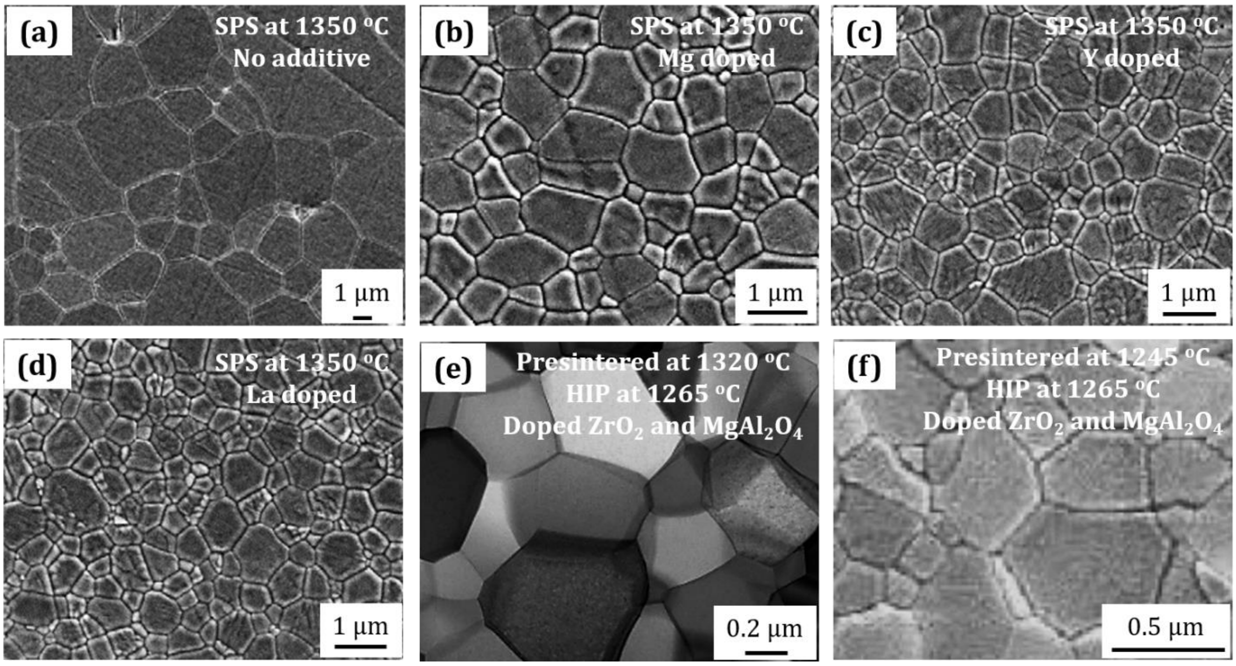

Fig. 7: Microstructure of Al_2O_3 obtained via SPS at 1350 °C a) pure and doped with b) Mg, c) Y and , d) La [166], or e) doped by ZrO_2 and $MgAl_2O_4$, [165] and f) by ZrO_2 and MgO, presintered and HIPed [39]

Transparent Al_2O_3 ceramics have been produced (flat windows 0.8 mm thick) with real in-line transmittance of nearly 60% with submicron grain size (0.4-0.6 µm), high hardness (HV10 20-21 GPa), and strength (four-point bending 600-700 MPa; three-point bending 750-900 MPa) [39]. It was found that doped Al_2O_3 transparent ceramic prepared using SPS technique resulted in higher transparency than pure Al_2O_3 [166,167]. However, Al_2O_3 transparent ceramic, doped with aluminium ethoxides, prepared using SPS technique results in higher transparency than pure Al_2O_3[166].It was investigated that doping with aluminium ethoxide (0.1-1 wt%) leads to form α-Al_2O_3 nanoparticles, which minimizes grain growth and changes the sintering mechanism from volume to grain boundary diffusion. The nucleated particles, which provide the energy barrier during sintering, block grain reorientation required for the diffusion of the grains during sintering. α-Al_2O_3 nanoparticles at the grain boundaries of the Al_2O_3 thus decrease the grain mobility and, in turn, prevent the joining of the grains. Due to the steric impediment provided by the α-Al_2O_3 nanoparticles and reduction in the grain size of the TC, it is concluded that the addition of aluminium ethoxide to Al_2O_3 reduces the wear resistance of the TC.

The optical, microstructural, mechanical, and fracture properties of Er^{3+} doped transparent alumina produced by co-precipitation method were investigated [75]. The real in-line transmittance of Er^{3+} doped samples was in the range of 55–59% for 1 mm thickness, which belongs to higher transmittance values in comparison with transmittance found in the other research [39]. Segregation of Er atoms at the grain boundaries probably caused a reduction of grain boundaries mobility, which led to decreasing the mean grain size (0.33–0.35 µm) compared to undoped alumina. The Vickers hardness of the Er^{3+} doped alumina was measured at different loading conditions, achieving 26.9 GPa at 10 N load. The fractography analysis showed a higher transgranular character of fracture surface in Er^{3+} doped alumina compared to undoped alumina, confirming the enhanced grain boundary cohesion due to Er doping. The indentation fracture toughness of Er^{3+} doped alumina was in the range 2.1–2.2 MPa.$m^{0.5}$. Therefore, Er^{3+} doped Al_2O_3 is a suitable combination of superior optical and mechanical properties [75].

It is concluded that transparent Al_2O_3 ceramics' optical and mechanical qualities rely on grain size and residual porosity. Various methods have been used to manage grain size and porosity. The mechanical strength and optical transparency of transparent Al_2O_3 ceramics were significantly improved with a decrease in grain size of TC. Al_2O_3 exhibits a Vickers micro-hardness of HV10 GPa to HV 27 GPa (at 10 kgf load). When the grain size of sintered alumina is reduced to the submicron range, a considerable improvement in hardness is produced. The fine grain size is accompanied by a high relative density and a low frequency of defects. Dopants like Mg, Y, La, ZrO_2, and MgO significantly improved the mechanical properties of the TC by altering the microstructure. Er atoms on the grain boundary causes a reduction of grain boundaries mobility, which led to decreasing the mean grain size. The wear resistance of transparent Al_2O_3 increases by strengthening grain boundaries, providing micro-mechanical stability. During scratch test, crushing, cracking, and delamination of the TC occurs. Self-doped Al_2O_3 transparent ceramic prepared using SPS technique provided higher transparency than pure Al_2O_3. Such high transmittance is only possible with SPS and needs high sintering pressures and low sintering temperatures. The Vickers hardness of the Er^{3+} doped alumina was one of the hardest (26.9 GPa at 10 N load) materials in this category.

2.3 AlON

Yamaguchi and Yanagida discovered aluminium oxynitride (AlON), a spinel structure in the pseudo binary Al_2O_3-AlN system [168]. Based on tests and theoretical calculations, the most acceptable model is McCauley's constant anion structural model with the formula $Al_{(64+x)/3}V_{(8-x)/3}O_{32-x}N_x$ (where V refers to cation vacancies and $2 \leq x \leq 5$) [24]. McCauley was the first to use reactive sintering to create translucent AlON ceramics using Al_2O_3 and AlN as raw materials[68]. Ish-Shalam [169] then adopted a carbothermal reduction and nitridation process to synthesize

AlON powder, which was then used to make translucent AlON ceramics. Raytheon [27] developed and commercialised large-scale transparent ceramics with exceptional optical quality over several decades. The transmission range of AlON extend from 0.2 µm in the UV through the visible to 6.0 µm in the infrared, which makes it a very useful material for many optical applications [168].The high strength and high hardness make AlON an ideal material for transparent armor products [170]. Transparent AlON exhibit superior slow crack resistance relative to fused silica [22] and has a potential in spacecraft window systems [77]. Transparent windows of AlON are produced in various sizes ranging from 8 to 24 inches and even greater. AlON has similar mechanical and thermal properties to that of polycrystalline alumina. Because of superior mechanical, tribological, and optical properties Raytheon Company (now Surmet) has used AlON for IR domes for missiles for many years. Compared to Al_2O_3, AlON has the advantage of cubic crystal structure and thus of optical isotropy.

Among the various types of processes to manufacture transparent AlON, the typical method of pressing has been widely employed due to its simplicity, time-saving, and low cost [171]. The manufacture of highly transparent aluminium oxynitride (AlON) ceramics in a variety of sizes and forms was accomplished using non-aqueous tape-casting forming method [123]. The tape-casting process employs both warm and cold isostatic pressing, which improves the microstructure and density of the AlON green tapes. This technique was used to obtain transparent AlON ceramics with pressureless sintering at temperature of 1800^{o}C for 8 hours [123,160]. The finished product has a transmittance of 84 % at wavelength of 2000 nm. AlON has hardness and fracture toughness value of around 18 GPa and 1.4 MPa.m$^{0.5}$, respectively. The improvement in these mechanical properties result in good wear resistance resulting enhanced tribological properties. The microstructure of AlON is shown in **Fig. 8a**.

Bodhak et al. [28] studied in vitro tribological properties of transparent AlON ceramics for implant applications. Tribometric tests with 3 mm Al_2O_3 ball performed in a simulated body fluid at 37 °C provided wear rate of the order of 10^{-6} mm^3 Nm^{-1}, much lower compared to Al_2O_3 on Al_2O_3 or ZrO_2 on ZrO_2 reported in other publications [89,172,173]. A linear-reciprocating ball on a disc testing tribometer was used for all the experiments. A linear oscillatory motion of 10mm was made with a constant load of 20N and a constant speed of 5000 mm/min with Al_2O_3 as a counter body. Wear rate for distances of 1000 m and 3000 m was 12.5±2.16 x 10^{-6} mm^3 Nm^{-1} and 10.1±0.27 x 10^{-6} mm^3 Nm^{-1}, respectively. Volume loss for similar distances was estimated to be 0.250±0.01 mm^3 and 0.606±0.03 mm^3, respectively. Hardness and friction coefficient value of fabricated $MgAl_2O_4$ sample was 15.14±0.46 GPa and 0.46±0.02.

The tribological behaviour of AlON depends on the sintering additives. Zhao et al. [174] added nano-sized silicon carbide (SiC) and zirconia (ZrO_2) particles to AlON produced by hot-press sintering, which significantly increased the mechanical characteristics (relative density, microhardness, Young's modulus, flexural strength and fracture toughness) than AlON fabricated without additive. Zirconium nitride (ZrN) phase was observed to have formed as a result of the addition of nanoparticles during sintering. The majority of the SiC and ZrN nanoparticles were positioned at the grain boundaries of micro-scale AlON particles and limited the expansion of AlON grains owing to the pinning action of SiC and ZrN nanoparticles, as shown in **Fig. 8b**. It causes the reduction in the grain size in nanoparticulate reinforced composites. The reinforcement and grain size reduction can reduce the crack propagation and the wear of the TC.

Liu et al. [175] fabricated transparent MgAlON ceramic with the composition $Mg_{0.27}Al_{2.58}O_{3.73}N_{0.27}$ exhibiting a maximum transmittance of 84% by pressureless sintering of fine single-phase powders. The sintered sample exhibits excellent in-line transmittance, which is due to the high density and the rare pores coupled with a high purity, as shown in **Fig. 8c**. Transparent MgAlON ceramic exhibits a broad transparency range from 0.22 to 6.24 µm, excellent mechanical properties, dielectric constant of 9.19 MHz at 1 MHz, and thermal conductivity of 8.16 $Wm^{-1}K^{-1}$ at 32°C. The hardness of MgAlON (13±0.18 GPa) was found higher than $MgAl_2O_4$ (12-15 GPa) but lower than γ-AlON (~15 GPa). The fracture toughness of MgAlON (2.46±0.30 $MPa.m^{0.5}$) was higher than $MgAl_2O_4$ (1.5-2.2 $MPa.m^{0.5}$) and similar to γ-AlON (~2 $MPa.m^{0.5}$) [160,175]. The physical properties of AlON seems to be influenced by the simultaneous introduction of Mg in cation sites and N in anion sites. Ma et al. [176] synthesized MgAlON powder at 1600 °C for 2 h via the carbothermal reduction and nitridation method. The obtained MgAlON powder is crystalline and exhibits a spinel structure. It shows high sinterability, with a bimodal particle size distribution at 0.3 µm and 0.9 µm. The microstructural sintering evolution showed that significant densification occurs at the temperature range of 1600–1700 °C, and rapid grain growth appeared at higher temperature (≥ 1750 °C). Pressureless sintering with additional holds at the intermediate temperature regions (1650–1700 °C) was effective in controlling the microstructure with reduced porosity, which in turn improved the light transmittance. Three samples were prepared at different sintering temperature, shown in **Fig. 8d, Fig 8e, and Fig 8f**. A highly transparent MgAlON ceramic was prepared by pressureless sintering at 1700 °C for 2 h and then at 1850 °C for 20 h, which exhibits excellent transmittance from the visible to middle IR regions (82.37 % at 0.60 µm and 86.59 % at 3.70 µm). The Vickers hardness and flexural strength are ~ 13.5 GPa and ~ 246 MPa, respectively.

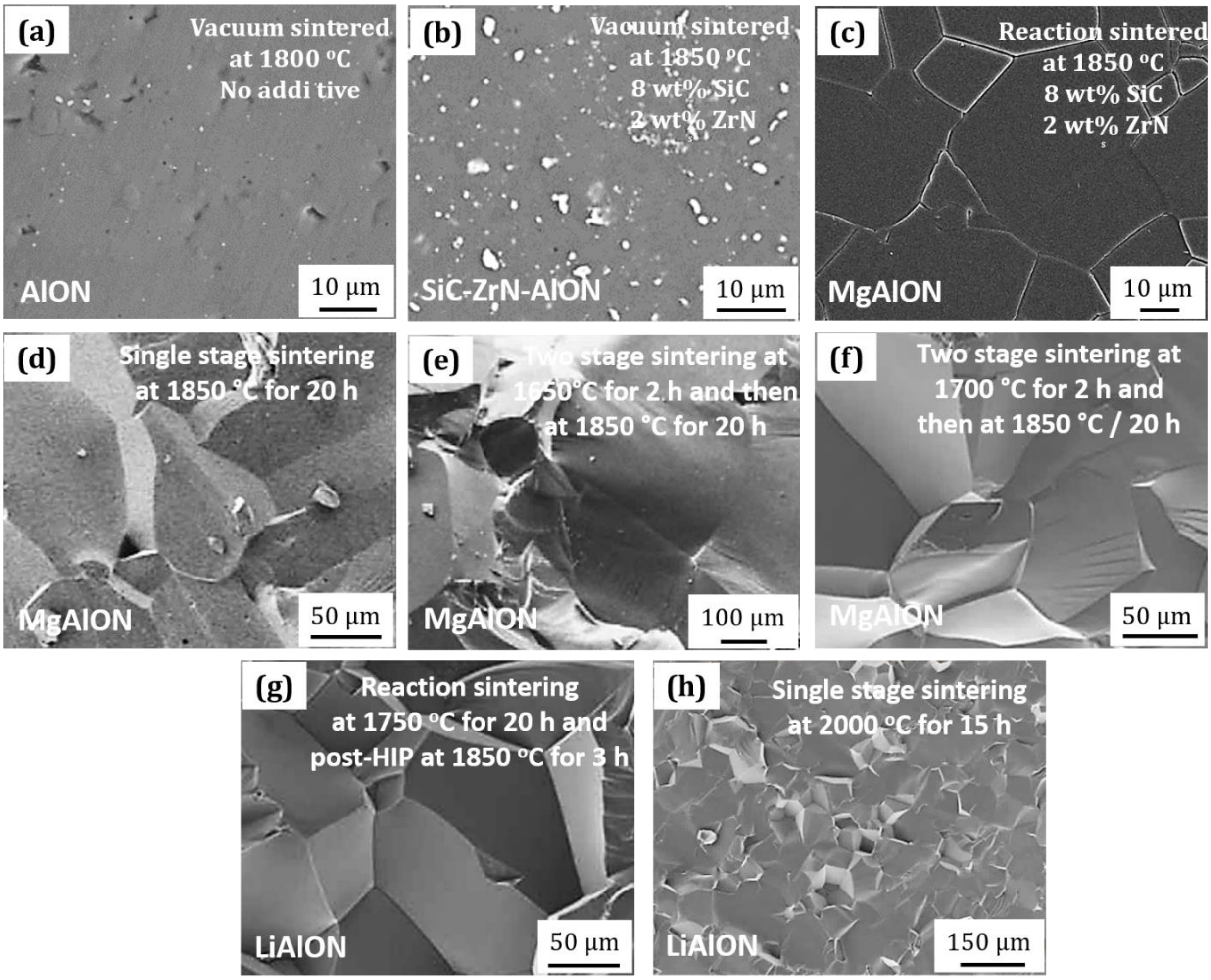

Fig. 8: Microstructure of a) pure AlON [174] b) SiC-ZrN-AlON composite [174] c), d), e) MgAlON [175,176], f), and g) LiAlON [177,178]

Highly transparent LiAlON ceramic was successfully manufactured by Zhang et al. [177] via reaction sintering (1750 °C, 20 hours) of AlN-Al_2O_3-$LiAl_5O_8$ composite and post-HIP (1850 °C, 3 hours, 180 MPa). Al_2O_3 acts as secondary phase in LiAlON. Transparency of 85.5% at 3.7 µm wavelength was achieved thanks to a complete pore removal (Figure 8g). LiAlON has a potential of high wear resistance, as it exhibits high flexural strength and Vickers hardness (303 MPa and 15.06 GPa, respectively). Clay et al. [178] also fabricated transparent LiAlON by pressureless reaction sintering at sintering temperature 1800 ^{o}C and HIPing at 2000 ^{o}C at 207 MPa for 2 hours (Figure 8h). In addition, they also show that transparent LiAlON is obtained by pressureless sintering, without HIPing, if annealed at 2000 ^{o}C for 10-15 hours. The hardness of LiAlON obtained with the two processes was 17 GPa with 1 kg load Vickers indent. High optical transmittance and good mechanical properties of LiAlON, along with its comparatively low processing temperature, make it a viable material to compete with MgAlON and AlON. Table 3 shows different mechanical and optical properties of transparent AlON.

Table 3: Mechanical and optical properties of different AlON-based ceramics.

Material	**Vickers hardness (GPa)**	**Flexural Strength (MPa)**	**Grain size (µm)**	**Transparency**
AlON [179–181]	17	-	-	~80% (at 2.5 to 4 µm)
AlON [174]	13.78±0.21	296±63	~5	-
AlON [28,160]	~15	~310	~200	~80% (2.5-4 µm)
LiAlON [177]	15.06±0.20	303±8	~120	~85.5 % (at 3.7 µm)
LiAlON [178]	16.50±0.50	-	~80-100	~65 % (at 3.3 µm)
MgAlON [176]	13.50±0.15	246±5	100-150	~86.59 (at 3.7 µm)
MgAlON [175]	13.39±0.18	274±5	57.5	~82% (at 0.5 to 4 µm)
SiC-ZrN-AlON [174]	18.19±0.30	418±52	< 5	-

It is concluded that the presence of second phase reinforcements and a fine grain size reduce the crack propagation and the wear of the TC. Sintered specimens with porosity below 0.5-1.2% have low wear resistance and provide good tribological behaviour. This is achieved with the addition of sintering additives at low sintering temperature and high pressure. On the other hand, secondary phases reduce transparency due to scattering.

2.4 Lu_2O_3

In recent years, some researchers have validated a strong interest in the production of Lu_2O_3 TCs of high quality and large size [78,79], and their characterization [182,183], including the tribological characteristics [184]. For characterisation of tribological and mechanical properties, scratch testing is used to provide the understanding of the surface deformation characteristic and material removal mechanism of hard-brittle materials. Single nanoscratch, repeated nanoscratch, and double nanoscratch experiments of Lu_2O_3 TCs (diameter of 6 mm and a thickness of 1 mm) have been carried out on a nanoindenter [184] using Berkovich indenter's tip radius of about 80 nm. Chemical-mechanical polishing was used to polish the workpiece surface and the polished surface has a roughness of less than 3 nm as determined by atomic force microscopy (AFM). Prediction values for penetration depth in single and repeated nanoscratch tests are very close to experiment observations, as shown in **Fig. 9a**.

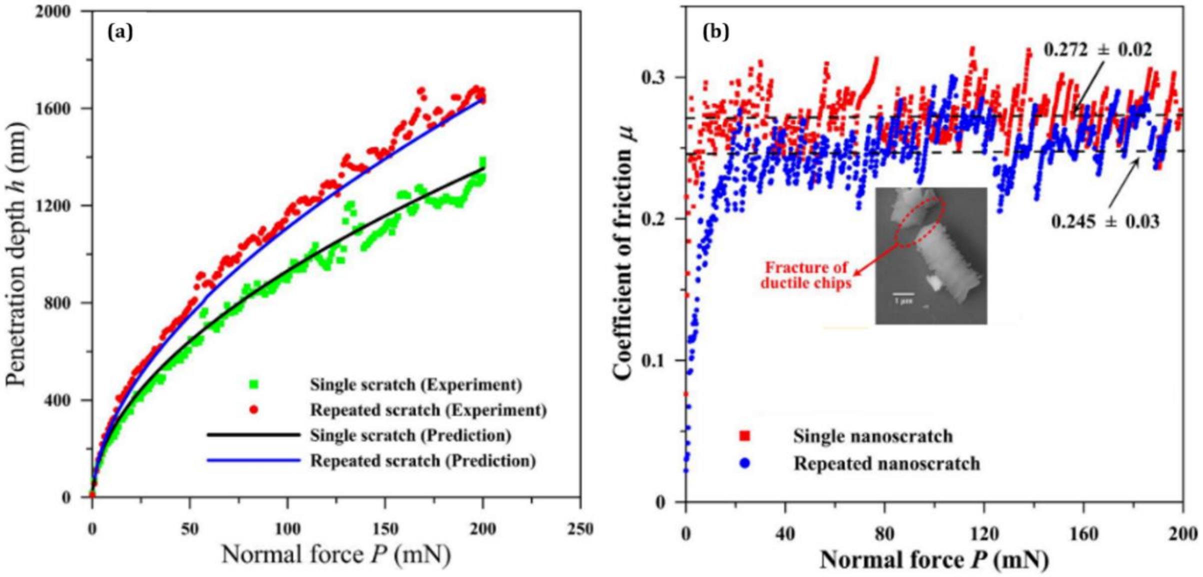

Fig. 9: Relationship of a) penetration depth vs. normal force and b) coefficient of friction vs. normal force in single nanoscratch and repeated nanoscratch tests on Lu_2O_3 TCs [184].

The coefficient of friction is generally calculated using normal force and tangential force. The relationships between the friction coefficient and normal force in single nanoscratch and repeated nanoscratch tests are shown in **Fig. 9b**. The grain boundary, chip fracture, and plastic flow lines all contribute to the variation of the friction coefficient during the nanoscratch process. In repeated nanoscratch tests, the friction coefficient is lower than in single nanoscratch tests. This is due to the reason that subsurface damage caused by the first nanoscratch modifying the mechanical characteristics of the material which in turn modify the tribological characteristics. After the first scratch, the remaining material transforms into a mixture of polycrystalline nanocrystals and amorphous material, compared to the original micron-size grains. Simultaneously, many defects, including dislocations, stacking faults, nano twins, atomic plane torsion, atomic plane fracture, and atomic plane misalignment, are generated in nanograins during the nanoscratch process. The mechanical properties of a mixture of polycrystalline and amorphous material compared with many atomic-scale flaws are different from micron-sized grains. These changes in mechanical properties result in a reduction in the friction coefficient with repeated scratching. The friction coefficient increases and then tends to be stable with the increase of the normal force.

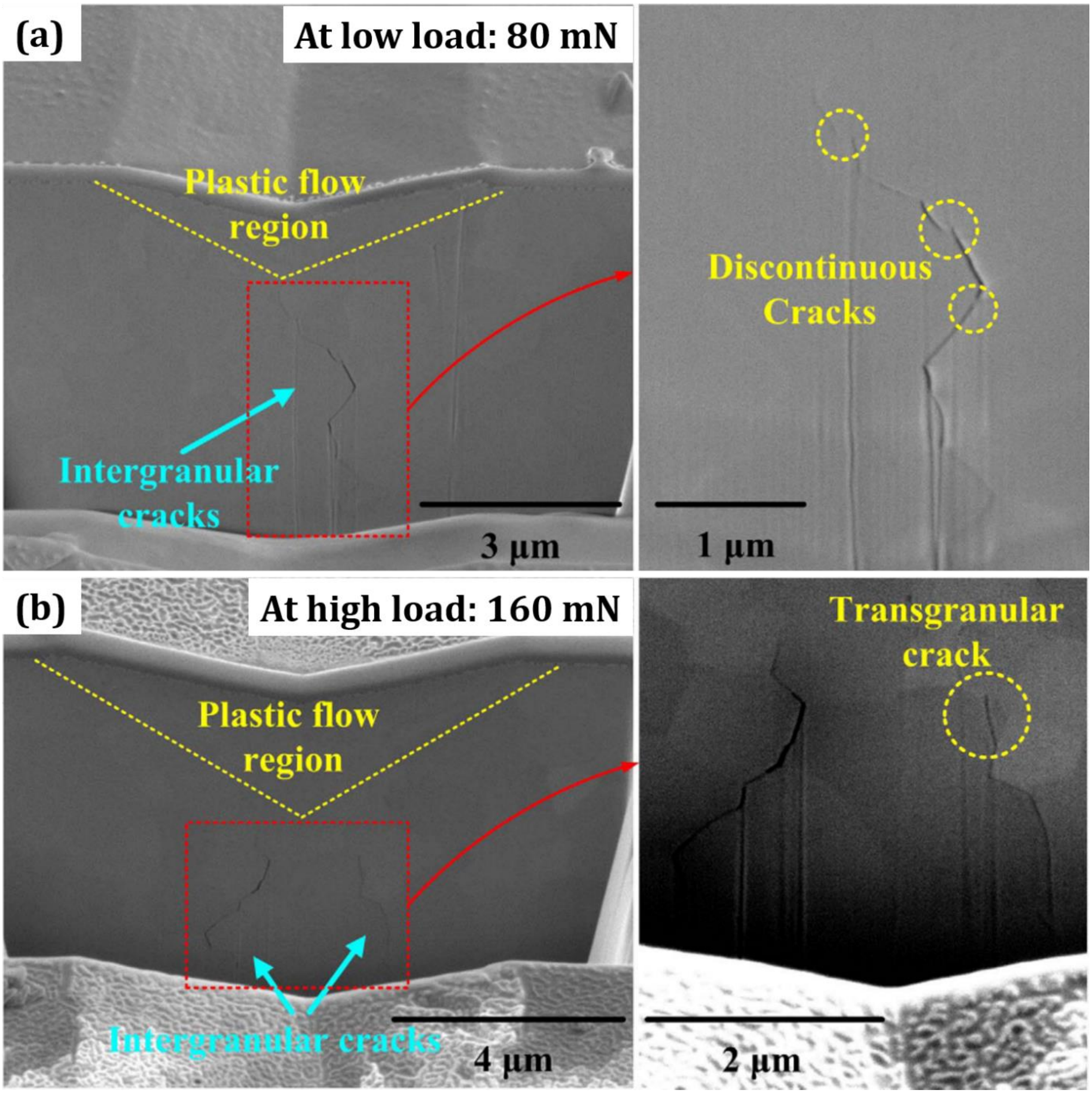

Fig. 10: Crack propagation in transparent Lu_2O_3 under a) low load and b) high load conditions [184].

The tribological behaviour of TCs depends on the load applied during wear. In a scratch test of transparent Lu_2O_3 [184] cracks were not formed under low load conditions, i.e., below 5 mN load. At higher load conditions, median cracks were formed at a deeper depth than the depth of the scratch indenter. It was observed that intergranular fracture was the most common mode of crack propagation (**Fig. 10a**). Additionally, the subsurface has a modest number of transgranular and discontinuous fractures (**Fig. 10a and Fig. 10b**). Discontinuous cracks at low load (**Fig. 10a**) are converted to transgranular load at high load (**Fig. 10b**). In TCs, grain boundaries are especially weak and the mismatch degree between neighbouring grains is high [185]. As a result, subsurface fractures spread along grain boundaries in TCs. Lu_2O_3 powder was used for fabricating TC by SPS technique [186]. The pressure and temperature of SPS varied between 20-100 MPa and 1000^{o}C-1600^{o}C, respectively, with soaking time of 5-600 minutes. The microstructures were uniform, with homogeneous equiaxed polyhedral grains, and had few residual pores at the triple junctions. The concentration of pores dropped as the sintering temperature increased from 1300^{o}C to 1500^{o}C and then rose again above 1500^{o}C accompanied by abnormal grain growth. The fracture surface of the TC was intergranular below 1500^{o}C and transgranular above. **Fig. 11a, Fig. 11b, and Fig. 11c** show that an increase in sintering temperature leads to the increase in grain size of the TC, which results in a loss of transparency after attaining the maximum value. The increase in grain size reduces the hardness and fracture toughness value. It, in turn, increases the mass loss tendency upon wear test. **Fig. 11d and Fig. 11e** show the increase in the grain size of the material when Lu_2O_3 is doped with additives. Ytterbium (Yb) doped Lu_2O_3 TCs fabricated using SPS sintering technique have a smaller grain size than TC fabricated using vacuum sintering (**Fig. 11d and Fig. 11e**) [187]. **Fig. 12** shows the decrease in transparency with the rise in relative density and grain size. The small-sized grain TC is likely to perform well in the tribological application for which an optimum sintering temperature is required [186,187].

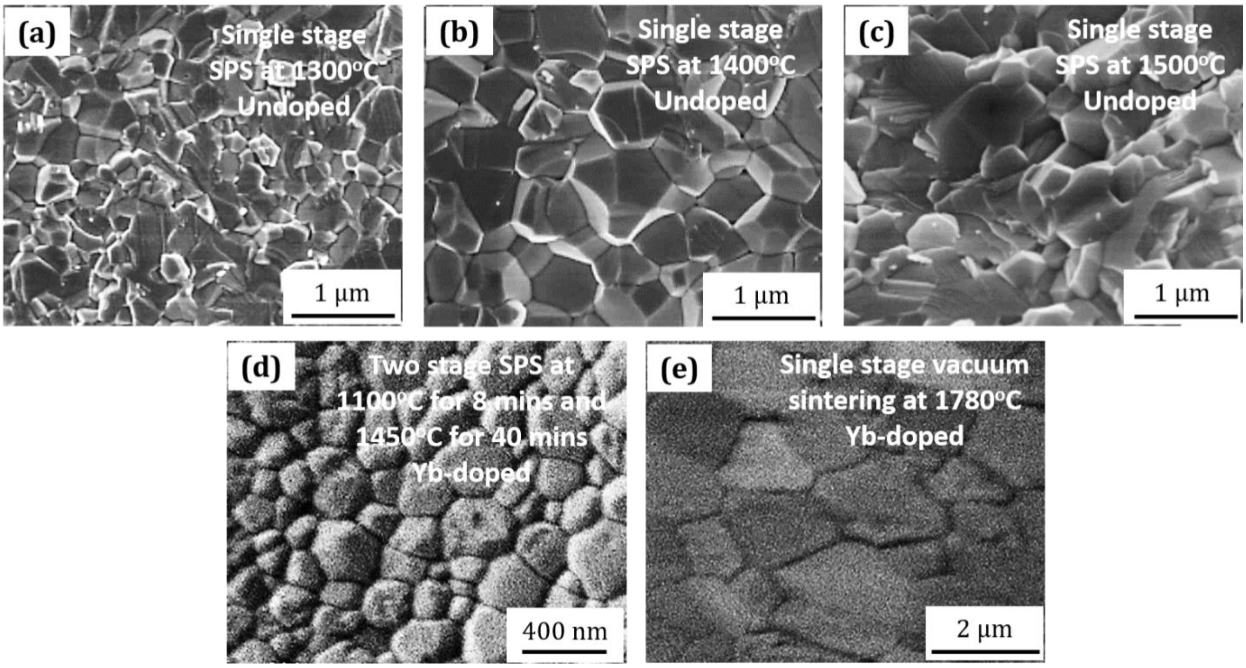

Fig. 11: Microstructure of a), b), c) undoped Lu_2O_3 sintered by single stage SPS, d) Yb-doped two stage SPS, and e) Yb-doped two stage vacuum sintering [186,187].

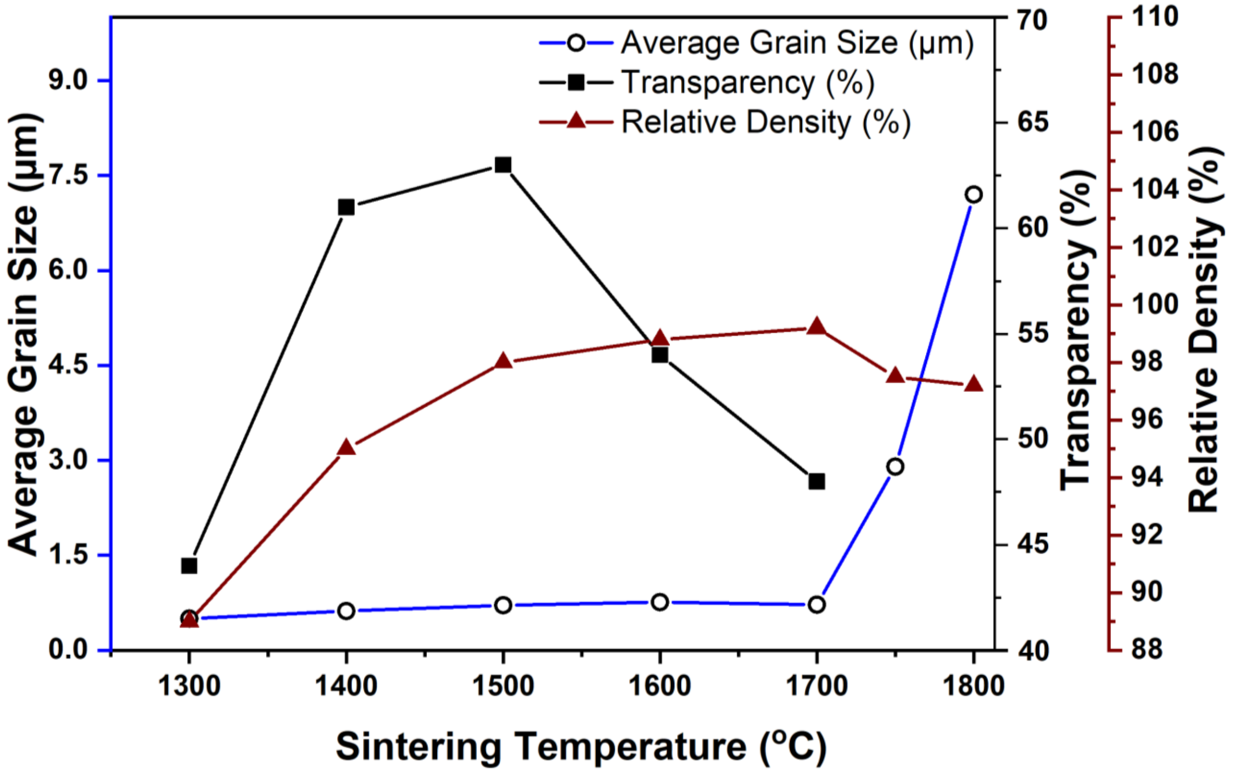

Fig. 12: Variation of average grain size (µm), transparency (%), and relative density (%) of transparent Lu_2O_3 without additive as a function of the sintering temperature by SPS [186,187].

It is concluded from the above discussion that the grain boundary, chip fracture, and plastic flow lines all contribute to the disparity of the wear behaviour during scratching. The wear of TC is a function of porosity. The porosity of the fabricated TC depends on many factors. One out of these factors is sintering temperature. The optimum sintering temperature is desirable for achieving low porosity.

2.5 Y_2O_3

Transparent polycrystalline Y_2O_3 has significant physical and chemical properties, such as low thermal expansion (8.1×10^{-6} K^{-1}) [188], the refractive index of 1.935 [189], high density (5.031 g/cm^3) [81], high thermal conductivity (13.6 W/m.K at 300 K) [188], a broad transparency range from violet to infrared light (0.2 to 8 µm), and high corrosion resistance. Consequently, Y_2O_3 ceramics are used as promising TCs in various applications, including high-intensity discharge lamps, infrared missile domes, gas nozzles, and heat-resistive windows [81,82]. Liu et al. [113] fabricated high-strength transparent Y_2O_3 ceramics using the SPS technique by optimizing the heating rate. The heating rate substantially affects the microstructure of transparent Y_2O_3, which affects the optical/mechanical characteristics of TCs due to reduced grain growth with the rise in heating rate. SPS has effectively synthesized dense Y_2O_3 materials at lower sintering temperatures, 1100-1300°C and shorter sintering times [94,190,191]. As in the case of Lu_2O_3, the final microstructure depends strongly on the sintering process used, and SPS offers a faster treatment at a lower temperature in comparison with vacuum sintering [192], leading thus to a finer grain size.

Numerous articles have been published on the production of transparent Y_2O_3 ceramics using pressureless sintering in vacuum or in an H_2 environment [193–196]. Densification was facilitated with decreased particle size of the powder. Jin et al. [194] reported on a vacuum sintering technique for fabricating transparent Y_2O_3 ceramics using ZrO_2 doping, with varying ZrO_2 concentrations after 8 hours of sintering at 1860°C. The starting Y_2O_3 powder had an average particle size of 2 mm, which was decreased to approximately 0.34 mm after 12 hours of ball milling in ethanol. The optimal concentration of ZrO_2 was found to be 5 mol% in terms of densification and reduced grain size. The good tribological properties of Y_2O_3 ceramics is explained by their improved densification and inhibited grain development characteristics caused by the presence of ZrO_2. **Fig. 13a-Fig. 13d** shows SEM images of samples sintered at 1860°C for 8 h. No pore was seen in the sample doped with 5 mol% ZrO_2. This reduction in porosity will provide better wear resisting properties to the TC. To increase the density of TCs with high transmittance, transparent Y_2O_3 ceramics are also fabricated using vacuum and air sintering in combined with HIPing [197]. The results show that sintering in air in combination with HIPing is similar to sintering in vacuum and HIPing for the preparation of transparent Y_2O_3 ceramics. The density of the resulting air-sintered ceramics is limited to about 98–99%. HIPing is required to take the ceramics to full density. Nanophase Y_2O_3 powder is simply processed into green bodies with high densities. **Fig. 13e** represents SEM image of sintered and etched transparent Y_2O_3. The nanophase Y_2O_3 powder was dry-pressed in a stainless steel die under 632 MPa for 30 minutes to prepare 2 mm thick green body. The green body was then sintered at 1600°C for 2 hours in air. The resulting translucent ceramic of relative density of about 99.4% was polished to gain 61% transparent Y_2O_3.

Recently, nanocrystalline Y_2O_3 ceramics were prepared [57] with very fine grains (20 nm) and good mechanical properties (hardness 10.5 GPa, fracture toughness 2.21 Mpa $m^{1/2}$), although the production method required very high pressure (5 Gpa). Y_2O_3-MgO nanocomposites transparent in the near-infrared light have been also produced using hot pressing [198,199] and SPS [132]. The production of transparent nanocomposites is a particularly interesting concept, as while the combination of phases with different refractive index generally does not allow reaching transparency, the scattering is limited when the grain size is significantly reduced below the wavelength of light. At the same time, such approach offers a lot of space for the tuning of effective material properties. Furthermore, Y_2O_3 nanopowder was also used a starting material to produce transparent Y_2O_3 ceramic by SPS at 1200 ^{o}C to 1600°C for 20 minutes under the pressure of 100 Mpa [200]. It was observed that an optimum sintering temperature is required for obtaining good mechanical properties while maintaining good transmittance value.

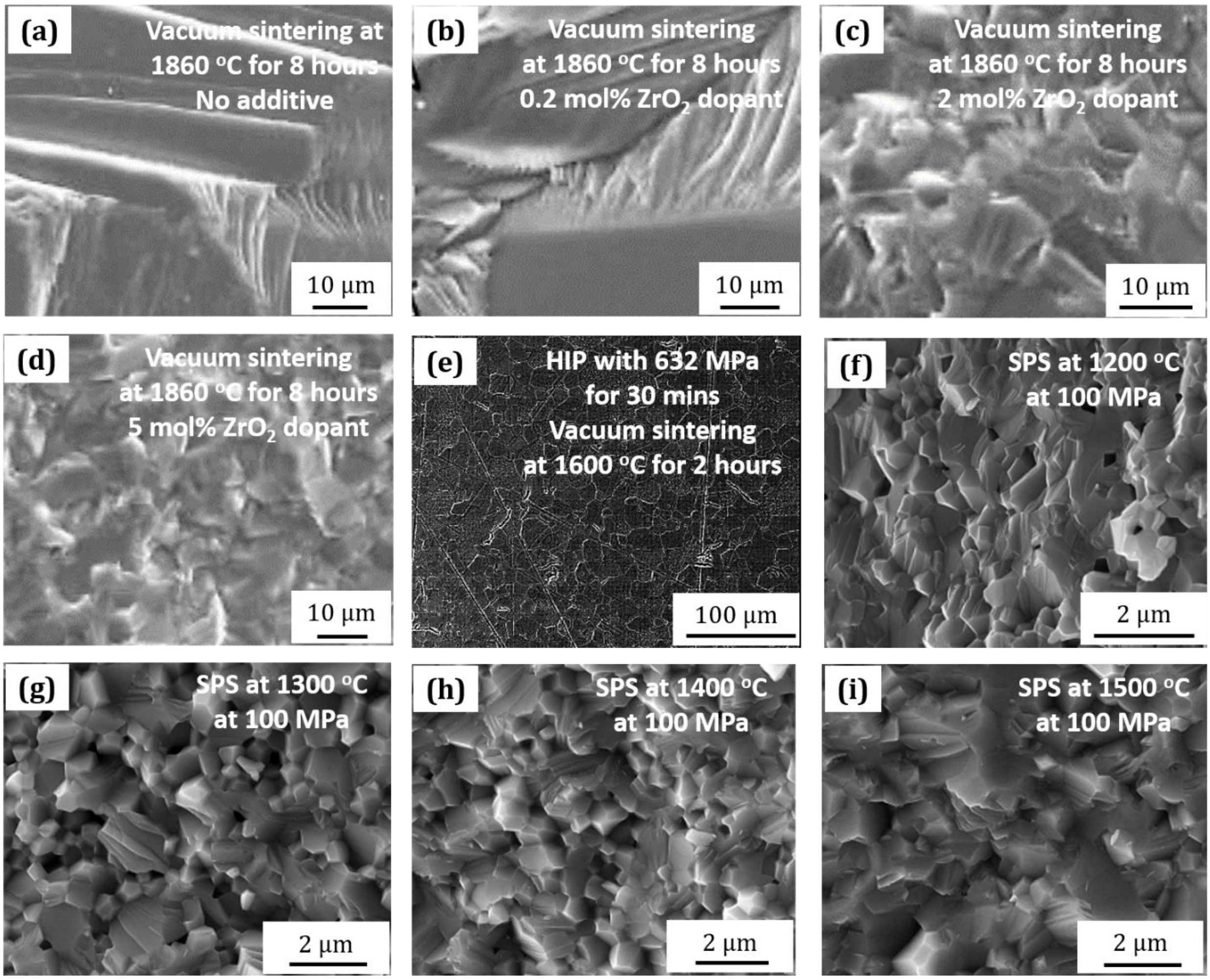

Fig. 13: Micrographs of transparent Y_2O_3 obtained a) via vacuum sintering without additive [194] b), c), d) via vacuum sintering with 0.2 mol%, 2 mol% and 5 mol% ZrO_2 dopant [194] e) via HIP followed by vacuum sintering [197], f), g), h) and i) via SPS at different temperatures [200].

Table 4: Mechanical and optical properties of different Y_2O_3 TCs.

Material	**Vickers hardness (GPa)**	**Fracture Toughness ($MPa.m^{0.5}$)**	**Grain size (µm)**	**Transparency (%)**
Y_2O_3 [197]	7.41-7.67	-	21.5±11.1	61 at 1000 nm
Y_2O_3 [200]	6.87-7.60	1.99-2.06	0.58±0.11	54 at 800 nm
Y_2O_3 [57]	10.4-10.5	2.20-2.21	~0.02	81.3 at 1100 nm
Er:Y_2O_3 [201]	7.23 ±0.35	0.81 ±0.07	~328	32 at 2000 nm
Er:Y_2O_3 [201]	9.09 ±0.41	1.39 ±0.07	~0.34	81 % at 2000 nm

The micrographs of fracture surface of sintered samples obtained at different temperatures are shown in **Fig. 13f-13i**. The hardness of the TC increased from 6.87 to 7.60 GPa and flexural strength increased from 75 MPa to 122 MPa with increase in the sintering temperature up to 1500°C due to relative density improvement and decreased with further rise in temperature. However, the fracture toughness did not show the same trend and decreased with rise in the temperature due to the reduction in the porosity. The change in mechanical properties of the TC improve the tribological properties and need to be further investigated. **Table 4** collects the mechanical and optical properties of different transparent Y_2O_3 ceramics available in the open literature. The hardness of transparent Y_2O_3 increases with increasing heating rate and follows the Hall–Petch relationship, i.e., with grain size reduction [113]. On the other hand, the toughness is less susceptible to heating and grain size and takes on a comparable value. Therefore, the influence of heating rate on wear resistance and coefficient of friction of material requires further research.

However, it should also be kept in mind that the fracture toughness of transparent Y_2O_3 is relatively low compared to other transparent ceramics, affecting the tribological behavior. Most research has been done on TC's densification and microstructure. There is no systematic research on the correlation between the change in the microstructure of transparent Y_2O_3 and the mechanical characteristics, which improves the wear resistance of materials.

2.6 Cubic boron nitride (cBN)

In comparison to cubic boron nitride (cBN) single crystals, polycrystalline cBN (PcBN) sintered bodies have better mechanical and tribological characteristics. PcBN was subjected to high pressure (20 GPa) and temperature (1500 °C), resulting in nanostructures with a grain size of 20 nm and hardness of 85 GPa. The Hall Petch effect, in which the mobility of dislocations is effectively inhibited, is responsible for the increase in hardness of nanostructured PcBN to about 50-70% [202]. As a consequence of the high hardness value, there is a high wear resistance associated with it. A high wear resistance is expected considering the high hardness. Tian [109] first incorporated nano twins into nanostructured PcBN, which led to an increase in hardness to 100 GPa. Grains were equiaxed of the same size but irregular in shape. However, there is still debate regarding this outcome [203]. Conversely, the above-mentioned manufactured superhard PcBN exhibits transparent properties with a maximum transmittance ranging from 20% to 40% at 400–800 nm [110].

Taniguchi et al. [80] developed bulk single-crystal cBN that was colorless and had worthy transmission by utilizing $Ba_3B_2N_4$ as solvents. Researchers [108–110] used hexagonal BN (hBN) as a starting material for the production of superhard cBN blocks without any further additives or modifications. The fabrication requires very high sintering pressure and temperature, which modifies the phase from hBN to cBN, leading to optical transparency. For manufacturing transparent ultra-hard polycrystalline cBN with a grain size of 200 nm, a two-stage multi-anvil cell pressing was utilized in conjunction with pressures as high as 14 GPa and temperatures ranging from 1300–2000^{o}C. Translucent polycrystalline cBN was obtained with a maximum hardness of about 69 GPa, which is almost two times harder than single-crystal [204]. cBN powders of different sizes were sintered at pressure 7.7 GPa and temperatures varying from 1500 to 2500^{o}C [205]. It was observed that the transparency of the materials decreases if the powders is sintered between 2000 to 2500^{o}C. The fracture mechanism for transparent cBN changed from intergranular to transgranular when the sintering temperature was increased during the fabrication of TC. The performance of the materials changed also with the initial particle size. The performance of the materials changed also with the initial particle size.

Fig. 14a, Fig. 14b, and Fig. 14c represent the variation of relative density, hardness, and fracture toughness as a function of the sintering temperature of transparent cBN with an initial particle size of 0.5-1.2, 2-4, and 8-12 µm, respectively. It depicts that with an increase in sintering temperature, the relative density increases. The value of hardness and fracture toughness of the TC first increased with an increase in particle size from 0.5-1.2 to 2-4 µm, and then decreased with a further increase in particle size from 2-4 to 8-12 µm. So, the optimum size of initial particle size is between 1-2 µm for maximum hardness and fracture toughness. Hence, the particle size affects the tribological behavior of TC as wear resistance of the sintered sample possibly increases with the increase in hardness and fracture toughness. The maximum hardness value was obtained at sintering temperature around 2350^{o}C for all initial particle sizes. However, the maximum fracture toughness was received for 0.5-1.2 µm, 2-4 µm, and 8-12 µm at around 2200°C, 2000°C, and 2400°C, respectively.

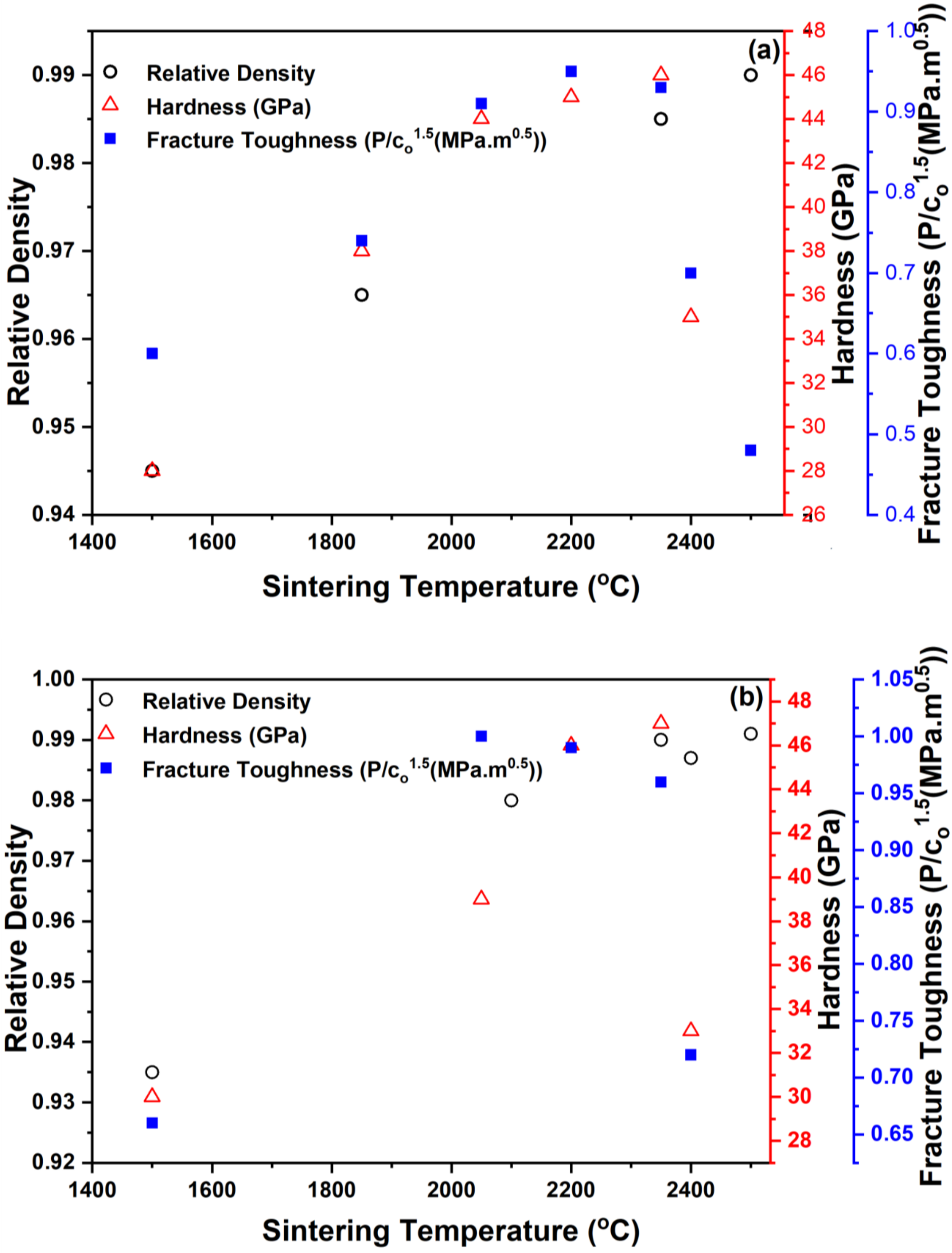

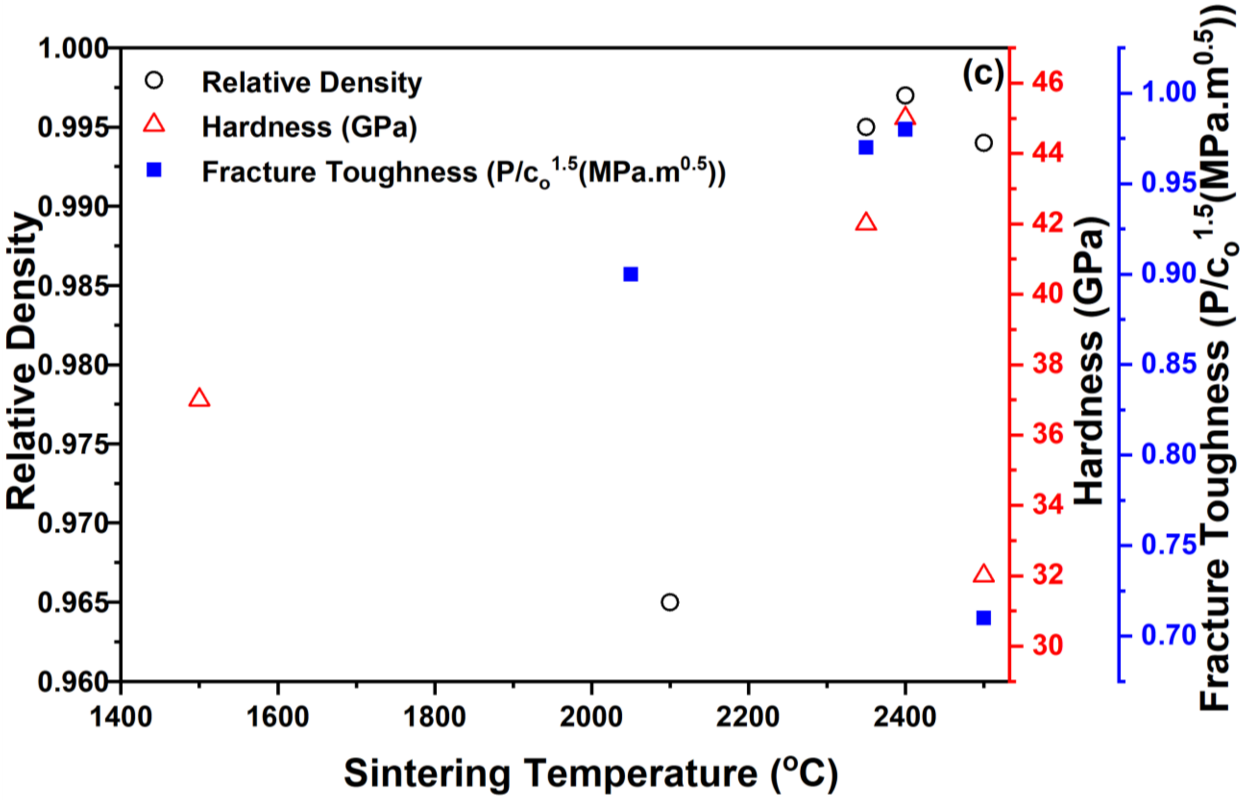

Fig. 14: Relative density, hardness, and fracture toughness vs. sintering temperature of cBN with initial particle size a) 0.5-1.2 µm b) 2-4 µm, and c) 8-12 µm [205]

Wear resistance is an essential characteristic for the use of sintered transparent cBN. To understand the wear behaviour of cBN, the machine tool made of cBN synthesized by reaction sintering were compared to other sintered tools made by vacuum sintering method. The degree of wear in the cutting edge of the manufactured cutting tools is represented by the flank wear. The relation between the amount of flank wear and the cutting time of the test specimens made of different initial particle size and the relationship between the amount of flank wear and the cutting time of the sample produced by reaction sintering were derived. Four specimen at different sintering conditions were fabricated, i.e., specimen of initial particle size of 0.5–2 µm and 2–4 µm: sintered at 2050°C and 7.7 GPa, specimen of initial particle size of 4–8 µm: sintered at 2350°C and 7.7 GPa, and specimen obtained by reaction sintering method: synthesized at 7.7 GPa and 2150°C. Machining conditions were cutting speed of 10 m/min, depth of cut 0.2 mm, and feed/rev of 0.1 mm/rev with no coolant on work material WC-24 wt.% Co alloy. According to the research findings, there was no noticeable difference between any test specimens in terms of wear characteristics. There was a significant overlap between the wear resistance of test specimens and that produced by the reaction-sintering technique. According to Hooper and Brookes [206], the high value of hardness is associated with the higher fraction of cBN aggregate material. It is due to the deformed cBN skeletal structure produced during the synthesis process. SEM and TEM studies of the grain and microstructure of transparent polycrystalline cBN have shown that both the Hall–Petch effect and microscopic flaws contribute to the enhanced hardness and wear resistance of the TC.

It is concluded that an optimal size of initial particle is required to develop TC with the hardness and fracture toughness needed for tribological application. The production of equiaxed grains resist the mobility of dislocations which is desired for high wear resisting TCs.

2.7 SiAlON and Si_3N_4

SiAlON ceramics are solid solutions of silicon nitride (Si_3N_4) containing variable amounts of additional aluminum (Al) and oxygen (O). High strength over extensive high temperatures, high thermal shock resistance, and relatively high chemical stability of SiAlON ceramics place them amonst other important engineering ceramics. Advanced sintering technologies have been used to fabricate translucent and even transparent SiAlON ceramics, demonstrating their potential as engineering ceramics [101,207]. SiAlON is structurally identical to Si_3N_4, except that Al and O, respectively, have replaced the Si and N of Si_3N_4. Sintering of Si_3N_4 powder with AlN-Al_2O_3-MO_x and AlN-MO_x systems, where M denotes Li, Mg, Ca, Y, and rare earth elements, is produce SiAlON ceramics (excluding La, Ce, Pr, and Eu) which are transparent and suitable for tribological applications. The translucent α-SiAlON ceramics stabilized with metal cations, such as Nd^{3+}, Y^{3+}, Gd^{3+}, Dy^{3+}, Yb^{3+}, Lu^{3+}, etc. have been developed with high transmittance in the infrared region [84–86].

Silicon Nitride (Si_3N_4) is an extensively used ceramic material with numerous industrial applications. Atoms of silicon and nitrogen of Si_3N_4 have strong covalent bonds and hence, it exhibits poor atomic mobility and high resistance to deformation. Usually, two polymorphs of Si_3N_4 (α and β), having silicon atoms tetrahedrally coordinated by nitrogen atoms, exist at wide temperature range: a low-temperature α-Si_3N_4 whereas and high-temperature β-Si_3N_4. A third polymorph (γ-Si_3N_4) was obtained at high pressure (∼13 GPa). It has a cubic structure with two-thirds of silicon atoms octahedrally placed and one-third of silicon atoms tetragonally placed. It has a very high density and closer atomic packing and good transparency in the visible range. However, so far the production of larger bodies was not demonstrated Si_3N_4 is one of the most successful ceramic materials for spacecraft applications [208,209] because of its mechanical strength and good wear resistance in harsh environments that include constant rain and extreme thermal shock [210,211]. In addition, the bending strength and hardness of 100 % dense pure Si_3N_4 developed without additives are almost temperature independent from room temperature to 1500 °C [212]. It makes Si_3N_4 an appealing material for high-temperature tribological applications [213]. Si_3N_4 exhibits properties such as high flexural strength, good wear resistance, corrosive resistance, fracture resistance, creep resistance, and high hardness. The optical properties of Si_3N_4 are of enormous interest over decades [214]. Si_3N_4 is transparent in the IR range, but the transparency in the visible range is usually limited. Many researchers have developed transparent Si_3N_4 by different techniques with appreciable transparency and improved mechanical and tribological properties. Some researchers have recently shown an interest in preparing translucent ceramics [86,215–219]. Pechenik et al. [220] used a laser-driven gas-phase reaction between silane and ammonia, followed by diamond cell pressing at 100 GPa and sintering at 1000-1400°C, to create translucent Si_3N_4.

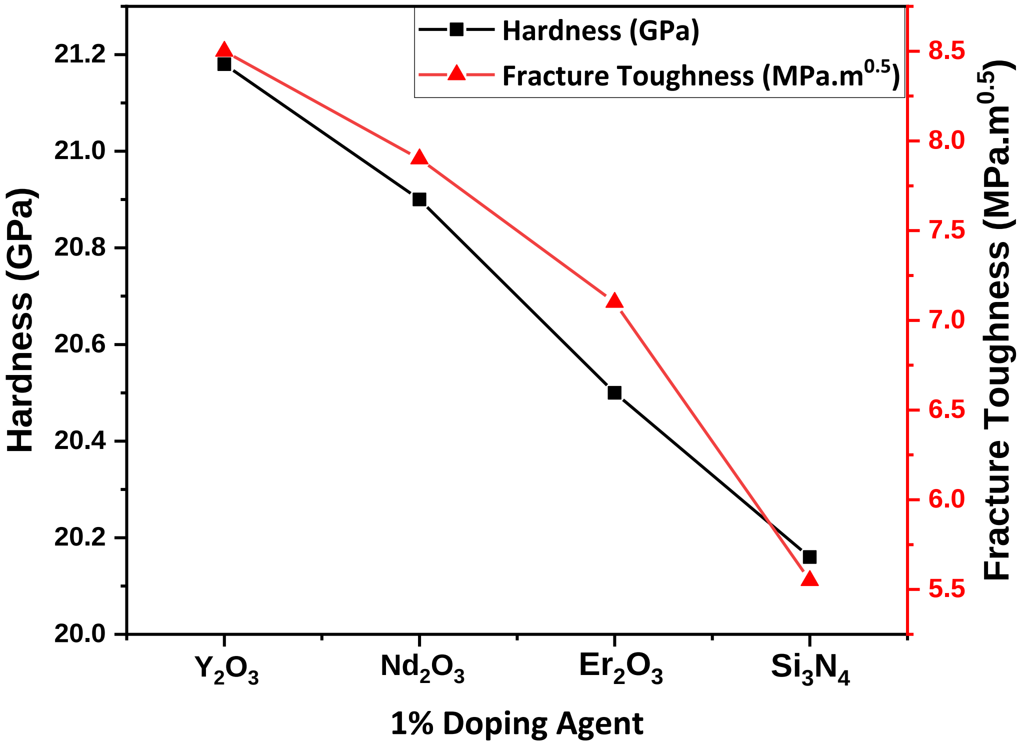

Fig. 15: Doping agent vs. Hardness and Fracture Toughness in Si_3N_4.

Doping agents in Si_3N_4 ceramics affect sliding wear characteristics. Joshi et al. [65] used Y_2O_3, Er_2O_3, and Nd_2O_3 doping agents and developed transparent Si_3N_4 ceramics with 3 wt.% MgO, 9 wt.% AlN, 87 wt.% α-Si_3N_4 and 1% doping agent by hot press technique with a sintering temperature of 1850 °C and a pressure of 30 MPa. The addition of a 1 wt.% doping agent increases hardness and fracture toughness, as shown in **Fig. 15.** Y_2O_3 results out to be one of the most successful doping agents in increasing the hardness and fracture toughness and reducing friction and wear of Si_3N_4, thus improving its tribological behavior. This increase in the mechanical properties reduce the wear of Si_3N_4 at room and elevated temperatures and enhance tribological behavior [61,62]. Translucent single-phase Li-α-SiAlON ceramics were successfully developed using SPS at a heating rate of 100 $^{o}Cmin^{-1}$ for 5 minutes at 1750^{o}C. The results indicate that SPS significantly retards the volatilization of Li_2O due to the quick consolidation process. Within a few minutes, Li-α-SiAlON densification is efficiently accelerated. The resulting sample exhibited a reasonably high infrared transmittance of 57% at 1.4 μm, which is attributed to the dense, homogeneous, and equiaxed-grain microstructure with low amount of intergranular glassy phase. The density, hardness, and fracture toughness of the sintered sample were 3.12 gcm^{-3}, 20.1±0.2 GPa, and 3.0±0.1 $MPa.m^{0.5}$, respectively. These improved mechanical properties show that Li-α-sialon has the potential to be used as a high wear resistance TC [217]. When in the fabrication of transparent Si_3N_4, α-Si_3N_4 transforms to β-Si_3N_4, lower tribological properties are achieved along with low transparency. To enhance the formation of the α phase of the material and suppress that of the β phase, MgO-AlN spinel was used as a sintering additive, reducing the material fracture toughness [221]. To enhance the material fracture toughness, h-BN was used as the sintering additive [90], as it resists the crack propagation by forming a composite material. The wear volume decreased due to the reduced grain pull-out of h-BN and β-Si_3N_4 and the lubrication properties of α-Si_3N_4.

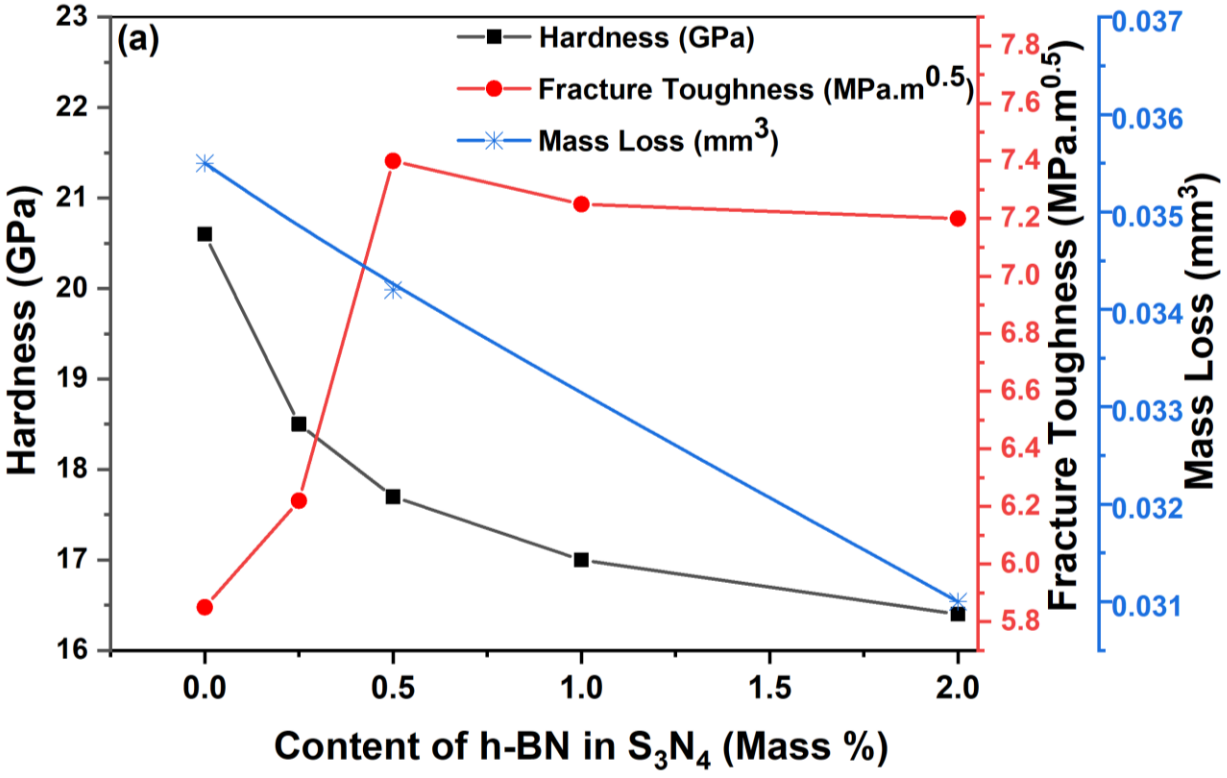

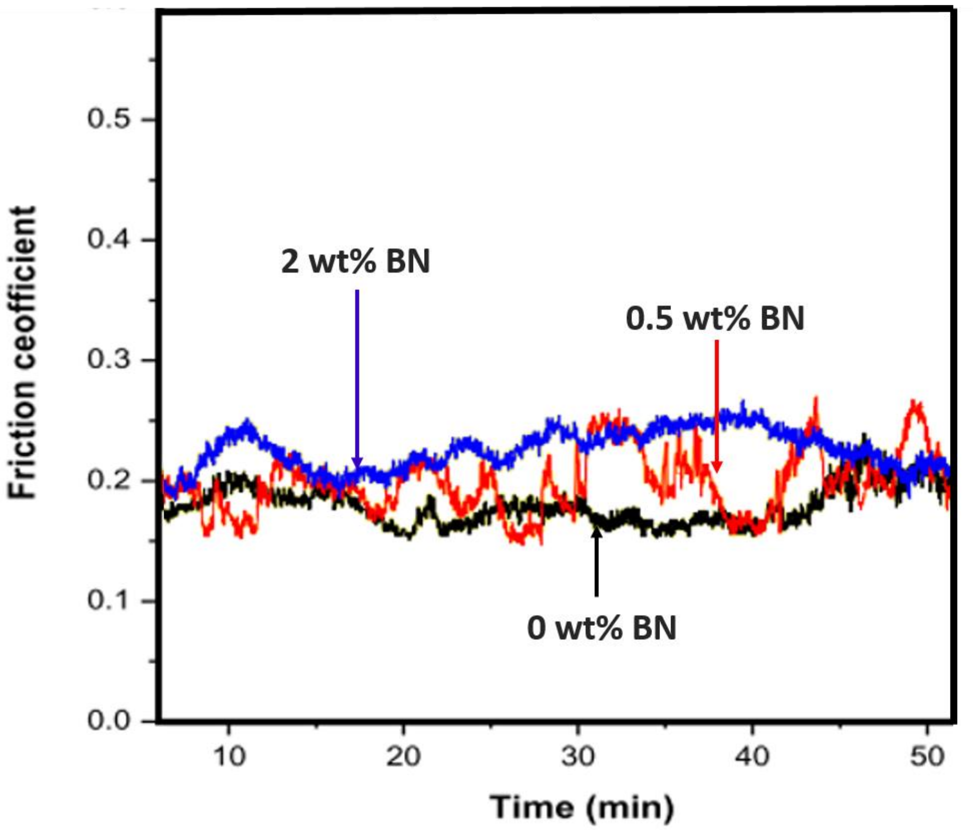

Fig. 16: Variation of a) hardness, fracture toughness, wear volume, and b) friction coefficient with different h-BN content [100].

Tribological properties, like wear volume and coefficient of friction, decreased with an increase in h-BN content (0 mass % to 2 mass %), as shown in **Fig. 16a and Fig. 16b** (redrawn), respectively [100]. The addition of h-BN to Si_3N_4 improved the fracture toughness but reduced the hardness of the transparent ceramic. The fracture toughness of this TC first increased and then slightly decreased with the increase in amount of h-BN to Si_3N_4. Joshi et al. [37] examined the hot-pressed samples of the mixture of α-Si_3N_4, AlN, MgO, and h-BN sintered at 1850°C and 30 MPa, respectively. It was observed that h-BN was dispersed in β-Si_3N_4 after sintering. With the increase in the sintering aid, i.e., h-BN (0.25 to 2 wt%), the density, flexural strength, hardness, and transparency of the material decreased, while the wear resistance and fracture toughness of the TCs was enhanced. With the addition of h-BN, density of the material decreases due to porosity, compromising also transparency. But the fracture toughness of the material with BN content is higher than that without BN content due to the resistance to crack propagation provided by BN content. Also, the fracture toughness increases after adding a small amount (0.25 to 2 wt%) of BN to Si_3N_4- Conversely further addition of BN content showed no further improvement of fracture toughness [37].

Many researchers recommended the fabrication of fine grain-sized α-SiAlON TC as it increases the density of the material. High density and small grain sizes TC provide good tribological properties. Su et al. [101] also commented that α-SiAlON has high optical transmission in visible and IR regions. Besides, the addition of Dy_2O_3, AlN, and Al_2O_3 in α-Si_3N_4 exhibited high hardness and high fracture toughness. Yang et al. [222] examined the effect of mixing different amounts of AlN-MgO, AlN-Y_2O_3, and Al_2O_3-Y_2O_3 systems in Si_3N_4 and observed that the addition of a low amount of sintering aids to Si_3N_4 leads to the formation of β-Si_3N_4, increases the transparency and leads to fine structure, which was opposite to previous results. It is concluded that transparent SiAlON and Si_3N_4 exhibits different tribological properties and transparency by varying the amount of sintering additives. Transparent Si_3N_4 is one of the best transparent materials that can be used for high temperature tribological applications due to its high temperature metastability.

3. Effect of microstructure and mechanical properties

Microstructure (such as pores, grain size, and grain boundaries) of TCs affects their fracture toughness and hardness. In response to the change in the mechanical properties of the TCs then affects the tribological performance of the material [73,223,224]. It was revealed that TCs have a higher hardness and lower mass loss compared to all types of glasses and hence higher wear resistance. It is evident that TCs also show brittle fracture as dominant wear mechanism. To calculate sliding wear in the tribocontact of brittle materials in the absence of any layer development, a sharp indenter model and a blunt indenter model were presented. According to Marshall et al. [225], wear in brittle materials occurs as a consequence of the development and propagation of lateral cracks. For a given applied load (P), total sliding distance (S), hardness (H), fracture toughness (K_{1c}) and elastic modulus (E), wear volume of the brittle solid (V_1) is assessed using the following equation:

$$\boldsymbol{V_1 = \alpha \frac{P^{9/8}}{K_{1c}^{1/2} H^{5/8}} \left(\frac{E}{H}\right)^{4/5} S} \qquad (1)$$

where α is a material constant. When a blunt indenter is placed against a brittle solid, surface ring cracks are created. These cracks spread downward with repeated sliding contact and eventually develop into conical cracks, resulting in material pull-out [226]. With a big data set of wear data, another method for examining wear across materials and operating situations is to study correlational models against crucial material and operational characteristics [227,228]. The basic mechanism of wear in an ideal contact model based on our current knowledge. Wear is regarded as simple asperity-scale abrasion in the mild regime. In this situation, the product of the wear depth, contact breadth, and length of sliding within each "sliding cycle" is used to estimate the wear caused by each asperity contact, as shown in **Fig. 17a**. The "sliding cycle" is defined as the entire slide distance *l* divided by the Hertzian contact width *2a*, i.e., *l/2a*. With these assumptions, mild wear is represented as follows:

$$\mathbf{Wear\ Volume} \propto \frac{\mathbf{P_m}}{\mathbf{H_v}} \frac{\mathbf{N}}{\mathbf{E'}} \mathbf{f(roughness\ parameter)} \times \mathbf{l} \qquad (2)$$

where P_m denotes the mean Hertzian pressure, H_v denotes the hardness, N is the load, E the composite Young's modulus and f is considered as a constant in this analysis. Thus, mild wear was proportional to $P_m \times N \times l$, which was correlated to the operating parameters, and inversely proportional to the material characteristics, H_v and $E^{'}$. Due to the existence of fractures, edge effects from those cracks, and third-body wear particles in the severe wear regime, the asperity contacts might exhibit different properties, as demonstrated in **Fig. 17b**. The entire volume of wear is stated as follows:

$$\mathbf{Wear\ Volume} \propto \frac{\boldsymbol{\sigma}_{\mathbf{max}}(\mathbf{T^*}/\mathbf{T_o})\sqrt{\mathbf{d_{50}}}}{\mathbf{K_{1c}}} \frac{\mathbf{N}}{\mathbf{H_v(T^*)}} \mathbf{l} \qquad (3)$$

where T^* is the nominal contact's interfacial temperature [229], T_o is the ambient temperature set to 20 ^{o}C, K_{1c} is the fracture toughness, d_{50} is the mean grain size, and σ_{max} is the maximum tensile stress. Archard's temperature equation [230] is used to compute the interfacial temperature (T) rise due to friction.

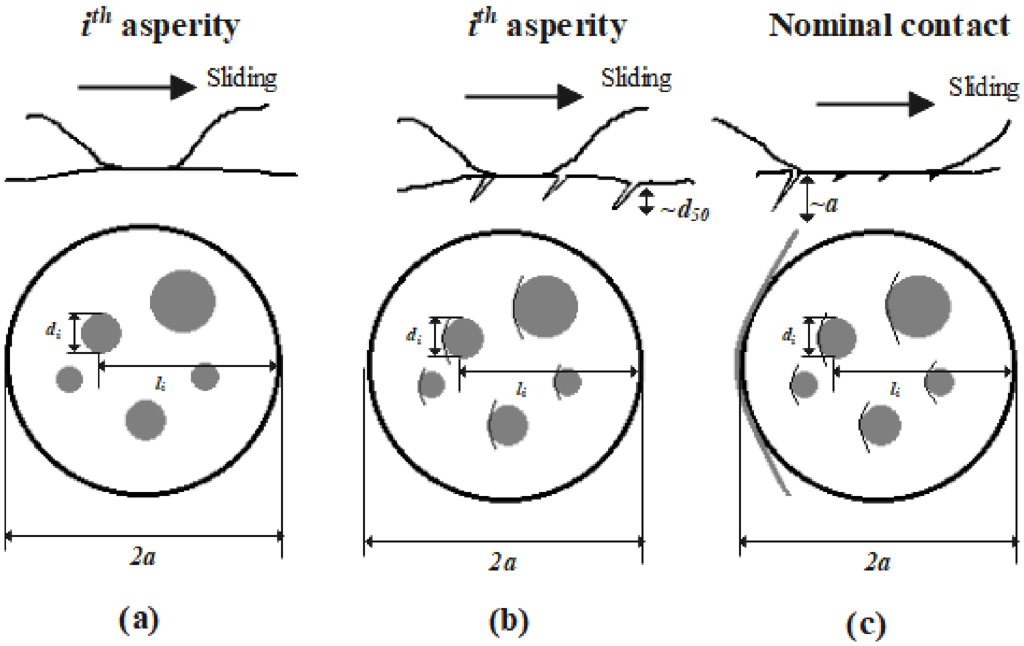

(a) (b) (c)

Fig. 17: Modeling wear in different wear regimes. (a) Asperity-scale abrasion in mild wear regime, (b) tensile cracks inside the nominal contact in severe wear regime, and (c) gross fracture in the nominal contact in ultra-severe wear regime [228].

Thermal shock is attributable to a temperature gradient between the hot patch and the surrounding low temperature region under an extremely severe wear regime. Because the interfacial temperature occurs in a layer with a thickness of half the Hertzian width, the wear equation in Eq. (3) is expanded by substituting a for the d_{50} term; that is, the crack length that affects the stress intensity is equal to *a*, as shown in **Fig. 17c**. This results in the following equation:

$$\boldsymbol{Wear\ Volume} \propto \frac{\sigma_{max}(T^*/T_o)\sqrt{a}}{K_{1c}} \frac{N}{H_v(T^*)} \boldsymbol{l} \qquad (4)$$

where cone crack length, *a*, is given as:

$$\boldsymbol{a} = \left(\frac{\chi P}{K_c}\right)^{2/3} \qquad (5)$$

Increased (T/T_o) ratio and fracture length in combination with a drop in $H_v(T^*)$ should result in a much greater amount of wear compared to corresponding to the extreme wear stated in Eq. *(3)*.

The scratch wear test provides evidence that TCs have higher wear resistance properties than all glasses [66]. Si_3N_4 has superior mechanical and tribological properties compared to glasses and is used in applications like armor, missiles domes, and laser windows for elevated temperatures [231]. However, Si_3N_4 is generally not transparent in the visible range. However, altering the microstructure of transparent Si_3N_4 improves the transparency and mechanical properties of the material. Joshi et al. [36] produced Si_3N_4 transparent in the IR and translucent in the visible region using hot pressing and the addition of h-BN. A small amount of h-BN led to a good densification, but as the h-BN content increased, the performance deteriorated and a higher porosity was observed. It was also found that the presence of inclusions of α-Si_3N_4 and AlN increased the hardness the material. During the fabrication of transparent Si_3N_4 with γ-phase at high pressure (13 GPa) and high temperature (1800°C), the α-phase and β-phase of Si_3N_4 change to γ-phase [44]. The average grain size of γ-Si_3N_4 was 143 nm. The hardness and fracture toughness of TC were 34.9 GPa and 3.5 $MPa \cdot m^{1/2}$, respectively. Similar observations have been reported for other TCs [35,37,38]. High-density transparent $MgAl_2O_4$ with fine grain size exhibits high hardness but low fracture toughness [35].

To improve the transparency of Al_2O_3, a reduction in grain size is the most promising approach [23,45,163]. In the case of Al_2O_3, an increase in sintering temperature results in grain growth which causes birefringence and reduces transparency [232]. The grain refinement of transparent ceramics is required to improve the mechanical behavior, which further enhances the tribological performance of TCs. Therefore, optimum grain size is needed for a combination of good tribological behavior of TCs with good transparency. The reduction of porosity level in TCs improves the mechanical properties and transparency of the materials, leading to a further improvement of their tribological behavior. It is important to note that the impact of even a small amount of porosity is much stronger on the optical quality then on the mechanical properties.

Recent investigations show that the SPS is one of the best techniques to fabricate TCs as it produces small grain structures at low sintering temperatures [55,56]. Alumina ceramics with a transparency of 65.4 % and an average grain size of 200 nm were produced using high-pressure (> 400 MPa) SPS [64,67]. Nishiyama et al. [63] also developed transparent Al_2O_3 ceramics with nanocrystalline grains employing high pressure (7.7 GPa) and low temperature (800°C) SPS method. The resulting samples had a mean grain size of 0.15 µm, with a maximum in-line transmission of 71% at 640 nm for 0.8-mm thick samples. More notably, the transparent Al_2O_3 ceramics exhibited excellent mechanical properties, with average microhardness and fracture toughness of 25.5 GPa and 2.9 MPa-m$^{1/2}$, respectively. So, it is concluded that TCs fabricated by SPS improve the tribological behavior.

Using HIP and a vacuum-pressure slip-casting method, Mizuta et al. [52] produced fine-grained transparent Al_2O_3 ceramics with a transparency up to 46% (1 mm thick) and bend strength of 600–800 MPa. Pre-sintering at 1240°C for 2 hours, with heating and cooling rates of 40°C/min and 5°C/min, was done followed by HIP sintering at 1050–1400°C for 1 hour at 150 MPa, i.e., 30 °C/min to 500 °C, 20 °C/min to 1050°C, and 10 °C/min to the ultimate sintering temperature. During HIP, the pressure raised at a rate of 3.4 MPa/min above 500°C. After sintering at 1350°C, samples reached a maximum transparency of 46%. Grasso et al. [64] also fabricated transparent Al_2O_3 with a grain size of 107 nm and a transparency of 65.4%. This fine structure of TC should provide high mechanical strength and good tribological properties [52]. To better control the grain size of transparent Al_2O_3, dopants like 0.3% zirconia and 0.175% $MgAl_2O_4$ were used by Trunec et al. [53], which increased the transparency by 7-12%. SPS and self-doping techniques were also used to manipulate the grain size of the TC, which affect the mechanical and tribological behavior of the material. Zheng et al. [129] fabricated transparent MgAlON with an approximate grain size of 10 µm by vacuum sintering and HIP. Optically transparent MgAlON is obtained by reactive sintering of a MgO, AlN, and Al_2O_3 powder mixture at 1650°C for 15 hours. The fabricated TC yield 40% increase in the mechanical strength due to the Hall Patch effect and twin lamella strengthening mechanism. Therefore, it is considered as a promising candidate material for tribological applications. Zheng et al. [177] also developed transparent LiAlON with no porosity by reactive sintering at 1750°C for 20 hours of powders AlN, Al_2O_3, and $LiAl_5O_8$, which eliminated Al_2O_3 secondary phase and porosity to obtain TC with maximum transparency of 85.5%. The hardness and flexural strength of developed TC were 15 GPa and 303 MPa, which provide good wear resistance to the material. The tribological performance of transparent $MgAl_2O_4$ fabricated by SPS at 73 MPa with different sintering temperatures shows that the friction coefficient and mass loss increase with an increase in sintering temperature [35]. The variation in the mass loss during the wear experiment of transparent spinel with the deviation of hardness and fracture toughness is depicted in **Fig. 6**. High hardness and low fracture toughness achieved at low sintering temperature were suitable for low mass loss during wear. Fracture toughness is highly affected by the microstructure of materials. It is enhanced by encouraging strengthening processes such as grain bridging, which absorbs some of the energy required to propagate fractures.

Lopez et al. [54] also showed that the hardness of TCs increases with decreasing the grain size whereas, the fracture toughness remains the same with the decrease in grain size. The lubricated sliding wear of three transparent $MgAl_2O_4$ spinel materials with various grain sizes designated as Nano (345nm), Fine (2.1µm), and Coarse (15 µm) has been studied. Fine $MgAl_2O_4$ has traditional wear behavior, including mild wear, followed by a rapid shift to severe fracture-controlled wear. A significant grain pull-out was observed on worn surfaces of Fine $MgAl_2O_4$, which is compatible with the intergranular mechanism of fracture. Compared to Fine $MgAl_2O_4$, Nano and Coarse $MgAl_2O_4$ both demonstrate a progressive transition from moderate to severe wear and have substantially lower overall wear rates. Both Nano and Coarse $MgAl_2O_4$ have worn surfaces that show transgranular fracture and material loss, similar to lateral-crack driven chipping. Stronger grain boundaries in Nano $MgAl_2O_4$ is ascribed to the Y_2O_3 sintering additive employed for grain refining, which might explain the transgranular fracture mode. At the same time, the transgranular fracture seen in Coarse spinel might be due to the enormous size of the grains in that spinel. The fracture surfaces of pure $MgAl_2O_4$ spinel (**Fig. 4a and Fig. 4b**) and spinel with-1 wt% Si_3N_4 (**Fig. 4e**), show that in the latter the grain size is significantly smaller [48]. The same is true for spinel with 3 wt% Si_3N_4, (**Fig. 4g**) which exhibits much smaller grains on the fracture surface than pure spinel. However, in this sample, it seems as if the density of voids had a stronger correlation with the fracture toughness of nanocomposite samples. The fracture toughness of pure spinel, spinel-1 wt% Si_3N_4, and spinel-3 wt% Si_3N_4 was 5.1, 5.3, and 3.1 $MPa.m^{0.5}$, respectively. The similarity of the toughness values in pure spinel and spinel having 1% Si_3N_4 indicates that 1% Si_3N_4 has a minimal impact on the toughness of spinel composites. Gledhill et al. reported a toughness of 1.3 $MPa.m^{0.5}$ for an unheated composite, lower than the value obtained in previously discussed research [17]. The hardness of pure spinel, spinel-1 wt% Si_3N_4, and spinel-3 wt% Si_3N_4 was 7.7, 8.1, and 10.2 GPa, respectively. Heat-treated samples provide a greater hardness value than unheated samples. The combined effect of high hardness and high fracture toughness is observed in the spinel-1 wt% Si_3N_4 and is believed to provide good wear resistance. On the other hand, the presence of voids or secondary phases has a deteriorating effect on the transparency of ceramics, in particular in the visible range. Thus, a careful optimization is required.

Fig. 18 provides a comparison of hardness and shear modulus of different TCs. The cubic Si_3N_4 results as the third hardest transparent material after diamond and c-BN [72]. The excellent mechanical properties will most likely lead to excellent tribological performance of the material. In the case of TCs, there is a very significant relationship between grain size and wear resistance. TCs have the highest hardness and lowest mass loss during the scratch wear test with the load increasing progressively, which provides high wear resistance properties to TCs.

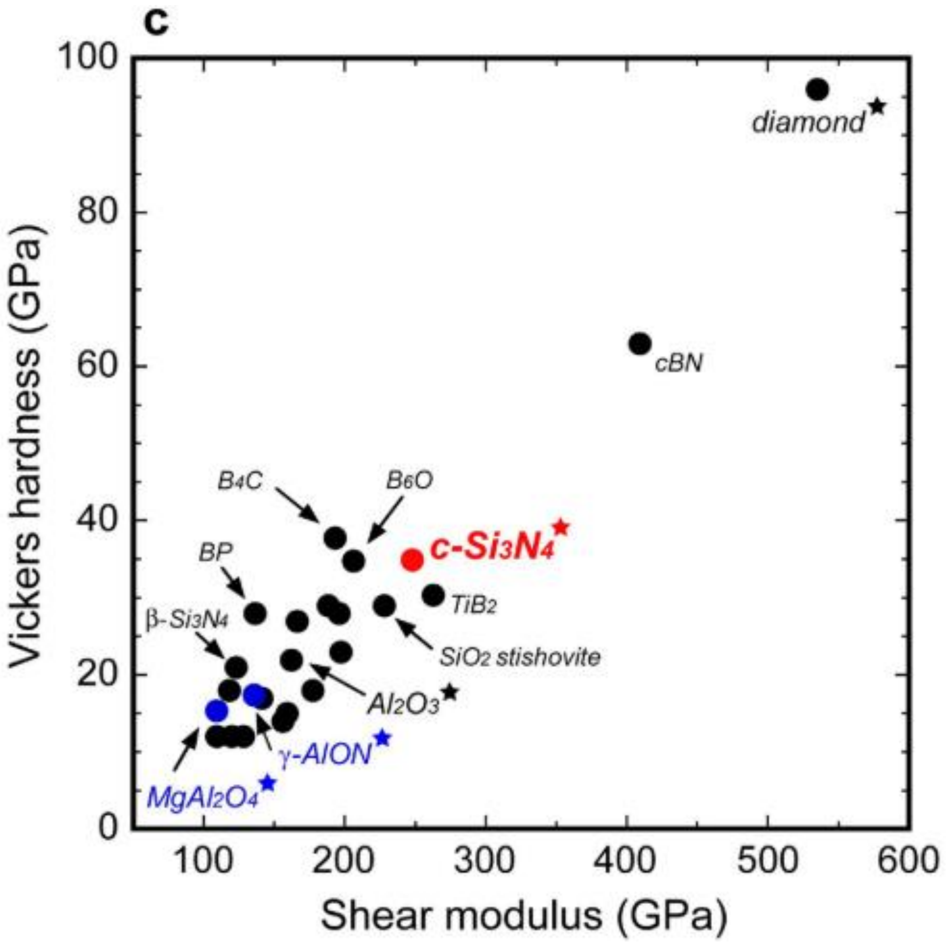

Fig. 18: VIckers Hardness (1kg) of cubic silicon nitride compared to other super-hard ceramics [83].

TCs can be produced by SPS or by vacuum sintering. Compared to single crystals, the transmittance of ceramics is lower due to scattering, as described in section 1 and illustrated in **Fig. 2**. Light scatters mainly on secondary phases, grain boundaries and pores [26], which is minimized by improving powder processing and ceramic fabrication methods. Lopez et al. [54] observed the change in the microstructure when different grain sized TC is subjected to wear. The material removal from the surface of the coarse and nano grained TCs experience transgranular fracture while performing sliding wear test. In contrast, fine grain size TCs i.e., the grain size between coarse grain and nano grain experience intergranular fracture during sliding wear. The micrographs of fracture surface for coarse, nano and fine grain after sliding wear are shown in **Fig. 19a, Fig. 19b, and Fig. 19c** respectively.

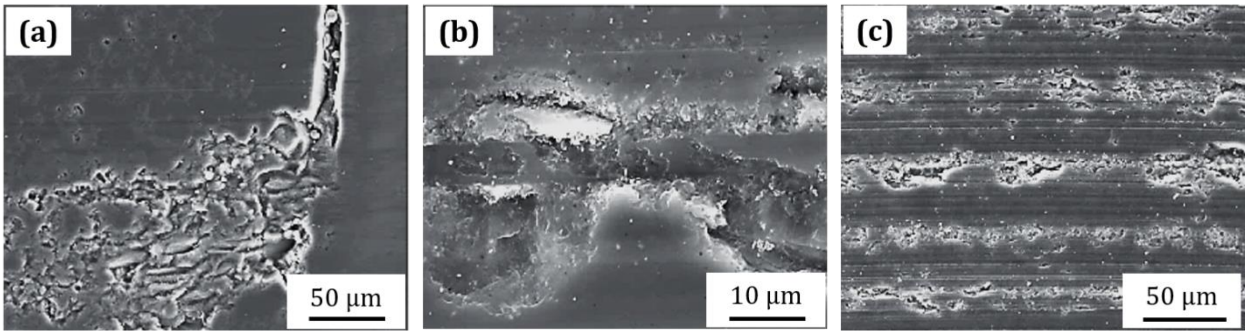

Fig. 19: SEM micrographs of fracture damage in wear scars in a) coarse spinel, b) nano spinel and c) fine spinel at the end of the sliding wear test (1000 min) [54].

Subsurface damage induced in the nanoscratch changes the mechanical properties of the TC [184]. Zang et al. [184] investigated the wear performance of Lu_2O_3 TCs by single nanoscratch, repeated nanoscratch, and double nanoscratch experiments on a nanoindenter. After the first scratch, the residual material changed to a combination of polycrystalline nanocrystallites and amorphous from original micron-size grains. At the same time, many defects, *viz.*, dislocations, stacking faults, nano twins, torsion of an atomic plane, fracture of the atomic plane, and wrong arrangement of the atomic plane were induced in nanograins during the nanoscratch process. The mechanical property of a combination of polycrystalline nano-crystallites and amorphous phases with many atomic-scale defects was different from that of micron-sized grains. These changes of mechanical properties result in the decrease of friction coefficient in the repeated scratch.

Table 4 shows the mechanical, optical, and tribological behavior of different TCs and **Table 5** shows the potential tribological behavior with respect to improved mechanical properties of TCs. **Fig. 20a and Fig. 20b** show the comparison of mechanical properties (hardness and fracture toughness) and transparency of selected TCs. In the case of spinel, Y_2O_3, Si_3N_4 or SiAlON the change that led to an increase of hardness led also to a better transparency, while in the case of fracture toughness such a trend is not fully clear. All these properties are highly microstructure-dependent, but not always in the same way.

Table 5: Mechanical, optical, and tribological behaviour of TCs.

Material	Sintering Additives	Sintering Parameters	Transparency (%)		Mechanical Properties			Tribological test parameters	Coefficient of friction	Wear Vol. mm^3/ Rate mm^{3}Nm^{-1}	Microstructure	Tribological outcomes	Ref.
					Relative Density (%)	Hardness (GPa)	Fracture Toughness (MPa.m$^{0.5}$)						
Si_3N_4 (3wt.% MgO + 9wt.% AlN + 1 wt.% REO) (α phase)	Y_2O_3 1wt%	Type- HP Atmosphere- N_2 Pressure- 30 MPa Sintering Temperature- 1850 °C Holding Time- 60 min	54	From 500-2500 nm	99.6	21.1	8.5	Load-10N Time-30min Reciprocating	0.33	-	Lower β phase than undoped silicon nitride with interwoven structure. Grain pull-out showed abrasive wear during sliding	Increased hardness and fracture toughness result in a reduction in coefficient of friction.	[65]
	Nd_2O_3 1wt%		50		99.5	20.9	7.9		0.36				
	Er_2O_3 1wt%		40		99.3	20.5	7.1		0.39				
	None		64		99.0	20.1	5.9		0.41				
Si_3N_4 (3wt.% MgO + 9wt.% AlN + BN) (α phase)	h-BN (0.25%)	Type- HP Atmosphere- N_2 Pressure- 30 Sintering Temperature- 1850 Holding Time- 60	57	From 500-2500 nm	96.7	18.5	6.2	Time-60min Reciprocating	-	0.0350 mm^3	Debris of α-Si_3N_4 made a thin film and decreased wear volume.	Decrease in hardness and increase in fracture toughness results in decreased cof and wear volume	[37,100]
	h-BN (0.5%)		43		93.6	17.75	7.4		0.21	0.0345 mm^3			
	h-BN (1%)		40		92.3	17	7.3		-	0.0320 mm^3			
	h-BN (2%)		25		90.1	16.5	7.3		0.19	0.0280 mm^3			
	None		-		99.0	20.5	5.9		0.24	0.0355 mm^3			
Spinel ($MgAl_2O_4$)	Commercially available TC was used for the experimentation		Highly transparent		99.5	14.12 ± 0.77	-	Linear reciprocating ball- on-disc Counter-body- Al_2O_4 Load- 20N Velocity- 5000 ms^{-1}	0.42 ± 0.02	0.094 ± 0.02 mm^3/ 4.72 ± 1.22 mm^3 Nm^{-1} (for 1000m) 0.316 ± 0.05 mm^3/ 5.27 ± 0.85 mm^3 Nm^{-1} (for 3000m)	-	As the sliding distance increases, the rate of wear increases. On the surface, parallel arrays of fatigue fractures perpendicular to the sliding direction were discovered, suggesting fatigue type wear.	[28]
AlON	Commercially available TC was used for the experimentation		Highly transparent		99.6	16.33 ± 0.5	-	Linear reciprocating ball- on-disc Counter-body- Al_2O_4 Load- 20N Velocity- 5000 ms^{-1}	0.45 ± 0.02	0.250 ± 0.01 mm^3/ 12.5 ± 2.16 mm^3 Nm^{-1} (for 1000m) 0.606 ± 0.03 mm^3 10.1 ± 0.27 mm^3 Nm^{-1} (for 3000m)	-	On the surface, parallel arrays of fatigue fractures perpendicular to the sliding direction were discovered, suggesting fatigue type wear. It was discovered that as the sliding distance increased, the wear rate steadily dropped until it reached a constant value.	[28]

Lu_2O_3	Commercially available TC was used for the experimentation	Highly transparent	-	10.95	-	Single Nanoscratch	0.272±0.02	-	Grain boundaries in Lu_2O_3 TCs are extremely weak, and the mismatch degree between neighbouring grains is high. As a result, subsurface fractures cracks propagate along grain boundaries	The friction coefficient rises and tends to remain steady with increasing normal force in repeated nanoscratch testing. Lu_2O_3 TCs undergo ductile deformation during the nanoscratch process as a result of a combination of polycrystalline nanocrystallites in the inner grain and amorphous transformation. Intergranular fractures are the most common kind of subsurface crack propagation for Lu2O3 TCs. Additionally, a few transgranular and discontinuous fractures are detected in the subsurface.	[184]
						Repeated Nanoscratch	0.245±0.03				

Table 6: Potential tribological behaviour with respect to improved mechanical properties of TCs.

Material	**Experiment condition**	**Sintering Parameters**	**Transparency (%)**		**Mechanical Properties**				**Microstructure**	**Potential Tribological outcomes**	**Ref.**
					Mean grain size (nm)	**Relative Density (%)**	**Hardness (GPa)**	**Fracture Toughness ($MPa.m^{1/2}$)**			
Si_3N_4 (α phase) <0.5 µm	Additive- MgO (10nm) 12wt%	Type- SPS Atmosphere- N_2 Pressure- 50 MPa Sintering Temperature- 1850 °C Holding Time- 5 min	~ 0	From 400-900 nm	290	97	12.1-13.1	6.7-7.7	β phase was formed after sintering. No change in the mean grain size, i.e., 0.29µm of transparent Si_3N_4, was observed with a change in percentage of MgO, but the mean grain size was reduced from 0.37 µm to 0.34 µm when Y_2O_3 was increased from 2% to 12%.	2 wt% Y_2O_3 in Si_3N_4 provide high wear resisting properties to the TC.	[99]
	Additive- Y_2O_3 (0.7µm) 12wt%		~ 0		340	99.8	13.4-14.0	6.3-7.1			
	Additive- Al_2O_3 (0.5µm) 12wt%		-		-	95.3	-	-			
	Additive- MgO (10nm) 2wt%		~ 0		290	99.3	14.0-16.0	6.4-6.6			
	Additive- Y_2O_3 (0.7µm) 2wt%		0–35		370	99.9	14.9-15.9	6.1-6.7			
	Additive- Al_2O_3 (0.5µm) 2wt%		-		-	85.9	-	-			
Y_2O_3 (<74µm)	Heating rate- 10 °Cmin^{-1}	Type- SPS Pressure- 70 Sintering Temperature- 1250 °C Holding Time- 10 min	46		499	-	-	1.1	With an increase in the heating rate, the mean grain size of transparent Y_2O_3 was decreased significantly	Rapid heating results in tiny grain size and increased fracture toughness, which result in increased wear resistance.	[95]
	Heating rate- 20 °Cmin^{-1}		49		410			1.4			
	Heating rate- 50 °Cmin^{-1}		64		205			1.3			

	Heating rate- 100 °Cmin^{-1}		66		164			1.3			
Y_2O_3 (90nm)	Preload Pressure – 10MPa	Pressure conditions- It was increased to 100 MPa at 1000 °C and was kept constant during sintering and cooling Heating rate conditions- 100 °C/min 600°C, 25°C/min 1000°C, held 5 minutes, 10°C/min 1300 °C	76.7	At 200 nm	260	99.4	8.32 ± 0.18	1.25 ± 0.07	Increase in preload pressure result in a reduction in mean grain size, but no phase transition is seen.	When preload pressure is increased, the hardness and fracture toughness values fall, resulting in poorer wear resistance.	[94]
	Preload Pressure – 30MPa		70.2		320	98.8	7.56 ± 0.16	1.20 ± 0.05			
	Preload Pressure – 50MPa		51.1		450	98.7	7.01 ± 0.20	1.14 ± 0.04			
$MgAl_2O_4$	0 wt% LiF	HP vacuum sintering at 1600 °C for 60 min	34	At 1100 nm	3 ± 0.8 38 ± 13	-	-	-	Bimodal microstructure converted to equal grain size distribution with increase in wt% addition of LiF	The inclusion of LiF results in a fine structure and low porosity, which improves the hardness and, therefore, the tribological properties.	[60]
	0.5 wt% LiF		40		20 ± 10						
	1 wt% LiF		44		18 ± 14						
$MgAl_2O_4$	0 wt% Si_3N_4	SPS with maximum pressure and temperature of 80 MPa and 1550 °C for 20 min and heat treated	75	At 2500 nm	-	-	8.2	-	The porosity of the composite material increased with increase in the addition of Si_3N_4	$MgAl_2O_4$-1 wt% Si_3N_4 has a maximum shear strength, indicating that it has the greatest fracture toughness and the potential for the best wear resistance.	[48]
	1 wt% Si_3N_4		71				9.3				
	3 wt% Si_3N_4		58				12.1				

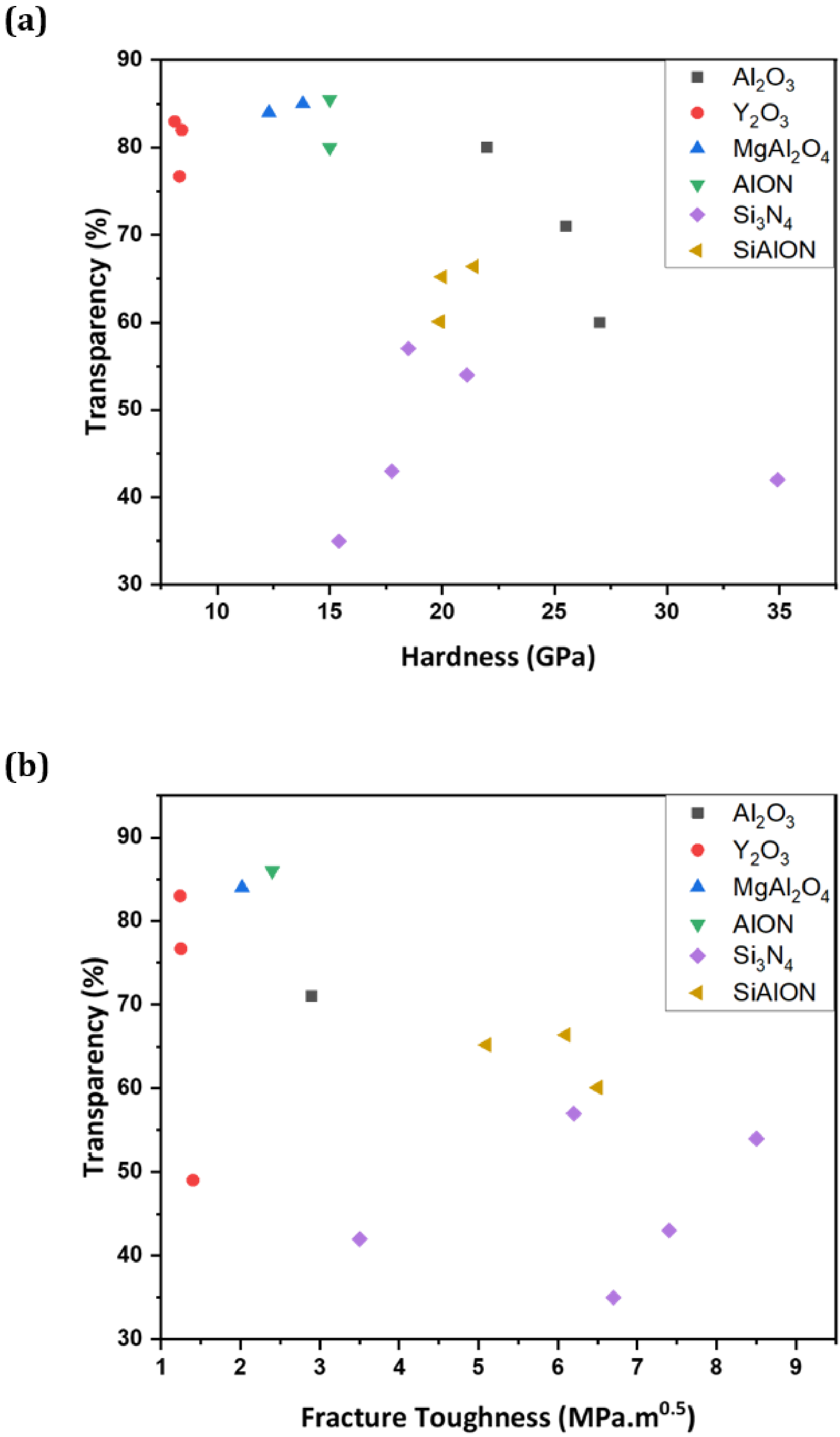

Fig. 20: Transparency vs. a) Hardness, and b) Fracture Toughness for different TCs [27,37,59,63,65,75,83,86,92–101,111,112]

The effect of pressure during sintering has various conflicting outcomes for the change in the microstructure of the TCs. When it comes to transparent cubic zirconia (c-ZrO_2), the studies established no effect of pressure on grain growth [233,234]. However, another study [235] found an increase in grain size when the pressure was increased, which decrease the wear resistance. On the other hand, a study [236] found both phenomena to occur: a minimal pressure influence on grain growth at low temperature (1100°C) and a considerable pressure effect on grain growth acceleration at high temperature (1200°C).

In addition, when compared to pressureless sintering under vacuum, the use of pressure-assisted methods allows the use of lower sintering temperatures. The densification is one of the significant factors for wear resistance because densification and reduction of porosity during sintering affect the tribological performance of the TC. When SPS is used to obtain transparent ceramics, sintering occurs from inside to outside of the sample for the low heating rate at high pressure (400 MPa) [236], and from outside to inside for high heating rate at low pressure (80 MPa) [237]. The increase in pressure allows to reduce the sintering temperature and to develop a fine grain size [47,238]. Kim et al. [236] also studied the pressure effect on the grain and grain boundary of the MgO-doped transparent Al_2O_3. It was observed that the compressive pressure [239] lowers both the free volume and the transfer of atoms between grain boundaries, resulting in reduced grain-boundary mobility and decreasing the wear resistance of the TC. Consequently, the increase in the hydrostatic pressure leads to the densification of the polycrystals and to a decrease of the grain growth rate.

It is concluded that the pressure increase during sintering should lead to the production of TCs with a fine structure and a low grain-boundary movement, which in turn increase the wear resistance of these materials.

4. Mechanisms of material removal

Wear modes vary according to the materials in contact, working load, mode and speed of relative motion, temperature, lubrication conditions, and environment. As a result, wear mechanisms vary considerably from case to case [240]. In addition, the predictive and quantitative modelling of the wear mechanism is complicated compared to contact mechanic issues. This section includes discussions on a material removal mechanisms in terms of material properties during the tribological application of TCs. Different friction and wear coefficients between different tribopairs indicated complicated material removal processes. The change in the microstructure and mechanical properties of the TCs affects its material removal mechanism [73,223,224]. The densification of TCs and the respective sintering conditions also affect the material removal mechanism during wear.

Abrasive particles develop during the wear process due to work hardening, phase changes, and the creation of a third body at the interface during sliding [241]. When hard asperities or hard particles travel over a soft surface, as well as when hard particles travel over a hard surface, abrasion occurs in both cases [145]. There are three types of mechanisms observed during abrasive wear, i.e., micro-cutting, wedge formation, and ploughing [242,243], as shown in **Fig. 21**. When the hard particles slide over a soft surface it result in formation of debris. When the debris is produced in form of chips, the mechanism is called micro-cutting. The wedge formation is observed when the abrasive particles slide on the material and the material deposit at certain position. The micro-cutting and wedge formation of abrasion are generally observed for low scratch length during sliding [244]. However, if debris is not formed, the action is called ploughing. Both cutting and ploughing result in plastic deformation and strain hardening of the material which improve the hardness and wear resistance of the material. This is not the case when hard asperities travel over a hard surface as no plastic deformation is possible for brittle material. Therefore, three types of cracks are observed in the material, i.e., radial, median and lateral cracks (**Fig. 3**). Studies reveal that the wear behaviour of TCs is abrasive [35,37,65,66].

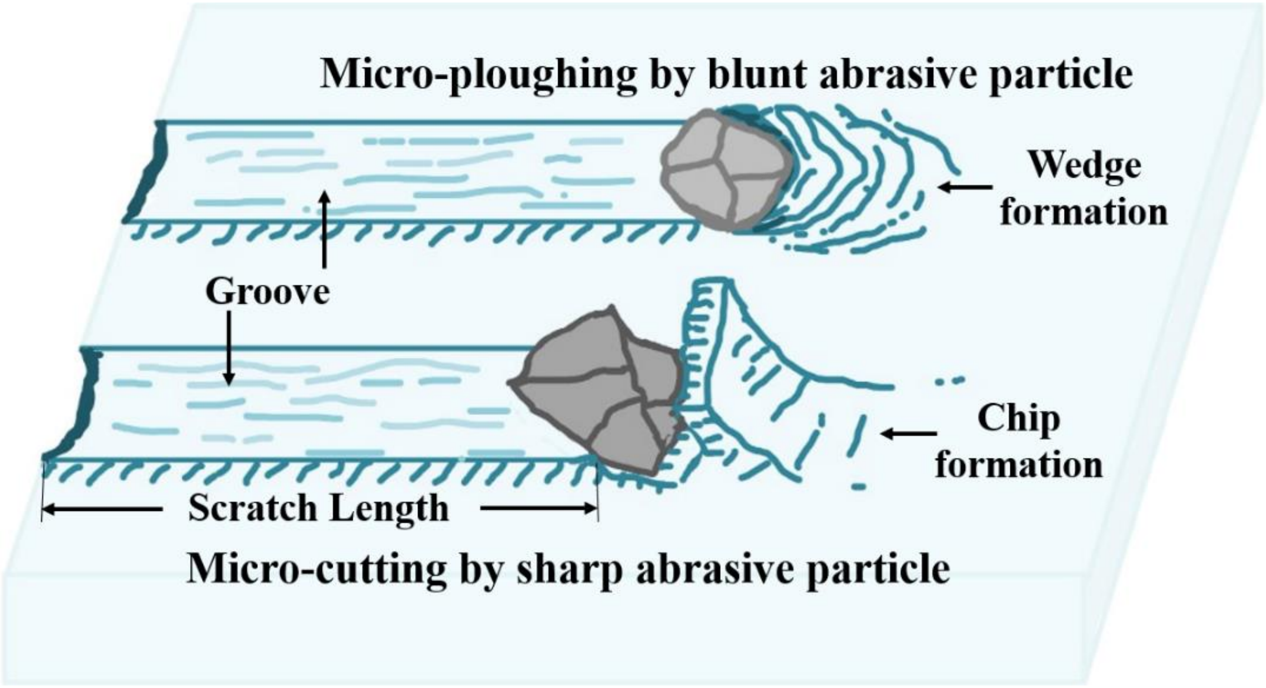

Fig. 21: Types of mechanisms observed during abrasive wear depending on abrasive particles.

Joshi et al. [37] depicted that worn surfaces on transparent Si_3N_4 were formed due to the pulling out of grains during the wear experiment, with an abrasive wear. Also, if the grains of doping agents are more easily pulled, because of the interlocking of the asperity and the grain of the doping agent, the abrasion increases. The interlocking of abrasive particles and doping particles and their wear is shown in **Fig. 22a and Fig. 22b**. The grain size of the doping agents and of the parent phase must be similar for low abrasive wear rate. The shape of the grain also affects the wear behaviour, like β-Si_3N_4 has a large elongated grain structure compared to α- Si_3N_4, and indeed α- Si_3N_4 has better tribological characteristics [65]. Similarly, the incorporation of nano twins into nanostructured polycrystalline cBN results to form equiaxed grains, which led to an increased hardness and improved wear resistance of TC.

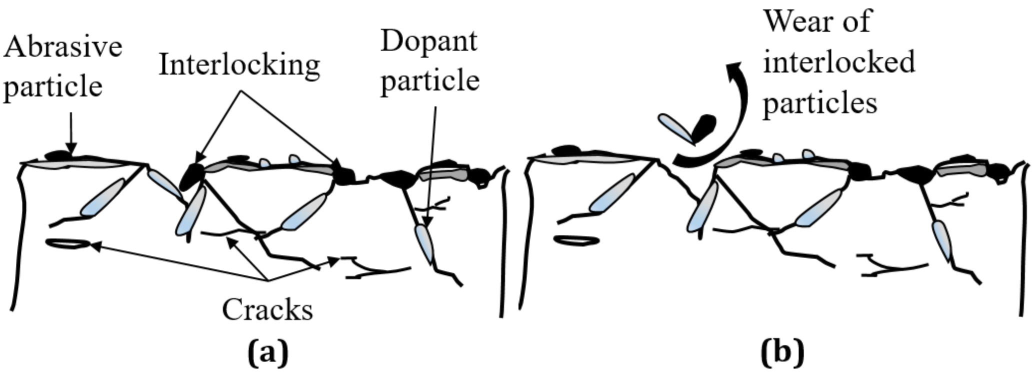

Fig. 22: Representation of a) interlocking of abrasive and doped particle, and b) their wear during sliding of abrasive particle on transparent ceramic.

To understand the wear mechanism, a scratch test was performed on transparent $MgAl_2O_4$ [66]. Three different regimes were distinguished along the scratch direction *viz.*, micro-ductile, micro-cracking, and micro-abrasive as discussed previously in **Fig. 3**. In every regime, the transport and removal of material are governed by abrasive wear. Different types of cracks are intensely influenced by applied load and stress. The median, radial, and lateral fractures contribute to the characteristic wear pattern. Scratch testing was also used to analyze the mechanical and tribological properties of transparent Lu_2O_3, as mentioned in **section 2.4**. Hard-brittle transparent materials with a brittle surface deformation characteristic and a material removal process were studied, and the results offered valuable information [184]. Several imperfections, comprising dislocations, stacking faults, nano twins, atomic plane torsion, atomic plane fracture, and atomic plane misalignment were produced in nanograins due to the nanoscratch process. All kinds of defects interacted differently towards material removal during scratching. When scratching TCs, the interaction between scratches has a significant effect on the material removal mechanism. While performing the scratch experiment, the material removal mechanism is dependent on scratch length. A ductile material removal mechanism is observed if the scratch length is large and brittle for a small scratch length [244].

Benaissa et al. [35] fabricated various $MgAl_2O_4$ TCs by SPS at different sintering temperatures and observed after tribological testing that these samples had an abrasive wear mechanism. Besides, it was also noted that the friction coefficient changed in a specific way for each sintering temperature variation. The authors further pointed out that the mass loss increased during wear as the sintering temperature increased. The wear volume of the TC was found to be proportional to its hardness. The hardness of TCs increases with the reduction of the sintering temperature as the grain size decreased and the hard TC prevent the particles being pulled away from the surface. On increasing the grain size of the sintered samples during high sintering temperature, the grain pulled-out and abrasion wear of TCs increased. As the wear rate and mechanism is directly related to the mechanical properties of the material, Zhao et al. [174] observed wear mechanism for TC with additives. The nano-sized silicon carbide (SiC) and zirconia (ZrO_2) particles were added to AlON by hot-press sintering which significantly increased the mechanical characteristics (relative density, microhardness, Young's modulus, flexural strength, and fracture toughness). Additionally, the fracture mode in the nanoparticle reinforced composites shifted from intergranular to mixed cracking. Numerous toughening mechanisms, including fracture deflection, crack bridging, and crack branching, were found in SiC and ZrN nanoparticulate reinforced AlON composites. These methods successfully enhanced crack propagation resistance, resulting in a 41.4% and 28.6% increase in flexural strength and fracture toughness, respectively, when compared to pure AlON.

To understand the ductile deformation mechanism of transparent Lu_2O_3 during sliding wear, transmission electron microscopy was conducted [184]. It was observed that subsurface of TC contains three types of grains beneath the scratch, as shown in **Fig. 23a and Fig. 23b**. The first scratch is concentrated on Grain 1, whereas the second scratch is concentrated on Grain 3. When the cutting depth was within a particular depth, there was a visible plastic flow area with no subsurface cracks, indicating that the machining process was entirely ductile. The transmission electron microscopy pictures suggested that the process included a combination of polycrystalline nanocrystallites inside the inner grain and amorphous transition, as shown in **Fig. 24a**. Numerous defects, including as dislocations, nano twins, stacking faults, twisting of atomic planes, misalignment of atomic planes, and fracturing of atomic planes were produced in nanograins created during the nano-scratch process as a consequence of the stress field (**Fig. 24**). When single crystal grains transform into polycrystalline nanocrystallites, the plastic deformation mechanism shifts from intragranular dislocation to grain boundary movements, such as grain sliding [246,247], grain rotation [248–251], and grain migration [252]. This is similar to previous research on the ductile deformation mechanism of $Gd_3Ga_5O_{12}$ single crystals [245]. Alike previous research on the ductile deformation mechanism of $Gd_3Ga_5O_{12}$ single crystal, when single crystal grains transform into polycrystalline nanocrystallites, the plastic deformation mechanism shifted from intragranular dislocation to grain boundary movements, such as grain sliding, grain rotation, and grain migration. Specifically, the scratch subsurface of Grain 3 was separated into three regions, as shown in **Fig. 24b**: the plastic flow region, the transitional region, and the grain matrix. In the plastic flow zone, a significant quantity of residual stress was discovered. Furthermore, the nano grains of the plastic flow zone include a large number of flaws that were produced during the machining process (**Fig. 24c and Fig. 24d**).

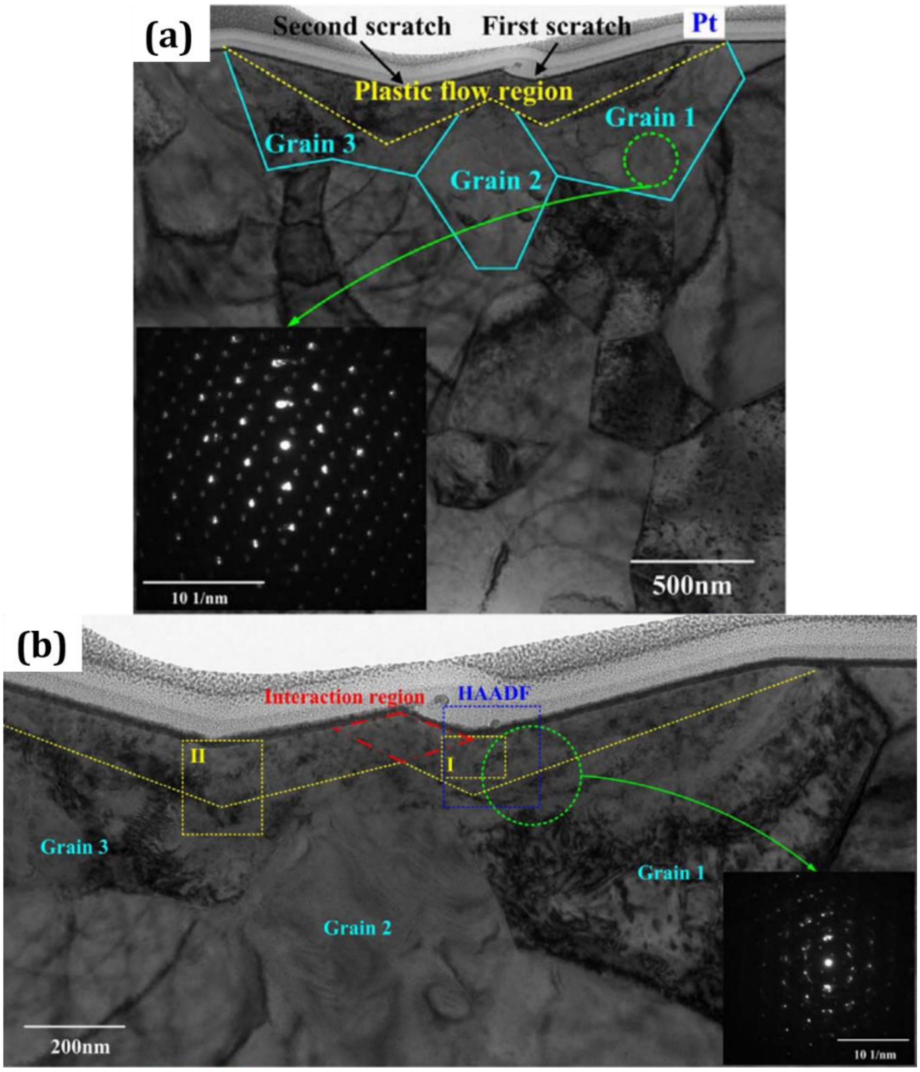

Fig. 23: Transmission electron micrographs of transparent Lu_2O_3 during sliding wear [184].

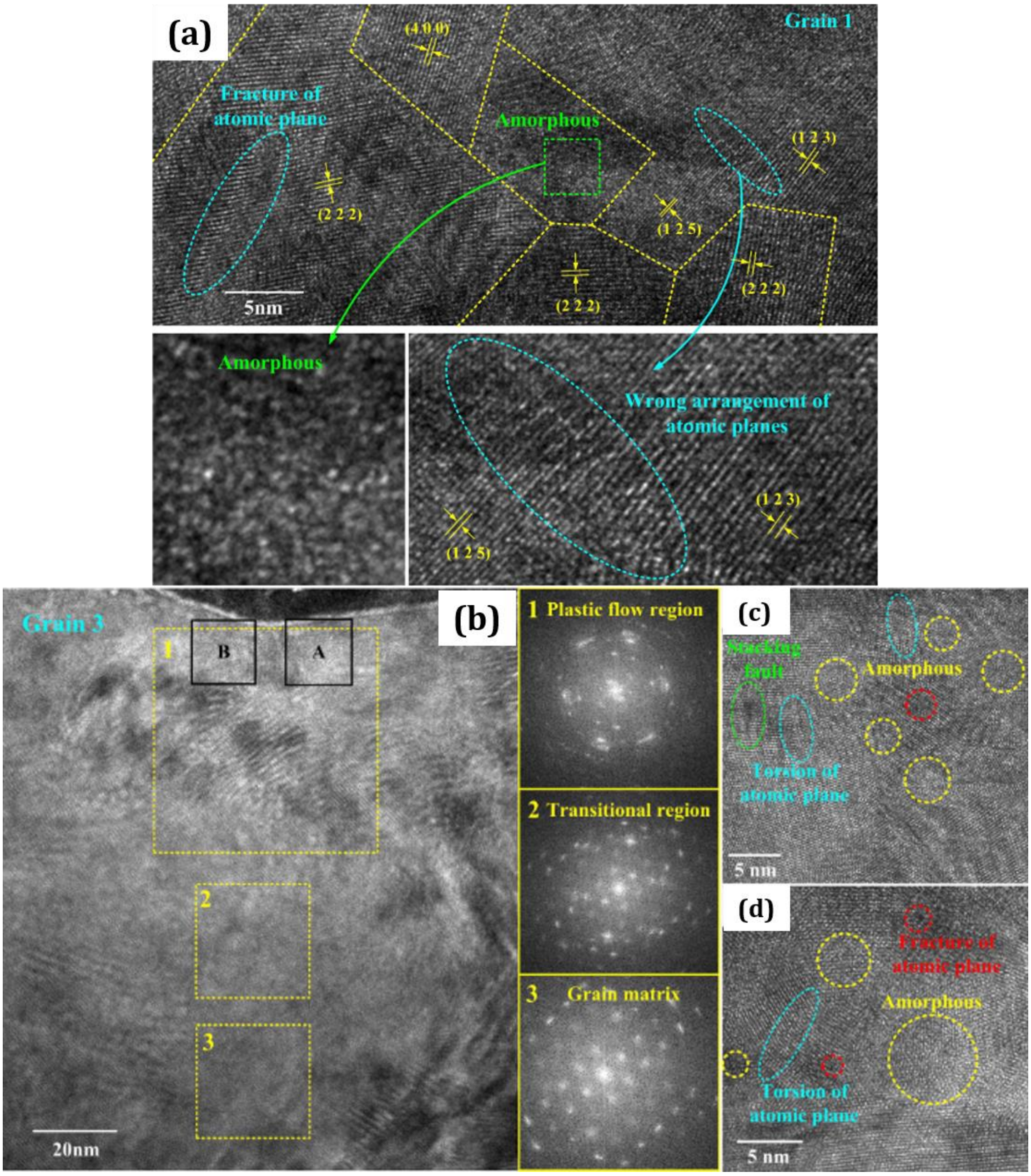

Fig. 24: High-resolution transmission electron microscopy of sections a) I, and b) II shown in figure 22b. c) and d) represent the types of flaws formed beneath scratch [184].

Microstructure refinement generally leads to a significant increase in hardness. The hardness of the TC is affected by numerous factors. The wear volume of the TC is found to be proportional to its hardness. TC's hardness increases as the grain size decreases, and the hard TC resists surface wear [35]. Sheikh et al. [51] also investigated transparent $MgAl_2O_4/Si_3N_4$ nanocomposite for hardness, fracture toughness, and transparency. The decrease of transparency and enhancement in mechanical properties is due to the presence of Si_3N_4 reinforcing nanoparticles and the relative toughening mechanism of $MgAl_2O_4$. **Fig. 25a, Fig. 25b, and Fig. 25c** illustrates the surface morphologies of the wear surfaces of TC sintered at 1300°C, 1350°C, and 1400°C, respectively. The grain size obtained at a higher sintering temperature is considerably higher than that obtained at a lower temperature. At all sintering temperatures, wear surfaces of the transparent spinel showed some grooves, demonstrating that abrasion wear was the dominant mode of wear in sintered samples. It was evident that increasing the grain size of the sintered sample resulted in increased abrasion wear. The addition of Dy_2O_3 to Si_3N_4 combined with AlN and Al_2O_3 resulted in a TC with a high fracture toughness and hardness. No glassy phase was observed at the grain boundary coupled with a homogeneous microstructure with equiaxed grains [101]. The addition of a doping agent provided a homogenous crystalline microstructure with increased hardness and fracture toughness resulting in improved wear resistance with a change in material removal mechanism.

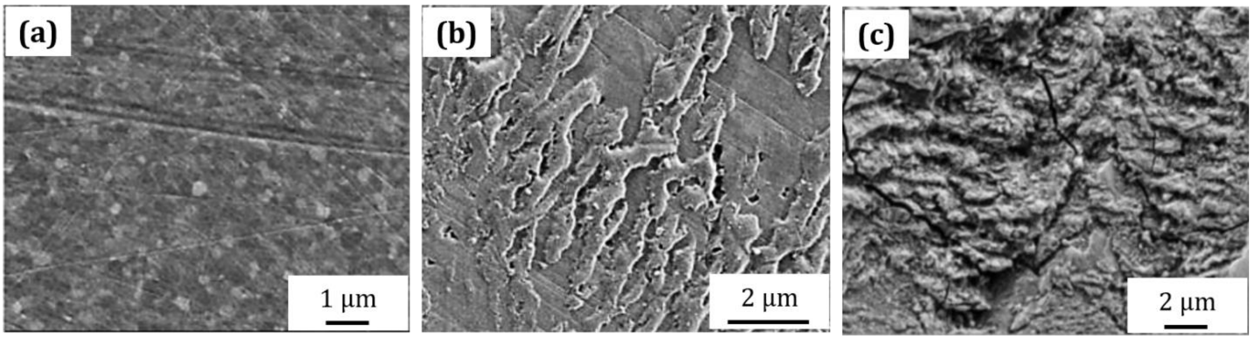

Fig. 25: Morphologies of the worn surfaces of transparent $MgAl_2O_4/Si_3N_4$ nanocomposite sintered at a) 1300°C b) 1350°C c) 1400°C [35] *passing from groves, to accumulated material and cracking of the worn surface due to an increased grain size of the matrix.*

Bodhak et al. [28] fabricated $MgAl_2O_4$ for an application in total hip arthroplasty and total knee arthroplasty, testing the fretting wear in the joint. Generally, a material's wear resistance is directly proportional to its hardness, i.e., the higher the hardness, the greater the wear resistance. However, there are several situations and materials where hardness does not correlate with wear [253–255]. To understand the wear mechanism, SEM images of spinel and AlON's worn tracks were observed by Bodhak et al. [28] in stimulated body fluid medium. Parallel arrays of fatigue cracks positioned perpendicular to the sliding direction were identified by high magnification investigation. Both transparent AlON and $MgAl_2O_4$ materials exhibited fatigue type wear. The small microcracks combined repeatedly to produce a longer crack. However, flaking and the production of wear debris increased in severity and became more noticeable on the AlON surface. It was previously assumed that the wear mechanism changed from abrasive and brittle fracture to fatigue wear as a result of the production of lubricating films on the surfaces during the wear testing. Another investigation on the wear of Al_2O_3-on-Al_2O_3 prosthetic hip joints [89] employed a multidirectional motion pin-on-disk device in distilled water and calf serum and found that moderate abrasion was the predominant wear mechanism. It was concluded that the alterations in surface roughness and method of preparation of TC contributed to different wear mechanisms and wear rates.

The material removal mechanism of TCs is directly affected by their densification degree. Transparent Y_2O_3 ceramic demonstrated that the powders processed with ball milling exhibit enhanced densification during SPS, possibly changing the material removal mechanism during wear [113]. There are two potential explanations: 1) The imperfections produced on the powder surfaces increase the electric current's impact during SPS processing. The milling process introduces large amounts of defects onto the powder surfaces. These defects enhance the conductivity of Y_2O_3 and subsequently improve sintering kinetics by an increase of electric current during SPS sintering. 2) The milling process decrease particle size, which be related to the current effect generated during SPS processing. Both these explanations demonstrate that the mechanism for material removal will be different for different wear tests.

An [186] fabricated transparent Lu_2O_3 ceramics by SPS using LiF as a sintering aid. The pressure and temperature of SPS varied between 20-100 MPa and 1000^oC-1600^oC, respectively, for 5-600 minutes. The fracture surface of the TC was intergranular below 1500^oC and transgranular above 1500^oC. A relationship has been established between the fracture toughness of TC and intergranular fracture occurring in TCs. An intergranular fracture occurs with coarse-grained microstructures, which is most likely caused by grain-boundary embrittlement. The embrittlement is produced by residual LiF, impurities, or residual stress [146]. It has been postulated that the weak boundaries of huge grains serve as critical surface defects in forming large grains. The fracture between grains that persists in coarse-grained microstructures lowers the overall strength of the material, which subsequently affects the tribological characteristic of the TC. Similarly, the fracture mechanism for transparent cBN changed from intergranular to transgranular when the sintering temperature is increased [205].

During rapid grain formation, the residual porosity in the sintered body is maintained, decreasing fracture toughness [205]. Thus, pore removal at the optimal sintering temperature is critical for creating a well-sintered material with superior mechanical properties. When fine powder and coarse powder are compared, it is discovered that fine powder has a greater driving force potential than coarse powder owing to the greater surface area of fine powder. For example, the surface area of fine powder with particles ranging from 0.5 to 1.2 µm is about ten times that of coarse powder with particles ranging from 8 to 12 µm [205]. These findings suggest that rapid grain formation occurs quickly in fine powders around the optimum sintering temperature. With decreasing particle sizes, controlling the sintering environment to create dense sintered bodies becomes increasingly tricky. Controlling the sintering temperature in fine-grained powders without causing grain formation is not straightforward, but affects the tribological characteristics.

5. Conclusions

This review aims to provide some meaningful guidelines for tribologists on the future study of tribological behaviour of transparent ceramics while identifying the wear mechanisms under particular wear conditions. Considering the extensive range of tribological applications, wear behaviour of TCs is extensively discussed in the present review and the following observations have been derived.

1. The microstructure of the TCs influences the mechanical, tribological and optical properties. There is a strong effect of microstructure, but the effect is not always be the same. Porosity affects all of the properties negatively, the presence of a secondary phase enhance mechanical (and tribological) properties, but has a deleterious effect on transparency. A solution come from a significant reduction of the grain size. The effect is stronger in the visible range compared to IR.

2. An increase in sintering temperature results in grain growth. In the case of non-cubic materials (e.g. alumina) or composite ceramics, this causes a reduction of transparency. The grain refinement of transparent ceramics is required to improve the mechanical behaviour, which further enhances the tribological performance of TCs. Therefore, optimum grain size is needed to achieve good tribological behaviour and good transparency. Fine-grained TCs are promising for both mechanical and optical properties and is successfully produced by SPS.

3. Fracture of TCs introduce median, radial, and lateral cracks, which result in the formation of debris. Besides the major microstructural factors affecting the wear of TC (porosity, phase composition, surface finishing), a notable influence is given by dislocations, stacking faults, nano twins, atomic plane torsion, atomic plane fracture, and atomic plane misalignment during scratching or erosion of TC.

4. Fracture toughness of TCs is highly affected by the microstructure of materials. Fracture toughness of TCs with maintaining their transparency is improved by strengthening and toughening mechanisms such as crack bridging, crack deflection, and crack branching, which absorbs some of the energy required to propagate fractures.

5. While scratching the TC the subsurface damage caused by the first nanoscratch modify the mechanical characteristics of the material, which in turn modify the tribological characteristics.

6. Abrasive particles develop during the wear process due to work hardening, phase changes, and the creation of a third body at the interface which are responsible for abrasive wear mechanism in the TCs. TCs operated under lubricated conditions are observed to experience fretting wear mechanism rather than abrasive wear mechanism.

6. Outlooks

For a comprehensive wear behaviour of TCs, microstructural characteristics must be included into modern wear models/theories in order to accurately estimate material removal under sliding or erosive situations. The majority of studies reported ambient temperature wear behaviour by estimating mechanical and microstructural characteristics of TCs, however, the influence of mechanical and microstructural properties on tribological applications must be taken into consideration at higher temperatures. Additionally, little research has been conducted on TCs to better understand their behaviour in low temperature tribological applications. A future research examining the influence of mechanical or microstructural properties at low temperatures should evaluate the possibility of using TCs for space or marine applications.

Additionally, the mechanics of deterioration under various wear circumstances must be completely understood. In light of the tribological performance, the parameters defining the microstructure (e.g. the amount of additive, the sintering method, sintering temperature, and sintering pressure) which are responsible for microstructural features must be studied in detail. Furthermore, studies must be expanded to better understand the performance of TC with high hardness and fracture toughness. The dependence of the ratio between hardness and fracture toughness, which is a prominent aspect of wear resistance of the ceramic materials, should be studied in case of TCs. Also the material removal mechanisms of TCs should be investigated in detail. While the majority of published research focuses on understanding the behaviour of transparency of TCs, one needs to examine the tribological potential of TCs for use in critical fields such as, explosive ordnance visors, aircraft, spacecraft, re-entry vehicles, electromagnetic windows, face shields, screens for smartphones and more. Lastly, and most importantly, the optical properties upon impact or scratch should be investigated in view of prolonged use.

Authors' Contributions:

Divyansh Mittal: Investigation, Resources, Data Curation, Writing - Original Draft

Jan Hostaša: Validation, Resources, Data Curation, Writing - Review & Editing, Visualization

Laura Silvestroni: Visualization, Resources, Data Curation, Writing - Review & Editing

Laura Esposito: Resources, Data Curation, Writing - Review & Editing

Anita Mohan: Formal analysis, Writing - Review & Editing

Rajiv Kumar: Formal analysis, Data Curation, Writing - Review & Editing

Sandan Kumar Sharma: Conceptualization, Methodology, Visualization, Validation, Resources, Data Curation, Writing - Review & Editing, Supervision.

Authors' Biography:

Mr. Divyansh Mittal is a Ph.D. (pursuing) scholar in the Metallurgical and Materials Engineering Department, PEC (Deemed to be University), Chandigarh, India. His research interests include Tribological behaviour of ceramic materials, Abrasive Jet Machining, and Mathematical Modelling.

Dr. Jan Hostaša is a researcher with a permanent position at the CNR ISTEC, Faenza, Italy. In his research, he focuses mostly on the production of transparent ceramics for optics, lasers, detectors and protection, and the relations between process, microstructure and the properties of these materials. Dr. Hostaša has been working significantly also on the shaping of transparent functional ceramics for optical applications and the fabrication of composite and gradient structures. He is one of the founders of a spin-off of the CNR, Zenit Smart Polycrystals.

Dr. Laura Silvestroni is a researcher at the Institute of Science and Technology for Ceramics. Her research interest includes the design, production and characterization of structural ceramics, in particular materials for harsh environments. She has published over 100 articles published in scientific journals as first author or co-author. Also, she is an Editor of the Journal of the European Ceramic Society. She is responsible for projects funded by government agencies and industries.

Dr. Laura Esposito is a researcher with experience in advanced ceramic materials gained in 30 years of work in research centers in Italy and abroad, in both the public and private sectors. She was National Expert Seconded to the European Commission in Brussels for four years, with expertise in the field of European research funding programs. Her field of expertise at ISTEC is transparent ceramics for optical applications.

Dr. Anita Mohan received her PhD from Dept. of Applied Physics, Indian Institute of Technology (BHU), Varanasi, India. Currently, she is working as Associate Professor at Department of Physics, IIT-BHU. Her research interest includes solar and space physics, physics and diagnostics of solar system plasmas: EUV and X-Ray emission, and synthesis and characterization of composites.

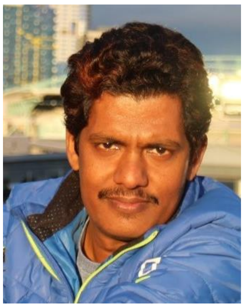

Dr. Rajiv Kumar received his Ph.D. degree from Indian Institute of Technology Bombay, India and Monash University, Australia. Currently, he is working in the Department of Metallurgical and Materials Engineering at Punjab Engineering College, Chandigarh, as an assistant professor. His research interests focus on powder metallurgy, high temperature oxidation, corrosion, bulk nanocrystalline materials, high entropy alloys, and mechanical behaviour of metals and alloys.

Dr. Sandan Kumar Sharma received his Ph.D. degree from Indian Institute of Technology Roorkee, India. Then he did his postdoctoral research in the Laboratory for Tribology and Surface Nanotechnology (TINT) at the University of Ljubljana, Slovenia. Currently, he is working in the Department of Metallurgical and Materials Engineering at Punjab Engineering College, Chandigarh, as an assistant professor. His research interests focus on friction and wear behaviour of materials, and the structure-property relation of advanced structural ceramics for extreme tribological applications.

References

1. Coble, R.L. Transparent Alumina and Method of Preparation. 1962.

2. Gatti, A.; Noone, J. Feasibility study for producing transparent spinel. AMMRC-CR 1970, 70–80.

3. Ballard Jr, C.P. Transparent ceramic armor. Sandia Labs., Albuquerque, NM, USA 1978, doi:EY-76-C-04-0789.

4. Ikesue, A.; Kinoshita, T.; Kamata, K.; Yoshida, K. Fabrication and Optical Properties of High- Performance Polycrystalline Nd:YAG Ceramics for Solid- State Lasers. J. Am. Ceram. Soc. 1995, 78, 1033–1040, doi:10.1111/j.1151-2916.1995.tb08433.x.

5. Wei, G.C. Transparent ceramic lamp envelope materials. J. Phys. D. Appl. Phys. 2005, 38, 3057–3065, doi:10.1088/0022-3727/38/17/S07.

6. Ikesue, A.; Aung, Y.L.; Lupei, V. Ceramic Lasers. J. Phys. D. Appl. Phys. 2013, 28, 3057–3065.

7. Krell, A.; Klimke, J.; Hutzler, T. Advanced spinel and sub-micrometer Al_2O_3 for transparent armour applications. J. Eur. Ceram. Soc. 2009, 29, 275–281, doi:10.1016/j.jeurceramsoc.2008.03.024.

8. Harris, D.C. Durable 3–5 μm transmitting infrared window materials. Infrared Phys. Technol. 1998, 39, 185–201, doi:10.1016/S1350-4495(98)00006-1.

9. Wang, S.F.; Zhang, J.; Luo, D.W.; Gu, F.; Tang, D.Y.; Dong, Z.L.; Tan, G.E.B.; Que, W.X.; Zhang, T.S.; Li, S.; et al. Transparent ceramics: Processing, materials and applications. Prog. Solid State Chem. 2013, 41, 20–54, doi:10.1016/j.progsolidstchem.2012.12.002.

10. Krell, A.; Bales, A. Grain size-Dependent hardness of transparent magnesium aluminate spinel. Int. J. Appl. Ceram. Technol. 2011, 8, 1108–1114, doi:10.1111/j.1744-7402.2010.02583.x.

11. Goldstein, A. Correlation between $MgAl_2O_4$-spinel structure , processing factors and functional properties of transparent parts (progress review). J. Eur. Ceram. Soc. 2012, 32, 2869–2886, doi:10.1016/j.jeurceramsoc.2012.02.051.

12. Sands, J.M.; Fountzoulas, C.G.; Gilde, G.A.; Patel, P.J. Modelling transparent ceramics to improve military armour. J. Eur. Ceram. Soc. 2009, 29, 261–266, doi:10.1016/j.jeurceramsoc.2008.03.010.

13. Straßburger, E. Ballistic testing of transparent armour ceramics. J. Eur. Ceram. Soc. 2009, 29, 267–273, doi:10.1016/j.jeurceramsoc.2008.03.049.

14. Klement, R.; Rolc, S.; Mikulikova, R.; Krestan, J. Transparent armour materials. J. Eur. Ceram. Soc. 2008, 28, 1091–1095, doi:10.1016/J.JEURCERAMSOC.2007.09.036.

15. Lempicki, A.; Brecher, C.; Szupryczynski, P.; Lingertat, H.; Nagarkar, V. V.; Tipnis, S. V.; Miller, S.R. A new lutetia-based ceramic scintillator for X-ray imaging. Nucl. Instruments Methods Phys. Res. Sect. A Accel. Spectrometers, Detect. Assoc. Equip. 2002, 488, 579–590, doi:10.1016/S0168-9002(02)00556-9.

16. Wei, N.; Lu, T.; Li, F.; Zhang, W.; Ma, B.; Lu, Z.; Qi, J. Transparent Ce:$Y_3Al_5O_{12}$ ceramic phosphors for white light-emitting diodes. Appl. Phys. Lett. 2012, 101, doi:10.1063/1.4742896.

17. Nishiura, S.; Tanabe, S.; Fujioka, K.; Fujimoto, Y. Properties of transparent Ce:YAG ceramic phosphors for white LED. Opt. Mater. (Amst). 2011, 33, 688–691, doi:10.1016/J.OPTMAT.2010.06.005.

18. Hinklin, T.R.; Rand, S.C.; Laine, R.M. Transparent, polycrystalline upconverting nanoceramics: Towards 3-D displays. Adv. Mater. 2008, 20, 1270–1273, doi:10.1002/adma.200701235.

19. Stanciu, G.; Stanciu, C.A.; Brandus, C.A.; Voicu, F.M.; Dascalu, T. Laser gain transparent ceramics media. Opt. InfoBase Conf. Pap. 2017, Part F67-L, 10–12, doi:10.1364/LIC.2017.LWA5.5.

20. Jones, I.K.; Seeley, Z.M.; Cherepy, N.J.; Duoss, E.B.; Payne, S.A. Direct ink write fabrication of transparent ceramic gain media. Opt. Mater. (Amst). 2018, 75, 19–25, doi:10.1016/j.optmat.2017.10.005.

21. Observatories across the electromagnetic spectrum available online: https://imagine.gsfc.nasa.gov/science/toolbox/emspectrum_observatories1.html (accessed on Jan 15, 2022).

22. Salem, J.A. Transparent armor ceramics as spacecraft windows. J. Am. Ceram. Soc. 2013, 96, 281–289, doi:10.1111/jace.12089.

23. Krell, A.; Hutzler, T.; Klimke, J. Transmission physics and consequences for materials selection, manufacturing, and applications. J. Eur. Ceram. Soc. 2009, 29, 207–221, doi:10.1016/j.jeurceramsoc.2008.03.025.

24. Xiao, Z.; Yu, S.; Li, Y.; Ruan, S.; Kong, L.B.; Huang, Q.; Huang, Z.; Zhou, K.; Su, H.; Yao, Z.; et al. Materials development and potential applications of transparent ceramics: A review. Mater. Sci. Eng. R Reports 2020, 139, 100518, doi:10.1016/j.mser.2019.100518.

25. Information on https://ntrs.nasa.gov/citations/20170005664.

26. Information on https://www.marketsandmarkets.com/Market-Reports/transparent-ceramic-market-78249828.html.

27. Goldstein, A.; Krell, A.; Burshtein, Z. Transparent Ceramics; Wiley, 2020; ISBN 9781119429494.

28. Bodhak, S.; Balla, V.K.; Bose, S.; Bandyopadhyay, A.; Kashalikar, U.; Jha, S.K.; Sastri, S. In vitro biological and tribological properties of transparent magnesium aluminate (Spinel) and aluminum oxynitride (ALON). J. Mater. Sci. Mater. Med. 2011, 22, 1511–1519, doi:10.1007/s10856-011-4332-5.

29. Medvedovsk, E. Ceramic Armor and Armor Systems; The American Ceramic Society, 2003; ISBN 1574980505.

30. Kerwienb, H.; Arsenal, P. Evaluation of ALON for cannon window application. Wind. Dome Technol. Mater. 1999, 3705.

31. Patel, P.J.; Gilde, G.A.; Dehmer, P.G.; McCauley, J.W. Transparent ceramics for armor and EM window applications. Inorg. Opt. Mater. II 2000, 4102, 1–14, doi:10.1117/12.405270.

32. Boulesteix, R.; Maître, A.; Baumard, J.-F.; Rabinovitch, Y.; Reynaud, F. Light scattering by pores in transparent Nd:YAG ceramics for lasers: correlations between microstructure and optical properties. Opt. Express 2010, 18, 14992, doi:10.1364/oe.18.014992.

33. Hříbalová, S.; Pabst, W. Modeling light scattering by spherical pores for calculating the transmittance of transparent ceramics – All you need to know. J. ofthe Eur. Ceram. Soc. 2020, 41, 2169–2192, doi:10.1016/j.jeurceramsoc.2020.11.046.

34. Dericioglu, A.F.; Kagawa, Y. Effects of grain boundary microcracking on the light transmittance of sintered transparent MgAl2O4. J. Eur. Ceram. Soc. 2003, 23, 951–959, doi:10.1016/S0955-2219(02)00205-4.

35. Benaissa, S.; Hamidouche, M.; Kolli, M.; Bonnefont, G.; Fantozzi, G. Characterization of nanostructured MgAl2O4 ceramics fabricated by spark plasma sintering. Ceram. Int. 2016, 42, 8839–8846, doi:10.1016/j.ceramint.2016.02.130.

36. Joshi, B.; Fu, Z.; Niihara, K.; Lee, S.W. Fabrication of translucent boron nitride dispersed polycrystalline silicon nitride ceramics. IOP Conf. Ser. Mater. Sci. Eng. 2011, 20, doi:10.1088/1757-899X/20/1/012014.

37. Joshi, B.; Fu, Z.; Niihara, K.; Lee, S.W. Optical, mechanical and tribological properties of boronnitride dispersed silicon nitride Ceramics. Korean J. Mater. Res. 2010, 20, 444–449, doi:10.3740/MRSK.2010.20.8.444.

38. Tingting, W.U.; Jian, Z.; Bolin, W.U.; Wenjie, L.I. Effect of La_2O_3 content on wear resistance of alumina ceramics. J. Rare Earths 2016, 34, 288–294, doi:10.1016/S1002-0721(16)60027-3.

39. Krell, A.; Blank, P.; Ma, H.; Hutzler, T.; Bruggen, M.P.B. Van; Apetz, R. Transparent Sintered Corundum with High Hardness and Strength. J. Am. Ceram. Soc. 2003, 86, 12–18.

40. Krell, A.; Klimke, J. Effects of the homogeneity of particle coordination on solid-state sintering of transparent alumina. J. Am. Ceram. Soc. 2006, 89, 1985–1992, doi:10.1111/j.1551-2916.2006.00985.x.

41. Li, K.; Shapiro, Y.; Li, J.C.M. Scratch test of soda-lime glass. Acta Mater. 1998, 46, 5569–5578, doi:10.1016/S1359-6454(98)00163-3.

42. Bull, S.J. Failure modes in scratch adhesion testing. Surf. Coatings Technol. 1991, 50, 25–32, doi:10.1016/0257-8972(91)90188-3.

43. Sato, Y.; Arzakantsyan, M.; Akiyama, J.; Taira, T. Anisotropic Yb:FAP laser ceramics by micro-domain control. Opt. Mater. Express 2014, 4, 2006, doi:10.1364/ome.4.002006.

44. Nishiyama, N.; Ishikawa, R.; Ohfuji, H.; Marquardt, H.; Kurnosov, A.; Taniguchi, T.; Kim, B.N.; Yoshida, H.; Masuno, A.; Bednarcik, J.; et al. Transparent polycrystzalline cubic silicon nitride. Sci. Rep. 2017, 7, 1–8, doi:10.1038/srep44755.

45. Stuer, M.; Bowen, P.; Cantoni, M.; Pecharroman, C.; Zhao, Z. Nanopore characterization and optical modeling of transparent polycrystalline alumina. Adv. Funct. Mater. 2012, 22, 2303–2309, doi:10.1002/adfm.201200123.

46. Pabst, W.; Hostaša, J. A closed-form expression approximating the mie solution for the real-in-line transmission of ceramics with spherical inclusions or pores. Ceram. - Silikaty 2013, 57, 151–161.

47. Lakshmanan, A. Sintering of ceramics– New Emerging Techniques; InTech, 2012; ISBN 9789535100171.

48. Nassajpour-Esfahani, A.H.; Emadi, R.; Alhaji, A.; Bahrami, A.; Haftbaradaran-Esfahani, M.R. Towards high strength $MgAl_2O_4/Si_3N_4$ transparent nanocomposite, using spark plasma sintering. J. Alloys Compd. 2020, 830, 154588, doi:10.1016/j.jallcom.2020.154588.

49. Huang, C.B.; Lu, T.C.; Lin, L. Bin; Lei, M.Y.; Huang, C.X. A Study on Toughening and Strengthening of Mg-Al Spinel Transparent Ceramics. Key Eng. Mater. 2007, 336–338, 1207–1210, doi:10.4028/www.scientific.net/kem.336-338.1207.

50. Awaji, H.; Choi, S.M.; Yagi, E. Mechanisms of toughening and strengthening in ceramic-based nanocomposites. Mech. Mater. 2002, 34, 411–422, doi:10.1016/S0167-6636(02)00129-1.

51. Sheikh, H.; Loghman-Estarki, M.R.; Sharifi, E.M.; Alhaji, A.; Shakeri, J. Toughening of MgAl2O4 spinel/ Si_3N_4 nanocomposite fabricated by spark plasma sintering. Ceram. Int. 2018, 44, 18235–18242, doi:10.1016/j.ceramint.2018.07.033.

52. Mizuta, H.; Oda, K.; Shibasaki, Y.; Maeda, M.; Machida, M.; Ohshima, K. Preparation of High- Strength and Translucent Alumina by Hot Isostatic Pressing. J. Am. Ceram. Soc. 1992, 75, 469–473, doi:10.1111/j.1151-2916.1992.tb08203.x.

53. Apetz, R.; Van Bruggen, M.P.B. Transparent alumina: A light-scattering model. J. Am. Ceram. Soc. 2003, 86, 480–486, doi:10.1111/j.1151-2916.2003.tb03325.x.

54. Borrero-López, O.; Ortiz, A.L.; Gledhill, A.D.; Guiberteau, F.; Mroz, T.; Goldman, L.M.; Padture, N.P. Microstructural effects on the sliding wear of transparent magnesium-aluminate spinel. J. Eur. Ceram. Soc. 2012, 32, 3143–3149, doi:10.1016/j.jeurceramsoc.2012.04.002.

55. Grasso, S.; Hu, C.; Maizza, G.; Kim, B.-N.; Sakka, Y. Effects of Pressure Application Method on Transparency of Spark Plasma Sintered Alumina. 2011, 1409, 1405–1409, doi:10.1111/j.1551-2916.2010.04274.x.

56. Roussel, N.; Lallemant, L.; Durand, B.; Guillemet, S.; Ching, J.C.; Fantozzi, G.; Garnier, V.; Bonnefont, G. Effects of the nature of the doping salt and of the thermal pre-treatment and sintering temperature on Spark Plasma Sintering of transparent alumina. Ceram. Int. 2011, 37, 3565–3573, doi:10.1016/j.ceramint.2011.05.152.

57. Huang, Z.; Deng, J.; Wang, H.; Zhang, Y.; Duan, J.; Tang, Z.; Yang, Y.; He, D.; Qi, J.; Lu, T. A new method for the preparation of transparent Y_2O_3 nanocrystalline ceramic with an average grain size of 20 nm. Scr. Mater. 2020, 182, 57–61, doi:10.1016/j.scriptamat.2020.02.044.

58. Goldstein, A.; Krell, A.; Burshtein, Z. Transparent Ceramics Wikipedia. Transparent Ceram. 2020, 1–16, doi:10.1002/9781119429524.

59. Bergmann, C.P.; Alegre, P. Transparent Ceramics; 2015; ISBN 9783319189550.

60. Esposito, L.; Piancastelli, A.; Miceli, P.; Martelli, S. A thermodynamic approach to obtaining transparent spinel ($MgAl_2O_4$) by hot pressing. J. Eur. Ceram. Soc. 2015, 35, 651–661, doi:10.1016/j.jeurceramsoc.2014.09.005.

61. Tanaka, S.; Itatani, K.; Uchida, H.; Aizawa, M. The effect of rare-earth oxide addition on the hot-pressing of magnesium silicon nitride. 2002, 22, 777–783.

62. A, Q.G.; Xikun, L.; Tai, Q.; Haitao, Z. Application of Rare Earths in Advanced Ceramic Materials. 2007, 25, 281–286.

63. Nishiyama, N.; Taniguchi, T.; Ohfuji, H.; Yoshida, K.; Wakai, F.; Kim, B.N.; Yoshida, H.; Higo, Y.; Holzheid, A.; Beermann, O.; et al. Transparent nanocrystalline bulk alumina obtained at 7.7 GPa and 800 ° C. Scr. Mater. 2013, 69, 362–365, doi:10.1016/j.scriptamat.2013.05.017.

64. Grasso, S.; Yoshida, H.; Porwal, H.; Sakka, Y.; Reece, M. Highly transparent alpha alumina obtained by low cost high pressure SPS. Ceram. Int. 2013, 39, 3243–3248, doi:10.1016/j.ceramint.2012.10.012.

65. Joshi, B.; Fu, Z.; Niihara, K.; Lee, S.W. Optical, mechanical and tribological properties of Y_2O_3, Er_2O_3 and Nd_2O_3 doped polycrystalline silicon nitride ceramics. IOP Conf. Ser. Mater. Sci. Eng. 2011, 18, 3–7, doi:10.1088/1757-899X/18/8/082020.

66. von Helden, S.; Malzbender, J.; Krüger, M. Mechanical properties, wear resistance and surface damage of glasses and $MgAl_2O_4$ spinel ceramic after abrasion and scratch exposure. Ceram. Int. 2019, 45, 10765–10775, doi:10.1016/j.ceramint.2019.02.150.

67. Grujicic, M.; Bell, W.C.; Pandurangan, B. Design and material selection guidelines and strategies for transparent armor systems. Mater. Des. 2012, 34, 808–819, doi:10.1016/j.matdes.2011.07.007.

68. Mccauley, J.W.; Strassburger, E.; Patel, P.; Paliwal, B.; Ramesh, K.T. Experimental Observations on Dynamic Response of Selected Transparent Armor Materials. Exp. Mech. 2013, 53, 3–29, doi:10.1007/s11340-012-9658-5.

69. Strassburger, E. V isualization of Impact Damage in Ceramics Using the Edge-On Impact Technique. Int. J. Appl. Ceram. Technol. 2004, 1, 35–42.

70. Senf, H.; Strassburger, E.; Rothenhausler, H. Stress wave induced damage and fracture in impacted glasses. Le J. Phys. IV 1994, 4, 741.

71. Strassburger, E.; Patel, P.; Mccauley, J.W.; Templeton, D.W. High-speed photographic study of wave and impact damage in fused silica and using edge-on impact (EOI) method. 2006, 1503–1506.

72. Lyberis, A.; Patriarche, G.; Gredin, P.; Vivien, D.; Mortier, M. Origin of light scattering in ytterbium doped calcium fluoride transparent ceramic for high power lasers. J. Eur. Ceram. Soc. 2011, 31, 1619–1630, doi:10.1016/J.JEURCERAMSOC.2011.02.038.

73. Sharma, S.K.; Kumar, B.V.M.; Kim, Y.W. Tribological behavior of silicon carbide ceramics - A review. J. Korean Ceram. Soc. 2016, 53, 581–596, doi:10.4191/kcers.2016.53.6.581.

74. Jung, W.K.; Ma, H.J.; Kim, H.N.; Kim, D.K. Transparent ceramics for visible/IR windows: Processing, materials and characterization. Korean J. Mater. Res. 2018, 28, 551–563, doi:10.3740/MRSK.2018.28.10.551.

75. Drdlik, D.; Drdlikova, K.; Hadraba, H.; Maca, K. Optical, mechanical and fractographic response of transparent alumina ceramics on erbium doping. J. Eur. Ceram. Soc. 2017, 37, 4265–4270, doi:10.1016/j.jeurceramsoc.2017.02.043.

76. Pietruszka, R.; Witkowski, B.S.; Zimowski, S.; Stapinski, T.; Godlewski, M. Tribological study of hafnium dioxide and aluminium oxide films grown by atomic layer deposition on glass substrate. Thin Solid Films 2020, 709, 138191, doi:10.1016/j.tsf.2020.138191.

77. Goldman, L.M.; Twedt, R.; Balasubramanian, S.; Sastri, S. AlON Optical Ceramic Transparencies for Window , Dome and Transparent Armor Applications. Wind. Dome Technol. Mater. 2011, 8016, 1–14, doi:10.1117/12.886122.

78. Guzik, M.; Pejchal, J.; Yoshikawa, A.; Ito, A.; Goto, T.; Siczek, M.; Lis, T.; Boulon, G. Structural investigations of Lu_2O_3 as single crystal and polycrystalline transparent ceramic. Cryst. Growth Des. 2014, 14, 3327–3334, doi:10.1021/cg500225v.

79. Lu, O.; Mcmillen, C.; Thompson, D.; Tritt, T.; Kolis, J. Hydrothermal Single-Crystal Growth of Lu_2O_3 and Lanthanide-Doped Lu_2O_3. 2011, 4386–4391.

80. Taniguchi, T.; Yamaoka, S. Spontaneous nucleation of cubic boron nitride single crystal by temperature gradient method under high pressure. 2001, 222, 549–557.

81. Fukabori, A.; Yanagida, T.; Pejchal, J.; Maeo, S.; Yokota, Y.; Yoshikawa, A.; Ikegami, T.; Moretti, F.; Kamada, K. Optical and scintillation characteristics of Y_2O_3 transparent ceramic. J. Appl. Phys. 2010, 107, doi:10.1063/1.3330407.

82. Hou, X.; Zhou, S.; Jia, T.; Lin, H.; Teng, H. Investigation of up-conversion luminescence properties of RE/Yb co-doped Y2O3 transparent ceramic (RE=Er, Ho, Pr, and Tm). Phys. B Condens. Matter 2011, 406, 3931–3937, doi:10.1016/j.physb.2010.10.090.

83. Nishiyama, N.; Ishikawa, R.; Ohfuji, H.; Marquardt, H.; Kurnosov, A.; Taniguchi, T.; Kim, B.N.; Yoshida, H.; Masuno, A.; Bednarcik, J.; et al. Transparent polycrystalline cubic silicon nitride. Sci. Rep. 2017, 7, 1–8, doi:10.1038/srep44755.

84. Mandal, H.; Bressiani, A.H.; Mandal, H. New developments in alpha-SiAlON ceramics. J. Eur. Ceram. Soc. 1999, 19, 2349–2357.

85. Su, X.; Wang, P.; Chen, W.; Cheng, Y.; Yan, D. Infrared transmission of hot-pressed Y- and Dy-α-sialon ceramics. Mater. Lett. 2004, 58, 1985–1988, doi:10.1016/j.matlet.2003.12.020.

86. Xiong, Y.; Fu, Z.; Wang, H.; Wang, W.; Zhang, J.; Zhang, Q.; Lee, S.W.; Niihara, K. Translucent Mg-α-sialon ceramics prepared by spark plasma sintering. J. Am. Ceram. Soc. 2007, 90, 1647–1649, doi:10.1111/j.1551-2916.2007.01615.x.

87. Goldman, L.M.; Hartnett, T.M.; Wahi, J.M.; Ondercin, R.J.; Olson, K. Recent advances in Aluminium Oxynitride (AlON) optical ceramic. Wind. Dome Technol. Mater. 2001, 4375, 71–78.

88. Mroz, T.; Goldman, L.M.; Gledhill, A.D.; Li, D.; Padture, N.P. Nanostructured , Infrared-Transparent Magnesium- Aluminate Spinel with Superior Mechanical Properties. Int. J. Appl. Ceram. Technol. 2012, 9, 83–90, doi:10.1111/j.1744-7402.2011.02629.x.

89. Saikko, V.; Keränen, J. Wear simulation of alumina-on-alumina prosthetic hip joints using a multidirectional motion pin-on-disk device. J. Am. Ceram. Soc. 2002, 85, 2785–2791, doi:10.1111/j.1151-2916.2002.tb00529.x.

90. Sung, R.J.; Kim, S.H.; Kusunose, T.; Nakayama, T.; Sekino, T. Mechanical and Wear Properties of Silicon Nitride added with AlN. Mater. Sci. Forum Trans Tech Publ. Ltd 2005, 487, 209–212, doi:10.4028/www.scientific.net/MSF.486-487.209.

91. Kim, J.H.; Venkata Manoj Kumar, B.; Hong, S.H.; Kim, H.D. Fabrication of silicon nitride nanoceramics and their tribological properties. J. Am. Ceram. Soc. 2010, 93, 1461–1466, doi:10.1111/j.1551-2916.2010.03614.x.

92. Li, X.; Xu, Y.; Mao, X.; Zhu, Q.; Xie, J.; Feng, M.; Jiang, B.; Zhang, L. Investigation of optical, mechanical, and thermal properties of ZrO_2-doped Y_2O_3 transparent ceramics fabricated by HIP. Ceram. Int. 2017, 44, 1362–1369, doi:10.1016/j.ceramint.2017.08.204.

93. Zhu, L.; Park, Y.; Gan, L.; Go, S.; Kim, H.; Kim, J.; Ko, J. Fabrication and characterization of highly transparent Er:Y_2O_3 ceramics with ZrO_2 and La_2O_3 additives. Ceram. Int. 2017, 43, 13127–13132, doi:10.1016/j.ceramint.2017.07.004.

94. Korkmaz, E.; Sahin, F. Fabrication of Transparent Yttria Ceramics by Spark Plasma Sintering Fabrication of Transparent Yttria Ceramics by Spark Plasma Sintering. ACTA Phys. Pol. A 2020, 8–11, doi:10.12693/APhysPolA.131.460.

95. Liu, L.; Morita, K.; Suzuki, T.S.; Kim, B.-N. Effect of the Heating Rate on the Spark-Plasma-Sintering (SPS) of Transparent Y_2O_3 Ceramics: Microstructural Evolution, Mechanical and Optical Properties. Ceramics 2021, 4, 56–69, doi:10.3390/ceramics4010006.

96. Composition, A.; Al, M.; Sutorik, A.C.; Gilde, G.; Swab, J.J.; Cooper, C.; Gamble, R.; Shanholtz, E. Transparent Solid Solution Magnesium Aluminate Spinel Polycrystalline Ceramic with the Alumina-Rich Composition MgO·1.2Al2O3. J. Am. Ceram. Soc. 2012, 643, 636–643, doi:10.1111/j.1551-2916.2011.04798.x.

97. Dericioglu, A.F.; Boccaccini, A.R.; Dlouhy, I.; Kagawa, Y. Effect of Chemical Composition on the Optical Properties and Fracture Toughness of Transparent Magnesium Aluminate Spinel Ceramics. Mater. Trans. 2005, 46, 996–1003.

98. Ramisetty, M.; Sastri, S.; Kashalikar, U.; Goldman, L.M.; Nag, N. Transparent polycrystalline cubic spinels protect and defend. Am. Ceram. Soc. Bull. 2013, 92.

99. Yang, W.; Hojo, J.; Enomoto, N.; Tanaka, Y.; Inada, M. Influence of Sintering Aid on the Translucency of Spark Plasma-Sintered Silicon Nitride Ceramics. J. Am. Ceram. Soc. 2013, 96, 2556–2561, doi:10.1111/jace.12370.

100. Joshi, B.; Fu, Z.; Niihara, K. Fabrication of Translucent Boron Nitride Dispersed Polycristalline Silicon Nitride Ceramics. IOP Conf. Ser. Mater. Sci. Eng. 2011, 20, 1–6, doi:10.1088/1757-899X/20/1/012014.

101. Su, X.; Wang, P.; Chen, W.; Zhu, B.; Cheng, Y.; Yan, D. Translucent alpha-Sialon Ceramics by Hot Pressing. J. Am. Ceram. Soc. 2010, 32, 730–732.

102. Kaminskii, A.A.; Akchurin, M.S.; Becker, P.; Ueda, K.; Bohat, L. Mechanical and optical properties of Lu_2O_3 host-ceramics for Ln^{3+} lasants. Laser Phys. Lett. 2008, 5, 300–303, doi:10.1002/lapl.200710128.

103. Munro, R.G. Elastic moduli data for polycrystalline ceramics. NISTIR, Gaithersburg, Maryl. 2002, 20899, 6853.

104. Speyer, R.F.; Sayir, A. Sintering, thermal conductivity, optical and lasing properties of doped-Lu2O3 fiberous transparent ceramics; 2014;

105. Pavlik, A.; Ushakov, S. V.; Navrotsky, A.; Benmore, C.J.; Weber, R.J.K. Structure and thermal expansion of Lu_2O_3 and Yb_2O_3 to the melting temperatures. J. Nucl. Mater. 2017, 495, 1–25.

106. Liang, A.; Liu, Y.; Shi, L.; Lei, L.; Zhang, F.; Hu, Q.; He, D. Melting temperature of diamond and cubic boron nitride at 15 gigapascals. Phys. Rev. Res. 2019, 1, 033090, doi:10.1103/PHYSREVRESEARCH.1.033090/FIGURES/17/MEDIUM.

107. Soltani, A.; Talbi, A.; Mortetb, V.; Benmoussa, A.; Zhang, W.J.; Gerbedoen, J.C.; De Jaeger, J.C.; Gokarna, A.; Haenen, K.; Wagner, P. Diamond and cubic boron nitride: Properties, growth and applications. AIP Conf. Proc. 2010, 1292, 191–196, doi:10.1063/1.3518293.

108. Akaishi, M.; Satoh, T.; Ishii, M.; Taniguchi, T. Synthesis of translucent sintered cubic boron nitride. J. Mater. Sci. Lett. 1993, 12, 1883–1885.

109. Tian, Y.; Xu, B.; Yu, D.; Ma, Y.; Wang, Y.; Jiang, Y.; Hu, W.; Tang, C.; Gao, Y. Ultrahard nanotwinned cubic boron nitride. Nature 2013, 493, 385–388, doi:10.1038/nature11728.

110. Sei, H. Effect of small amounts of hydrochloric acid on the synthesis of translucent sintered cubic BN. Diam. Relat. Mater. 1993, 2, 1160–1163.

111. Ghanizadeh, S.; Grasso, S.; Ramanujam, P.; Vaidhyanathan, B.; Binner, J.; Brown, P.; Goldwasser, J. Improved transparency and hardness in α-alumina ceramics fabricated by high-pressure SPS of nanopowders. Ceram. Int. 2017, 43, 275–281, doi:10.1016/j.ceramint.2016.09.150.

112. Chen, D.; Jordan, H.; Gell, M. Pressureless sintering of translucent MgO ceramics. Scr. Mater. 2008, 59, 757–759, doi:10.1016/j.scriptamat.2008.06.007.

113. Liu, L.; Morita, K.; Suzuki, T.S. Effect of the Heating Rate on the Spark-Plasma-Sintering (SPS) of Transparent Y_2O_3 Ceramics : Microstructural Evolution, Mechanical and Optical Properties. Ceramics 2021, 56–69.

114. Fleischman, Z.D.; Blair, V.L.; Ku, N.; Merkle, L.D. Dual-phase Er:Y_2O_3/MgO nanocomposites for mid-Infrared solid state lasers. https://doi.org/10.1117/12.2311470 2018, 10637, 116–126, doi:10.1117/12.2311470.

115. Wang, S.F.; Zhang, J.; Luo, D.W.; Gu, F.; Tang, D.Y.; Dong, Z.L.; Tan, G.E.B.; Que, W.X.; Zhang, T.S.; Li, S.; et al. Transparent ceramics: Processing, materials and applications. Prog. Solid State Chem. 2013, 41, 20–54, doi:10.1016/j.progsolidstchem.2012.12.002.

116. Goldstein, A.; Goldenberg, A.; Hefetz, M. Influence of powder type on the densification of transparent MgAl2O4 spinel. Ceram. Mater. Components Energy Environ. Appl. 2009, 579–84.

117. Merac, M.R. du; Kleebe, H.-J.; Muller, M.M.; Reimanis, I.E. Fifty Years of Research and Development Coming to Fruition: Unraveling the Complex Interactions during Processing of Transparent Magnesium Aluminate ($MgAl_2O_4$) Spinel. J. Am. Ceram. Soc. 2013, 96, 3341–3365, doi:10.1111/jace.12637.

118. Balabanov, S.S.; Yavetskiy, R.P.; Belyaev, A. V; Gavrishchuk, E.M.; Drobotenko, V. V Fabrication of transparent $MgAl_2O_4$ ceramics by hot-pressing of sol-gel-derived nanopowders. Ceram. Int. 2015, 41, 13366–13371, doi:10.1016/j.ceramint.2015.07.123.

119. Esposito, L.; Piancastelli, A.; Martelli, S. Production and characterization of transparent $MgAl_2O_4$ prepared by hot pressing. J. Eur. Ceram. Soc. 2013, 33, 737–747, doi:10.1016/j.jeurceramsoc.2012.10.013.

120. Hostaša, J.; Esposito, L.; Alderighi, D.; Pirri, A. Preparation and characterization of Yb-doped YAG ceramics. Opt. Mater. (Amst). 2013, 35, 798–803, doi:10.1016/j.optmat.2012.05.028.

121. Hostaša, J.; Biasini, V.; Piancastelli, A.; Vannini, M.; Toci, G. Layered Yb:YAG ceramics produced by two different methods: processing, characterization, and comparison. Opt. Eng. 2016, 55, 087104, doi:10.1117/1.oe.55.8.087104.

122. Trunec, M.; Kastyl, J.; Stastny, P.; Hildebrandt, S. Processing of large and complex-shaped fine-grained alumina bodies with high transparency. J. Eur. Ceram. Soc. 2021, 41, 2016–2022, doi:10.1016/j.jeurceramsoc.2020.10.065.

123. Feng, Z.; Qi, J.; Lu, T. Highly-transparent AlON ceramic fabricated by tape-casting and pressureless sintering method. J. Eur. Ceram. Soc. 2020, 40, 1168–1173, doi:10.1016/j.jeurceramsoc.2019.11.065.

124. Boulesteix, R.; Goldstein, A.; Perrière, C.; Maître, A.; Katz, M.; Coureau, C.; Sallé, C. Transparent ceramics green-microstructure optimization by pressure slip-casting: Cases of YAG and MgAl2O4. J. Eur. Ceram. Soc. 2021, 41, 2085–2095, doi:10.1016/j.jeurceramsoc.2020.11.003.

125. Hostaša, J.; Schwentenwein, M.; Toci, G.; Esposito, L.; Brouczek, D.; Piancastelli, A.; Pirri, A.; Patrizi, B.; Vannini, M.; Biasini, V. Transparent laser ceramics by stereolithography. Scr. Mater. 2020, 187, 194–196, doi:10.1016/j.scriptamat.2020.06.006.

126. Li, H.; Song, L.; Sun, J.; Ma, J.; Shen, Z. Asynchronous densification of zirconia ceramics formed by stereolithographic additive manufacturing. J. Eur. Ceram. Soc. 2021, 41, 4666–4670, doi:10.1016/j.jeurceramsoc.2021.02.052.

127. Zhu, L.L.; Park, Y.J.; Gan, L.; Go, S. Il; Kim, H.N.; Kim, J.M.; Ko, J.W. Fabrication of transparent MgAl2O4 from commercial nanopowders by hot-pressing without sintering additive. Mater. Lett. 2018, 219, 8–11, doi:10.1016/j.matlet.2018.02.010.

128. Gan, L.; Park, Y.J.; Zhu, L.L.; Kim, H.N.; Ko, J.W.; Kim, H.D. Optical and thermo-mechanical properties of fine-grained transparent yttria ceramics fabricated by hot-press sintering for infrared window applications. J. Eur. Ceram. Soc. 2018, 38, 4064–4069, doi:10.1016/j.jeurceramsoc.2018.04.056.

129. Zhang, R.; Wang, H.; Tian, M.; Liu, M.; Wang, H. Pressureless reaction sintering and hot isostatic strength of transparent MgAlON ceramic with high strength Rongshi. Ceram. Int. 2018, doi:10.1016/j.ceramint.2018.06.203.

130. Zhang, H.; Wang, H.; Gu, H.; Zong, X.; Tu, B.; Xu, P.; Wang, B.; Wang, W.; Liu, S.; Fu, Z. Preparation of transparent $MgO.1.8Al_2O_3$ spinel ceramics by aqueous gelcasting, presintering and hot isostatic pressing. J. Eur. Ceram. Soc. 2018, 38, 4057–4063, doi:10.1016/j.jeurceramsoc.2018.04.057.

131. Carloni, D.; Zhang, G.; Wu, Y. Transparent alumina ceramics fabricated by 3D printing and vacuum sintering. J. Eur. Ceram. Soc. 2021, 41, 781–791, doi:10.1016/j.jeurceramsoc.2020.07.051.

132. Safronova, N.A.; Kryzhanovska, O.S.; Dobrotvorska, M. V.; Balabanov, A.E.; Tolmachev, V. V.; Yavetskiy, R.P.; Parkhomenko, S. V.; Brodskii, R.Y.; Baumer, V.N.; Kosyanov, D.Y.; et al. Influence of sintering temperature on structural and optical properties of Y_2O_3–MgO composite SPS ceramics. Ceram. Int. 2020, 46, 6537–6543, doi:10.1016/j.ceramint.2019.11.137.

133. Shahbazi, H.; Shokrollahi, H.; Tataei, M. Gel-Casting of transparent magnesium aluminate spinel ceramics fabricated by spark plasma sintering (SPS). Ceram. Int. 2017, doi:10.1016/j.ceramint.2017.12.088.

134. Kerbart, G.; Harnois, C.; Bilot, C.; Marinel, S. Pressure-assisted microwave sintering: A rapid process to sinter submicron sized grained $MgAl_2O_4$ transparent ceramics. J. Eur. Ceram. Soc. 2019, 39, 2946–2951, doi:10.1016/j.jeurceramsoc.2019.03.046.

135. Han, Y.; Feng, J.; Zhou, J.; Li, F.; Huang, X.; Wang, L.; Liu, G.; Cheng, J. Heating parameter optimization and optical properties of Nd:YAG transparent ceramics prepared by microwave sintering. Ceram. Int. 2020, 46, 20847–20855, doi:10.1016/j.ceramint.2020.05.117.

136. Godec, Y. Le; Courac, A.; Solozhenko, V.; Godec, Y. Le; Courac, A.; Solozhenko, V.; Godec, Y. Le; Courac, A.; Solozhenko, V.L. High-pressure synthesis of superhard and ultrahard materials To cite this version : HAL Id : hal-02331183 High-pressure synthesis of superhard and ultrahard materials. J. Appl. Phys. 2019, 126, 151102.

137. Salke, N.P.; Xia, K.; Fu, S.; Zhang, Y.; Greenberg, E.; Prakapenka, V.B.; Liu, J.; Sun, J.; Lin, J. Tungsten Hexanitride with Single-Bonded Armchairlike Hexazine Structure at High Pressure HPSTAR. Phys. Rev. Lett. 2021, 126, 65702, doi:10.1103/PhysRevLett.126.065702.

138. Krell, A.; Klimke, J.; Hutzler, T. Transparent compact ceramics: Inherent physical issues. Opt. Mater. (Amst). 2009, 31, 1144–1150, doi:10.1016/j.optmat.2008.12.009.

139. Sikalidis, C. Advances in ceramics- Characterization, raw materials, processing, properties, degradation and healing; Intech, 2001; ISBN 9789533075044.

140. Pappas, J.M.; Dong, X. Direct 3D printing of silica doped transparent magnesium aluminate spinel ceramics. Materials (Basel). 2020, 13, 1–22, doi:10.3390/ma13214810.

141. Gledhill, A.D.; Li, D.; Mroz, T.; Goldman, L.M.; Padture, N.P. Strengthening of transparent spinel/Si_3N_4 nanocomposites. Acta Mater. 2012, 60, 1570–1575, doi:10.1016/j.actamat.2011.11.053.

142. Van de Hulst, H.C. Light Scattering by Small Particles; John Wiley and Sons: New York, 1957;

143. Basu, B.; Kalin, M.; Kumar, B. Friction and wear of ceramics: Principles and Case Studies; 2020; ISBN 9781119538387.

144. Basu, B.; Kalin, M. Tribology of Ceramics and Composites; 2011; ISBN 9780470522639.

145. Lines, M.E.; Glass, A.M. Principles and Applications of Tribology; 1977; Vol. 10; ISBN 3527305521.

146. Ganesh, I. A review on magnesium aluminate ($MgAl_2O_4$) spinel : synthesis , processing and applications. Int. Mater. Rev. 2013, 58, 63–112, doi:10.1179/1743280412Y.0000000001.

147. Wollmershauser, J.A.; Feigelson, B.N.; Gorzkowski, E.P.; Ellis, C.T.; Goswami, R.; Qadri, S.B.; Tischler, J.G.; Kub, F.J.; Everett, R.K. An extended hardness limit in bulk nanoceramics. Acta Mater. 2014, 69, 9–16, doi:10.1016/j.actamat.2014.01.030.

148. Reimanis, I.; Kleebe, H.J. A review on the sintering and microstructure development of transparent spinel ($MgAl_2O_4$). J. Am. Ceram. Soc. 2009, 92, 1472–1480, doi:10.1111/j.1551-2916.2009.03108.x.

149. Kim, B.N.; Morita, K.; Lim, J.H.; Hiraga, K.; Yoshida, H. Effects of preheating of powder before spark plasma sintering of transparent MgAl2O4 spinel. J. Am. Ceram. Soc. 2010, 93, 2158–2160, doi:10.1111/j.1551-2916.2010.03699.x.

150. Zou, Y.; He, D.; Wei, X.; Yu, R.; Lu, T.; Chang, X.; Wang, S.; Lei, L. Nanosintering mechanism of $MgAl_2O_4$ transparent ceramics under high pressure. Mater. Chem. Phys. 2010, 123, 529–533, doi:10.1016/J.MATCHEMPHYS.2010.05.009.

151. Sokol, M.; Kalabukhov, S.; Dariel, M.P.; Frage, N. High-pressure spark plasma sintering (SPS) of transparent polycrystalline magnesium aluminate spinel (PMAS). J. Eur. Ceram. Soc. 2014, 34, 4305–4310, doi:10.1016/J.JEURCERAMSOC.2014.07.022.

152. Morita, K.; Kim, B.N.; Hiraga, K.; Yoshida, H. Fabrication of transparent $MgAl_2O_4$ spinel polycrystal by spark plasma sintering processing. Scr. Mater. 2008, 58, 1114–1117, doi:10.1016/J.SCRIPTAMAT.2008.02.008.

153. Villalobos, G.R.; Sanghera, J.S.; Aggarwal, I.D. Degradation of magnesium aluminum spinel by lithium fluoride sintering aid. J. Am. Ceram. Soc. 2005, 88, 1321–1322, doi:10.1111/j.1551-2916.2005.00209.x.

154. Tsukuma, K.; Mgal, O. Transparent $MgAl_2O_4$ spinel ceramics produced by HIP post sintering. J. Ceram. Soc. Japan 2006, 806, 802–806.

155. Jan Hostasa, Francesco Picelli, Sona Hríbalova, V.N. Sintering aids , their role and behaviour in the production of transparent ceramics. Open Ceram. 2021, 7, doi:10.1016/j.oceram.2021.100137.

156. Bratton, R.J. Translucent Sintered $MgAl_2O_4$. J. Am. Ceram. Soc. 1974, 57, 283–286.

157. Maca, K.; Trunec, M.; Chmelik, R. Processing and properties of fine-grained transparent $MgAl_2O_4$ ceramics. Ceram. - Silikaty 2007, 51, 94–97.

158. Nečina, V.; Pabst, W. Comparison of the effect of different alkali halides on the preparation of transparent $MgAl_2O_4$ spinel ceramics via spark plasma sintering (SPS). J. Eur. Ceram. Soc. 2020, 40, 6043–6052, doi:10.1016/j.jeurceramsoc.2020.06.056.

159. Nečina, V.; Pabst, W. Grain growth of $MgAl_2O_4$ ceramics with LiF and NaF addition. Open Ceram. 2021, 5, 1–6, doi:10.1016/j.oceram.2021.100078.

160. Harris, D.C. Materials for Infrared Windows and Domes; 1999; ISBN 0819434825.

161. Steinbrech, R.W. R-Curve Behavior of Ceramics. Fract. Mech. Ceram. 1992, 9, 187–208, doi:10.1007/978-1-4615-3350-4_14.

162. Shi, Z.; Zhao, Q.; Guo, B.; Ji, T.; Wang, H. A review on processing polycrystalline magnesium aluminate spinel ($MgAl_2O_4$): Sintering techniques, material properties and machinability. Mater. Des. 2020, 193, 108858, doi:10.1016/j.matdes.2020.108858.

163. PAULING, L.; HENDRIC, S.B. Crystal structure of Hematite and Corondum. 1925, 346.

164. Krell, A.; Baur, G.; Dahne, C. Transparent sintered sub-micro meter Al2O3 with IR transmissivity equal to sapphire. Wind. Dome Technol. 2003, 5078, 199–207.

165. Trunec, M.; Maca, K.; Chmelik, R. Polycrystalline alumina ceramics doped with nanoparticles for increased transparency. J. Eur. Ceram. Soc. 2015, 35, 1001–1009, doi:10.1016/j.jeurceramsoc.2014.09.041.

166. Stuer, M.; Zhao, Z.; Aschauer, U.; Bowen, P. Transparent polycrystalline alumina using spark plasma sintering : Effect of Mg, Y and La doping. J. Eur. Ceram. Soc. 2010, 30, 1335–1343, doi:10.1016/j.jeurceramsoc.2009.12.001.

167. Ferna, A.; Mene, J.L.; Torrecillas, R.; Sua, M. Grain growth control and transparency in spark plasma sintered self-doped alumina materials. Scr. Mater. 2009, 61, 931–934, doi:10.1016/j.scriptamat.2009.07.026.

168. Mccauley, J.W.; Patel, P.; Chen, M.; Gilde, G.; Strassburger, E.; Paliwal, B.; Ramesh, K.T.; Dandekar, D.P. AlON : A brief history of its emergence and evolution. J. Eur. Ceram. Soc. 2009, 29, 223–236, doi:10.1016/j.jeurceramsoc.2008.03.046.

169. Ish-Shalom, M. Formation of aluminium oxynitride by carbothermal reduction of aluminium oxide in nitrogen. J. Mater. Sci. Lett. 1982, 1, 147–149.

170. Hartnett, T.M.; Bernstein, S.D.; Maguire, E.A.; Tustison, R.W. Optical properties of ALON (aluminum oxynitride). Wind. Dome Technol. Mater. 1997, 3060, 284–295, doi:10.1117/12.277053.

171. Su, M.; Zhou, Y.; Wang, K.; Yang, Z.; Cao, Y.; Hong, M. Highly transparent AlON sintered from powder synthesized by direct nitridation. J. Eur. Ceram. Soc. 2015, 35, 1173–1178, doi:10.1016/j.jeurceramsoc.2014.10.036.

172. Suh, M.S.; Chae, Y.H.; Kim, S.S. Friction and wear behavior of structural ceramics sliding against zirconia. Wear 2008, 264, 800–806, doi:10.1016/j.wear.2006.12.079.

173. Bull, S.J.; Kingswell, R.; Scott, K.T. The sliding wear of plasma sprayed alumina. Surf. Coatings Technol. 1996, 82, 218–225, doi:10.1016/0257-8972(95)02641-X.

174. Zhao, X.J.; Guo, L.; Cai, Z.Y.; Xiao, L.R.; Zhao, Z.W.; Li, G.; Han, J.; Ru, H.Q.; Zhang, N.; Chen, D.L. SiC and ZrN nano-particulate reinforced AlON composites: Preparation, mechanical properties and toughening mechanisms. Ceram. Int. 2016, 42, 6072–6079, doi:10.1016/j.ceramint.2015.12.164.

175. Liu, X.; Wang, H.; Tu, B.; Wang, W.; Fu, Z. Highly transparent $Mg_{0.27}Al_{2.58}O_{3.73}N_{0.27}$ ceramic prepared by pressureless sintering. J. Am. Ceram. Soc. 2014, 97, 63–66, doi:10.1111/jace.12711.

176. Ma, B.; Wang, Y.; Zhang, W.; Chen, Q. Pressureless sintering and fabrication of highly transparent MgAlON ceramic from the carbothermal powder. J. Alloys Compd. 2018, 745, 617–623, doi:10.1016/j.jallcom.2018.02.254.

177. Zhang, R.; Wang, Y.; Tian, M.; Wang, H. Highly transparent LiAlON ceramic prepared by reaction sintering and post hot isostatic pressing. J. Eur. Ceram. Soc. 2018, 38, 5252–5256, doi:10.1016/j.jeurceramsoc.2018.07.053.

178. Clay, D.; Poslusny, D.; Flinders, M.; Jacobs, S.D.; Cutler, R.A. Effect of LiAl5O8 additions on the sintering and optical transparency of LiAlON. J. Eur. Ceram. Soc. 2006, 26, 1351–1362, doi:10.1016/j.jeurceramsoc.2005.01.056.

179. Maguire, E.A.; Hartnett, T.M.; Gentilman, R.L. Method of producing aluminum oxynitride having improved optical characteristics. 1987.

180. Hartnett, T.M.; Gentilman, R.L.; Maguire, E.A. Aluminum Oxynitride Having Improved Optical Characteristics and Method of Manufacture. 1984.

181. Gentilman, R.L.; Maguire, E.A.; Dolhert, L.E. Transparent Aluminum Oxynitride and Method of Manufacture. 1984.

182. Yang, P.; Gai, S.; Liu, Y.; Wang, W.; Li, C.; Lin, J. Uniform Hollow Lu_2O_3:Ln (Ln: Eu^{3+} ,Tb^{3+}) Spheres : Facile Synthesis and Luminescent Properties. Am. Chem. Soc. 2011, 2182–2190.

183. Loiko, P.A.; Yumashev, K. V.; Schödel, R.; Peltz, M.; Liebald, C.; Mateos, X.; Deppe, B.; Kränkel, C. Thermo-optic properties of Yb:Lu2O3 single crystals. Appl. Phys. B Lasers Opt. 2015, 120, 601–607, doi:10.1007/s00340-015-6171-4.

184. Li, C.; Zhang, F.; Wang, X.; Rao, X. Repeated nanoscratch and double nanoscratch tests of Lu_2O_3 transparent ceramics: Material removal and deformation mechanism, and theoretical model of penetration depth. J. Eur. Ceram. Soc. 2018, 38, 705–718, doi:10.1016/j.jeurceramsoc.2017.09.028.

185. Lawn, B. Fracture of brittle solids. Cambridge Solid State Sci. Ser. 2010.

186. An, L.; Ito, A.; Goto, T. Fabrication of transparent lutetium oxide by spark plasma sintering. J. Am. Ceram. Soc. 2011, 94, 695–698, doi:10.1111/j.1551-2916.2010.04145.x.

187. Kijko, V.S.; Maksimov, R.N.; Shitov, V.A.; Demakov, S.L.; Yurovskikh, A.S. Sintering of transparent Yb-doped Lu2O3 ceramics using nanopowder produced by laser ablation method. J. Alloys Compd. 2015, 643, 207–211, doi:10.1016/j.jallcom.2015.04.127.

188. Pirri, A.; Toci, G.; Patrizi, B.; Vannini, M. An Overview on Yb-Doped Transparent Polycrystalline Sesquioxide Laser Ceramics. IEEE J. Sel. Top. Quantum Electron. 2018, 24, 1–8, doi:10.1109/JSTQE.2018.2799003.

189. Search, H.; Journals, C.; Contact, A.; Iopscience, M.; Address, I.P. Measurement of the Optical Constants of Yttrium Oxide. Japenese J. Appl. Phys. 1968, 7, 404–408.

190. Id, O.; Id, O.; Furuse, H.; Nakasawa, S.; Yoshida, H.; Morita, K.; Suzuki, T.S.; Kim, B.; Sakka, Y.; Hiraga, K.; et al. Transparent ultrafine Yb^{3+}:Y_2O_3 laser ceramics fabricated by spark plasma sintering. Am. Ceram. Soc. 2018, 0–2, doi:10.1111/ijlh.12426.

191. Marder, R.; Chaim, R.; Estournès, C. Grain growth stagnation in fully dense nanocrystalline Y2O3 by spark plasma sintering. 2010, 527, 1577–1585, doi:10.1016/j.msea.2009.11.009.

192. Maksimov, R.N.; Esposito, L.; Hostaša, J.; Shitov, V.A.; Belov, P.A. Densification and phase transition of Yb-doped Lu2O3 nanoparticles synthesized by laser ablation. Mater. Lett. 2016, 185, 396–398, doi:10.1016/j.matlet.2016.09.038.

193. Ikegami, T.; Li, J.G.; Mori, T.; Moriyoshi, Y. Fabrication of transparent yttria ceramics by the low-temperature synthesis of yttrium hydroxide. J. Am. Ceram. Soc. 2002, 85, 1725–1729, doi:10.1111/j.1151-2916.2002.tb00342.x.

194. Jin, L.; Zhou, G.; Shimai, S.; Zhang, J.; Wang, S. ZrO_2-doped Y_2O_3 transparent ceramics via slip casting and vacuum sintering. J. Eur. Ceram. Soc. 2010, 30, 2139–2143, doi:10.1016/j.jeurceramsoc.2010.04.004.

195. Zhang, J.; An, L.; Liu, M.; Shimai, S.; Wang, S. Sintering of Yb_{3+}:Y_2O_3 transparent ceramics in hydrogen atmosphere. J. Eur. Ceram. Soc. 2009, 29, 305–309, doi:10.1016/j.jeurceramsoc.2008.03.006.

196. RHODES, W.H. Controlled Transient Solid Second- Phase Sintering of Yttria. J. Am. Ceram. Soc. 1981, 64, 13–19, doi:10.1111/j.1151-2916.1981.tb09551.x.

197. Eilers, H. Fabrication, optical transmittance, and hardness of IR-transparent ceramics made from nanophase yttria. J. Eur. Ceram. Soc. 2007, 27, 4711–4717, doi:10.1016/j.jeurceramsoc.2007.04.006.

198. Blair, V.L.; Fleischman, Z.D.; Merkle, L.D.; Nicholas, Ku; Moorehead, C.A. Co-precipitation of rare-earth-doped Y_2O_3 MgO nanocomposites for mid-infrared solid-state lasers. Appl. Opt. 2017, 56, 154–58, doi:10.7868/s0002337x14090048.

199. Safronova, N.A.; Yavetskiy, R.P.; Kryzhanovska, O.S.; Dobrotvorska, M. V.; Balabanov, A.E.; Vorona, I.O.; Tolmachev, V.; Baumer, V.N.; Matolínová, I.; Kosyanov, D.Y.; et al. A novel IR-transparent Ho^{3+}:Y_2O_3–MgO nanocomposite ceramics for potential laser applications. Ceram. Int. 2021, 47, 1399–1406, doi:10.1016/j.ceramint.2020.08.263.

200. Ahmadi, B.; Razavi, S.; Ahsanzadeh-vadeqani, M.; Barekat, M. Mechanical and optical properties of spark plasma sintered transparent Y_2O_3 ceramics. Ceram. Int. 2016, 42, 17081–17088, doi:10.1016/j.ceramint.2016.07.218.

201. Serivalsatit, K.; Kokuoz, B.; Yazgan-Kokuoz, B.; Kennedy, M.; Ballato, J. Synthesis, processing, and properties of submicrometer-grained highly transparent yttria ceramics. J. Am. Ceram. Soc. 2010, 93, 1320–1325, doi:10.1111/j.1551-2916.2010.03601.x.

202. Solozhenko, V.L.; Kurakevych, O.O.; Godec, Y. Le Creation of Nanostuctures by Extreme Conditions : High- Pressure Synthesis of Ultrahard Nanocrystalline Cubic Boron Nitride. Adv. Mater. 2012, 24, 1540–1544, doi:10.1002/adma.201104361.

203. Dubrovinskaia, N.; Dubrovinsky, L. Controversy about ultrahard nanotwinned cBN. Nature 2013, 502, E1–E2, doi:10.1038/nature12620.

204. Harris, T.K.; Brookes, E.J.; Taylor, C.J. The effect of temperature on the hardness of polycrystalline cubic boron nitride cutting tool materials. Int. J. Refract. Metals Hard Mater. 2004, 22, 105–110, doi:10.1016/j.ijrmhm.2004.01.004.

205. Taniguchi, T.; Akaishi, M.; Yamaoka, S. Sintering of cubic boron nitride without additives at 7.7 GPa and above 2000 C. J. Mater. Res. 2000, 14, 162–169.

206. Hooper, R.M.; Shakib, J.I.; Brookes, C.A. Microstructure and wear of TiC-cubic BN tools. Mater. Sci. Eng. 1988, 105–106, 429–433, doi:10.1016/0025-5416(88)90727-6.

207. Hostas, J.; Silvestroni, L.; Piancastelli, A.; Sciti, D.; Esposito, L.; Martino, D. Di; Spa, M.I.; Km, V.T. Slip Casting of a Si_3N_4-Based System. Int. J. Appl. Ceram. Technol. 2012, 9, 246–258, doi:10.1111/j.1744-7402.2011.02718.x.

208. Ding, S.; Zeng, Y.; Jiang, D. Oxidation bonding of porous silicon nitride ceramics with high strength and low dielectric constant. Mater. Lett. 2007, 61, 2277–2280, doi:10.1016/j.matlet.2006.08.067.

209. Qi, G.; Zhang, C.; Hu, H. High strength three-dimensional silica fiber reinforced silicon nitride-based composites via polyhydridomethylsilazane pyrolysis. Ceram. Int. 2007, 33, 891–894, doi:10.1016/j.ceramint.2006.01.018.

210. Riley, F.L. Silicon Nitride and Related Materials. J. Am. Ceram. Soc. 2000, 65, 245–265.

211. A.Ziegler; C.Idrobo, J.; Cinibulk, M.K.; C.Kisielowski; Browning, N.D.; Ritchie, R.O. Interface Structure and Atomic Bonding Characteristics in Silicon Nitride Ceramics. Science. 2014, 306, 1768–70, doi:10.1126/science.1104173.

212. Pezzotti, G.; Okamoto, T.; Miyamoto, Y. Hot Isostatic Press Sintering and Properties of Silicon Nitride without Additives. J. Am. Ceram. Soc. 1989, 60, 1656–1660.

213. Dante, R.C.; Kajdas, C.K. A review and a fundamental theory of silicon nitride tribochemistry. Wear 2012, 288, 27–38, doi:10.1016/j.wear.2012.03.001.

214. Philipp, H.R. Optical Properties of Silicon Nitride. J. Electrochem. Soc. 1973, 120, 0–5.

215. Mao, X.; Shimai, S.; Dong, M.; Wang, S. Gelcasting and pressureless sintering of translucent alumina ceramics. J. Am. Ceram. Soc. 2008, 91, 1700–1702, doi:10.1111/j.1551-2916.2008.02328.x.

216. Mouzon, J.; Glowacki, E.; Odén, M. Comparison between slip-casting and uniaxial pressing for the fabrication of translucent yttria ceramics. J. Mater. Sci. 2008, 43, 2849–2856, doi:10.1007/s10853-007-2261-y.

217. Yang, Z.; Wang, H.; Min, X.; Wang, W.; Fu, Z.; Lee, S.W.; Niihara, K. Translucent Li-α-sialon ceramics prepared by spark plasma sintering. J. Am. Ceram. Soc. 2010, 93, 3549–3551, doi:10.1111/j.1551-2916.2010.04081.x.

218. Ye, F.; Liu, C.; Liu, L.; Zhou, Y. Optical properties of in situ toughened ScLu-α-SiAlON. Scr. Mater. 2009, 61, 982–984, doi:10.1016/j.scriptamat.2009.08.010.

219. Xue, J.; Liu, Q.; Fang, M.; Ma, L.; Xiu, T.; Gui, L. Effects of process on microstructure and properties of translucent Dy-α-SiAlON sintered at lower temperatures. J. Ceram. Soc. Japan 2008, 116, 822–824, doi:10.2109/jcersj2.116.822.

220. Pechenik, A.; Piermarini, G.J.; Danforth, S.C. Fabrication of Transparent Silicon Nitride from Nanosize Particles. J. Am. Ceram. Soc. 1992, 75, 3283–3288, doi:10.1111/j.1151-2916.1992.tb04422.x.

221. Singh, J.P.; Bansal, N.P.; Kriven, W.M. Advances in Ceramic Matrix Composites X; 2005; ISBN 6147945890.

222. Yang, W.W.; Inada, M.; Tanaka, Y.; Enomoto, N.; Hojo, J. Fabrication of translucent silicon nitride ceramics with various sintering aids. Int. J. Nanotehcnology 2013, 10, 119–125.

223. Zhang, W. A review of tribological properties for boron carbide ceramics. Prog. Mater. Sci. 2020, 100718, doi:10.1016/j.pmatsci.2020.100718.

224. Tokariev, O.; Schnetter, L.; Beck, T.; Malzbender, J. Grain size effect on the mechanical properties of transparent spinel ceramics. J. Eur. Ceram. Soc. 2013, 33, 749–757, doi:10.1016/j.jeurceramsoc.2012.09.024.

225. Marshall, D.B.; Lawn, B.R.; Evans, A.G. Elastic/Plastic Indentation Damage in Ceramics: The Lateral Crack System. J. Am. Ceram. Soc. 1981, 65, 6.

226. Lawn, B.R.; Padture, N.P.; Guiberteau, F.; Cai, H. A model for microcrack initiation and propagation beneath hertzian contacts in polycrystalline ceramics. Acta Metall. Mater. 1994, 42, 1683–1693, doi:10.1016/0956-7151(94)90378-6.

227. Tewari, A.; Basu, B.; Bordia, R.K. Model for fretting wear of brittle ceramics. Acta Mater. 2009, 57, 2080–2087, doi:10.1016/j.actamat.2009.01.013.

228. Hsu, S.M.; Shen, M. Wear prediction of ceramics. Wear 2004, 256, 867–878, doi:10.1016/J.WEAR.2003.11.002.

229. Lee, S.C.; Cheng, H.S. On the relation of load to average gap in the contact between surfaces with longitudinal roughness. Tribol. Trans. 1992, 35, 523–529, doi:10.1080/10402009208982151.

230. Archard, J.F. The temperature of rubbing surfaces. Wear 1959, 2, 438–455, doi:10.1016/0043-1648(59)90159-0.

231. Greskovich, C. Preparation of High-Density Si_3N_4 by a Gas-Pressure Sintering Process. J. Am. Ceram. Soc. 1981, 64, 725–730.

232. Pabst, W.; Hříbalová, S. Light scattering models for describing the transmittance of transparent and translucent alumina and zirconia ceramics. J. Eur. Ceram. Soc. 2021, 41, 2058–2075, doi:10.1016/j.jeurceramsoc.2020.10.025.

233. Munir, Z.A.; Anselmi-Tamburini, U. The effect of electric field and pressure on the synthesis and consolidation of materials : A review of the spark plasma sintering method. J. Mater. Sci. 2006, 1, 763–777, doi:10.1007/s10853-006-6555-2.

234. Quach, D. V; Avila-paredes, H.; Kim, S.; Martin, M.; Munir, Z.A. Pressure effects and grain growth kinetics in the consolidation of nanostructured fully stabilized zirconia by pulsed electric current sintering. Acta Mater. 2010, 58, 5022–5030, doi:10.1016/j.actamat.2010.05.038.

235. Bakshi, S.R.; Musaramthota, V.; Lahiri, D.; Singh, V.; Seal, S.; Agarwal, A. Spark plasma sintered tantalum carbide : Effect of pressure and nano-boron carbide addition on microstructure and mechanical properties. Mater. Sci. Eng. A 2011, 528, 1287–1295, doi:10.1016/j.msea.2010.10.009.

236. Kim, B.; Hiraga, K.; Grasso, S.; Morita, K.; Yoshida, H.; Zhang, H.; Sakka, Y. High-pressure spark plasma sintering of MgO-doped transparent alumina. 2012, 116–118.

237. Grasso, S.; Hu, C.; Maizza, G.; Kim, B.-N.; Sakka, Y. Effects of Pressure Application Method on Transparency of Spark Plasma Sintered Alumina. J. Am. Ceram. Soc. 2011, 1409, 1405–1409, doi:10.1111/j.1551-2916.2010.04274.x.

238. Lu, T.C.; Chang, X.H.; Qi, J.Q.; Luo, X.J.; Wei, Q.M.; Zhu, S.; Sun, K.; Lian, J.; Wang, L.M.; Lu, T.C.; et al. Low-temperature high-pressure preparation of transparent nanocrystalline $MgAl_2O_4$ ceramics Low-temperature high-pressure preparation of transparent nanocrystalline $MgAl_2O_4$ ceramics. Appl. Phys. Lett. 2006, 88, 1–3, doi:10.1063/1.2207571.

239. Perepezko, J.H.; Massalski, T.B. A note on the nature of massive transformation interfaces. Scr. Metall. 1972, 6, 743–752.

240. Meng, Y.; Xu, J.; Jin, Z.; Prakash, B.; Hu, Y. A review of recent advances in tribology; 2020; Vol. 8; ISBN 4054402003.

241. Rigney, D.A. Colmments of metals on the sliding wear. Tribol. Int. 1997, 30, 361–367.

242. Hokkirigawa, K.; Kato, K. An experimental and theoretical investigation of ploughing, cutting and wedge formation during abrasive wear. Tribol. Int. 1988, 21, 51–57.

243. Kato, K. Abrasive wear of metals. Tribol. Int. 1997, 30, 333–338, doi:10.1016/S0301-679X(96)00063-1.

244. Yang, X.; Qiu, Z.; Wang, Y. Stress interaction and crack propagation behavior of glass ceramics under multi-scratches. J. Non. Cryst. Solids 2019, 523, 119600, doi:10.1016/j.jnoncrysol.2019.119600.

245. Li, C.; Zhang, F.; Meng, B.; Rao, X.; Zhou, Y. Research of material removal and deformation mechanism for single crystal GGG ($Gd_3Ga_5O_{12}$) based on varied-depth nanoscratch testing. Mater. Des. 2017, 125, 180–188, doi:10.1016/J.MATDES.2017.04.018.

246. Van Swygenhoven, H.; Derlet, P.M. Grain-boundary sliding in nanocrystalline fcc metals. Phys. Rev. B - Condens. Matter Mater. Phys. 2001, 64, 1–9, doi:10.1103/PhysRevB.64.224105.

247. Schiøtz, J.; Di Tolla, F.D.; Jacobsen, K.W. Softening of nanocrystalline metals at very small grain sizes. Nature 1998, 391, 561–563, doi:10.1038/35328.

248. Schiøtz, J.; Vegge, T.; Di Tolla, F.D.; Jacobsen, K.W. Atomic-scale simulations of the mechanical deformation of nanocrystalline metals. Phys. Rev. B - Condens. Matter Mater. Phys. 1999, 60, 11971–11983, doi:10.1103/PhysRevB.60.11971.

249. Shan, Z.; Stach, E.A.; Wiezorek, J.M.K.; Knapp, J.A.; Follstaedt, D.M.; Mao, S.X. Grain boundary-mediated plasticity in nanocrystalline nickel. Science. 2004, 305, 654–657, doi:10.1126/science.1098741.

250. Ke, M.; Hackney, S.A.; Milligan, W.W.; Aifantis, E.C. Observation and measurement of grain rotation and plastic strain in nanostructured metal thin films. Nanostructured Mater. 1995, 5, 689–697, doi:10.1016/0965-9773(95)00281-I.

251. Wang, L.; Teng, J.; Liu, P.; Hirata, A.; Ma, E.; Zhang, Z.; Chen, M.; Han, X. Grain rotation mediated by grain boundary dislocations in nanocrystalline platinum. Nat. Commun. 2014, 5, 1–7, doi:10.1038/ncomms5402.

252. Farkas, D.; Frøseth, A.; Van Swygenhoven, H. Grain boundary migration during room temperature deformation of nanocrystalline Ni. Scr. Mater. 2006, 55, 695–698, doi:10.1016/j.scriptamat.2006.06.032.

253. Kim, S.S.; Kato, K.; Hokkirigawa, K.; Abé, H. Wear mechanism of ceramic materials in dry rolling friction. J. Tribol. 1986, 108, 522–526, doi:10.1115/1.3261255.

254. Wang, Y.S.; Hsu, S.M.; Munro, R.G. Ceramics wear maps: alumina. Lubr. Eng. 1991, 47, 63–69.

255. Trabelsi, R.; Treheux, D.; Orange, G.; Fantozzi, G.; Homerin, P.; Thevenot, F. Relationship between mechanical properties and wear resistance of alumina-zirconia ceramic composites. Tribol. Trans. 1989, 32, 77–84, doi:10.1080/10402008908981865.

List of Figure Captions

Fig. 1: Hardness and fracture toughness of different transparent ceramics such as SiAlON, Si3N4, AlON, Y2O3, Al2O3, MgAl2O4, NBK-7, Float glass, Float glass hardened, Borofloat, Borofloat hardened, Gorilla glass, Gorilla glass hardened, B270, B270 Hardened [37,44,63,65,75,86,92,94,96–101,111–113].

Fig. 2: Different sources for scattering the light.

Fig. 3: Typical scratch patterns on brittle materials during a progressive scratch [66].

Fig. 4: Microstructure of MgAl2O4 obtained a), b), c) via SPS at different temperature without additive [35], d) via HIP without additive [60] e), f) via HIP at different temperature with 0.5 wt% LiF and 1 wt% LiF [60], g) and h) via HIP at different temperature with 1 wt% Si3N4 and 3 wt% Si3N4 [48].

Fig. 5: Wear rate of Spinel and AlON [28].

Fig. 6: Hardness, fracture toughness and mass loss upon friction vs. sintering temperature of spinel [35].

Fig. 7: Microstructure of Al2O3 obtained via SPS at 1350 oC a) pure and doped with b) Mg, c) Y and , d) La [166], or e) doped by ZrO2 and MgAl2O4, [165] and f) by ZrO2 and MgO, presintered and HIPed [39]

Fig. 8: Microstructure of a) pure AlON [174] b) SiC-ZrN-AlON composite [174] c), d), e) MgAlON [175,176], f), and g) LiAlON [177,178]

Fig. 9: Relationship of a) penetration depth vs. normal force and b) coefficient of friction vs. normal force in single nanoscratch and repeated nanoscratch tests on Lu2O3 TCs [184].

Fig. 10: Crack propagation in transparent Lu2O3 under a) low load and b) high load conditions [184].

Fig. 11: Microstructure of a), b), c) undoped Lu2O3 sintered by single stage SPS, d) Yb-doped two stage SPS, and e) Yb-doped two stage vacuum sintering [186,187].

Fig. 12: Variation of average grain size (µm), transparency (%), and relative density (%) of transparent Lu2O3 without additive as a function of the sintering temperature by SPS [186,187].

Fig. 13: Micrographs of transparent Y2O3 obtained a) via vacuum sintering without additive [194] b), c), d) via vacuum sintering with 0.2 mol%, 2 mol% and 5 mol% ZrO2 dopant [194] e) via HIP followed by vacuum sintering [197], f), g), h) and i) via SPS at different temperatures [200].

Fig. 14: Relative density, hardness, and fracture toughness vs. sintering temperature of cBN with initial particle size a) 0.5-1.2 µm b) 2-4 µm, and c) 8-12 µm [205]

Fig. 15: Doping agent vs. Hardness and Fracture Toughness in Si3N4.

Fig. 16: Variation of a) hardness, fracture toughness, wear volume, and b) friction coefficient with different h-BN content [100].

Fig. 17: Modeling wear in different wear regimes. (a) Asperity-scale abrasion in mild wear regime, (b) tensile cracks inside the nominal contact in severe wear regime, and (c) gross fracture in the nominal contact in ultra-severe wear regime [228].

Fig. 18: VIckers Hardness (1kg) of cubic silicon nitride compared to other super-hard ceramics [83].

Fig. 19: SEM micrographs of fracture damage in wear scars in a) coarse spinel, b) nano spinel and c) fine spinel at the end of the sliding wear test (1000 min) [54].

Fig. 20: Transparency vs. a) Hardness, and b) Fracture Toughness for different TCs [27,37,59,63,65,75,83,86,92–101,111,112]

Fig. 21: Types of mechanisms observed during abrasive wear depending on abrasive particles.

Fig. 22: Representation of a) interlocking of abrasive and doped particle, and b) their wear during sliding of abrasive particle on transparent ceramic.

Fig. 23: Transmission electron micrographs of transparent Lu2O3 during sliding wear [184].

Fig. 24: High-resolution transmission electron microscopy of sections a) I, and b) II shown in figure 22b. c) and d) represent the types of flaws formed beneath scratch [184].

Fig. 25: Morphologies of the worn surfaces of transparent MgAl2O4/Si3N4 nanocomposite sintered at a) 1300°C b) 1350°C c) 1400°C [35] passing from groves, to accumulated material and cracking of the worn surface due to an increased grain size of the matrix.

List of Table Captions

Table 1: Effect of different factors on transparency and tribological behavior

Table 2: Physical properties of transparent ceramics with potential in tribological applications. [27,37,59,63,65,75,83,86,92–112]

Table 3: Mechanical and optical properties of different AlON-based ceramics.

Table 4: Mechanical and optical properties of different Y_2O_3 TCs.

Table 5: Mechanical, optical, and tribological behaviour of TCs.

Table 6: Potential tribological behaviour with respect to improved mechanical properties of TCs.